Author response to reviewers (our words in red)

Preamble:

Firstly, I would like to sincerely apologise for the delay in returning the revised manuscript. We have had a horror summer in Canberra (eastern Australia), involving drought, bushfire, hailstorms, and flood. This has severely disrupted all our lives (https://www.abc.net.au/news/2020-03-01/canberras-summer-of-fire-heat-rain-and-hail/12011124). I thank you for your patience.

As suggested, I have attached the marked-up version of the revised manuscript to this document. The reviews, while concise, suggested a rather extensive revision. Consequently, there is a lot going on in the marked-up document. For this I apologise also.

General:

We agree with the reviewers that our contribution has attempted to cover a lot of ground, some not exclusively related to the new data presented on the Lake Muir earthquake sequence. With this in mind we have trimmed the manuscript discussion. However, we retain insight that the Lake Muir sequence has contributed to regarding stable continental region earthquakes. Further, we expand the introduction to appeal more to the international readership of Solid Earth, and better scope our stable continental region focus. One area of concern for both reviewers was the degree to which deductions on earthquake genesis and relationships to faulting may be made from our main shock locations and aftershock relocations. We recognise that the uncertainties relating to earthquake locations were not well-communicated, and have rectified this deficiency. Specifically, we note that the uncertainties on aftershock locations are better than 300 m in all cases. The reviewed manuscript presented the initial Australian National Seismic Network locations for the three largest events in the sequence as these events failed key tests for double-difference relocation. This resulted in the undesirable situation where the main shocks were associated with horizontal location uncertainties of 5-6 km. In the revised manuscript we have relocated the two largest events based upon the relatively well located third largest event in the sequence. This relocation has resulted in collapse of the horizontal location uncertainty ellipses to ~ 1 km, and allows for better comparison between main shocks, aftershocks, and surface and geological data. The revised Figures 3 and 6 are attached as an example of the improvement.

Reply to specific comments made by EC1:

- "I suggest focusing on the characterization of the seismic sequence, its surface deformation and propose some explanation for the longer ruptures in comparison to the commonly used scaling relationships". The focus of the manuscript has been reframed in the introduction, and the relationship developed between visible surface rupture length (VSRL) and detectible surface rupture length (DSRL) removed as suggested. Discussion of the length of ruptures has been reserved for a future publication. Instead we consider in more detail the treiggering implications between events, as suggested by reviewer RC1.
- "Comprehensive figure where the data are integrated". It is not clear what the reviewer desires here. Figure 6 presents the InSAR results as a base, with the relocated epicentres, and rupture traces from field mapping and InSAR (black and white lines respectively) overlain. The only data not presented on this figure are the UAV data, which are presented in Figure 7. We feel that combining the UAV data with Figure 6 would unnecessarily clutter the figure. Or does the reviewer refer to his comment on Section 4.1.3, which is addressed below?
- "Title: Change in the title the part dealing with rethinking Australian stable continental region Earthquakes": Title text after the colon modified to more concisely introduce the paper content: "new insight into Australian stable continental region earthquakes"

- "For an international journal it would be more appropriate an introduction presenting data on moderate magnitude seismic sequences, their associated surface deformation and surface breaks (length)". We have rewritten the Introduction to better set the scope of the manuscript. We retain our focus on the stable continental region (SCR) setting, but have presented our study in the framework of global SCR earthquakes that precede the Lake Muir sequence, many of which have been imaged by InSAR. Table 1 has been expanded considerably to present data relating to these earthquakes.
- "Is it possible to better explain the meaning of grain in the landscape or add a reference for it?". We mean grain in the same way that trees have grain; a preferential alignment of constituent elements. To clarify, the word 'grain' in the sentence has been replaced with "an alignment of valleys and ridges".
- "At lines 285-295 the Authors infer fault geometry by aftershock distribution… To me this dataset is not enough to depict fault geometry". As a preamble to addressing this reviewer concern we note that in response to reviewer RC1 misunderstanding our aftershock deployment geometry we have added text to section 2.3 and to the caption of Figure 2 noting that the rapid deployment kits are prefixed by LM on Figure 2. We have also stated the uncertainties associated with the aftershock relocations in the text of Section 3.4, which was not made clear before. The mean location uncertainties in the relocated dataset were calculated to be 63 m, 116 m, and 228 m in the east, north and up directions, respectively. It is true that the computed aftershock distribution does not define a neat rupture plane, nor are relocated earthquakes so numerous, as may be the case in the plate margin examples presented by the reviewer. However, given the tight uncertainties we contend that the scatter is real, and the main concentration of aftershocks 'in general' occupy a volume defined by positive coulomb stress changes. This is especially the case when the Coulomb stress changes are resolved for optimal strike slip receiver faults. A new part to Figure 8 has been crafted to show this relationship. As the reviewer notes, this relationship remains less than 100%. However, we contend this stems in part from the 'real' scatter, and perhaps also to fluid migration of the sort described by Townend & Zoback (2000). We have tightened the text of Section 3.4, and the caption of Figure 8, to improve the clarity of communication of our observations.
- Section 3.5. "Relationship between moment magnitude and surface rupture length amongst Australian cratonic earthquakes. I suggest removing this paragraph". As this section was of concern to both reviewers, we have removed it. Instead, we focus on the utility of the InSAR data for deducing source parameters of each of the mainshock ruptures.
- Section 4.1.3. Co-location of thrust and strike-slip events: This is a quite big speculation since the resolution of the data do not allow for this, or data are not well presented to convince the reader about this. Provide an integrated picture to support the co-location. We must conclude that there are deficiencies in our presentation of the data as the evidence from the INSAR images is compelling and incontrovertible for an overlap of surface deformation envelopes resulting from the two largest events. This is explicitly stated in the text and is shown in Figure 6, where the surface trace of the strike-slip fault rupture relating to the November event (panels c and d) has been superposed onto the surface deformation pattern of the September event (panels a and b). We agree that there is significant uncertainty in relating the main shocks and aftershock distribution to geological structures. As mentioned in our general comments, we have tightened the uncertainties associated with the locations for the three largest events, and better communicated the uncertainties associated with the aftershock relocations. We contend that this allows us a firmer basis to explore the relationship between the rupture planes fro the larger events, and the aftershock locations.
- Section 4.1.3. "The sentence starting at line 443… In general, the volume in which aftershocks are located corresponds to a volume of positive Coulomb stress change resulting from the main shock (Figure 8)", is not 100% consistent with aftershock distribution… I suggest to significantly reduce this part and incorporate it in the discussion on the seismic sequence". As mentioned above, we have tightened the text in terms of communicating the uncertainties

associated with the hypocentral locations. Further, we have provided a potential explanation in the text for the hypocentres that do not occur in the volume of positive Coloumb stress. We contend that this justifies retaining the section.

- Section 4.1.4 “Mechanisms for strain localisation in Stable Continental Region (SCR) crust... This paragraph is not strongly related to the data presented in the manuscript but mainly based on literature. I suggest removing this part.” This section removed as suggested.
- Section 4.2 “One-off ruptures from moderate to large magnitude earthquakes in the cratonic regions of Australia... I suggest removing this part.” The section has been sharpened to emphasise that there is no evidence for prior rupture on the Lake Muir faults, and this is typical of Precambrian non-extended SCR crust worldwide, as presented in the reworded introduction. In addition, a section has been added prior (a new section 4.2) that discusses the stress triggering aspects of the new data, as recommended by reviewer RC1. The new sections 4.2 and 4.3 now focus on relating characteristics evident in the Lake Muir Ruptures with ruptures in analogous crust worldwide.
- Section 4.3. “Migration of the locus of moment release in the Southwest Seismic Zone… I suggest deleting it” This section has been deleted as suggested.
- Section 4.4. Deleted as suggested.

Reply to specific comments made by RC1:

- Section 2.3. “Rapid Deployment aftershock kits… Regarding the seismic station deployment, the closest station has been located at least at 24 km far from the epicentral area of both earthquakes... large uncertainties might afflict the location of small magnitude earthquakes occurred during the swarms”. The reviewer misunderstood our communication of the experimental design. The nearest ***permanent*** network station is 24 km from the epicentral area. This is explicitly stated in the text. The five rapid deployment aftershock kits range in distance from right on top of the first main shock (LM01), to 42 km distant (LM05). We have added text to Section 2.3, and the caption of Figure 2, to make clear that the black triangles with labels prefixed by ‘LM’ on Figure 2 are the temporary stations. We understand that the network, comprising permanent and temporary stations, is not as dense as might be achieved in regions where there is a higher perception of earthquake hazard (i.e. non-SCR), but are satisfied that our uncertainties (better than 300 m for aftershocks) is suitable to make our conclusions. Further, relocation of the three largest events in the revised manuscript places us in a much better position to relate these events to structure and to the aftershocks.
- Section 3.5. “In my opinion this latter argument [new relationships between moment magnitude and surface rupture length] deserves a separate paper. The paper should be more focused to the expected results introduced by the title.” This section has been removed as suggested by both reviewers. The wording has been changed throughout to celebrate the ability of the InSAR data to detect and characterise surface ruptures in remote areas, such as SCR crust.
- Line 445-448. “They don’t clearly explain if they consider the November earthquake induced by a dynamic triggering of the September event …I think the clarification of this point could be an important statement for future and more addressed studies, for instance the fault ruptures interaction or the dynamic triggering between two or more seismic sources.’ Excellent point! The text in Section 4.1.3 has been modified to reflect the fact that we do indeed think that the second M5 event was triggered. We have added a new section to the discussion (new section 4.2) that examines patterns common to the Lake Muir sequence and other Precambrian SCR sequences. Excitingly, we find evidence elsewhere that the triggered events can have different failure mechanisms.
- “in Figure 6a there is an east-west oriented fringe interruption at latitude/longitude 6190000/4790000? How the Authors interpret it?” The text of Section 3.2 states “Coherence is also partly lost beneath an approximately 2 km wide (N-S) easterly trending band of pine

forest (see Figures 3 and 6a for location)". The north-south extent of this forest is clearly marked with an arrow labelled "pine forest" on both Figures 3 and 6a. We have added the following text to the caption of Figure 6: The north-south extent of an easterly trending band of pine forest associated with degradation of coherence is indicated with a white arrow in part (a).

- "For a "not Australian" reader is a bit hard to follow the text with the lack of a clear tectonic map containing the bright place names tags." Figure 1 *is* a clear tectonic map as far as stable continental region crust may be divided with respect to seismogenic potential (e.g. Johnston et al 1994; Clark et al. 2012). In the revised manuscript, we have either included all Australian place names mentioned in the text in Figure 1, or written explicit locations into the text itself.

References cited

Townend, J., and Zoback, M. D.: How faulting keeps the crust strong, Geology, 28, 399-402, 2000.

Surface deformation relating to ~~The~~ the 2018 Lake Muir earthquake sequence, southwest Western Australia: ~~rethinking~~ new insight into ~~Australian~~ stable continental region earthquakes

Dan J. Clark[1], Sarah Brennand[1], Gregory Brenn[1], Matthew C. Garthwaite[1], Jesse Dimech[1], Trevor I. Allen[1], Sean Standen[2]

[1] Positioning and Community Safety Division, Geoscience Australia, GPO Box 378 Canberra ACT, Australia
[2] The University of Western Australia, 35 Stirling Hwy, Crawley, Western Australia, Australia

Correspondence to: Dan J. Clark (dan.clark@ga.gov.au)

Abstract. A shallow M_W 5.3 earthquake near Lake Muir in the stable continental region (SCR) crust of southwest Western Australia on the 16th of September 2018 was followed on the 8th of November by a proximal M_W 5.2 event. Focal mechanisms produced for the events suggest reverse and strike-slip rupture, respectively. Field mapping, guided by Sentinel-1 InSAR data, reveal that the first event produced an approximately 3 km-long and up to 0.4-0.6 m high west-facing surface rupture, consistent with reverse slip on a moderately east-dipping fault. The InSAR data also shows that the surface scarp relates to a sub-surface rupture ~5 km long, bound at its north and southern extremities by ~~strike-slip terminal~~bedrock structures. The November event produced a surface deformation envelope that is spatially coincident with that of the September event, but did not result in discrete surface rupture. Almost nine hundred aftershocks were recorded by a temporary seismometer deployment. Hypocentre locations correlate poorly with the rupture plane of their respective main-~~shocks, but~~shocks but correlate well with regions of increased coulomb stress. The spatial and temporal relationships between the $M_W > 5.0$ events, and their aftershocks, reveals dependencies with ~~important~~ implications for how other less well documented SCR earthquake ~~swarms~~sequences could be interpreted. Furthermore, the September M_W 5.3 Lake Muir earthquake was the ninth event documented to have produced surface rupture in Australia in historical times. These nine ruptures are located exclusively in the Precambrian non-extended SCR rocks of central and western Australia, and none could have been identified and mapped using topographic signature prior to the historical event. ~~A pattern is emerging where 'one-off' ruptures, as evidenced by the historic surface breaking earthquakes, are filling the spaces between mapped multi-event neotectonic scarps.~~ Consistent, though fragmentary, evidence exists from analogous regions worldwide. Our analysis of the Lake Muir earthquake sequence therefore provides constraint on models describing mechanisms for strain accumulation and localized release as earthquakes in non-extended SRC crust.

~~Modern geodetic and seismic monitoring tools are enabling the study of moderate-sized earthquake sequences in unprecedented detail. Here we use a variety of methods to examine surface deformation caused by a sequence of earthquakes near Lake Muir in southwest Western Australia in 2018. A shallow MW 5.3 earthquake on the 16th of September 2018 was followed on the 8th of November 2018 by a MW 5.2 event in the same region. Focal mechanisms for the events suggest reverse and strike-slip rupture, respectively. Interferometric Synthetic Aperture Radar (InSAR) analysis of the events suggests that the~~

ruptures are in part spatially coincident. Field mapping, guided by the InSAR results, reveals that the first event produced an approximately 3 km long and up to 0.5 m high west facing surface rupture, consistent with slip on a moderately east dipping fault. Double difference hypocentre relocation of aftershocks using data from rapidly deployed seismic instrumentation confirms an east dipping rupture plane for the first event, and shows a concentration located at the northern end of the rupture where the InSAR suggests greatest vertical displacement. The November event resulted from rupture on a northeast trending strike slip fault. UAV derived digital terrain models (differenced with pre event LiDAR) reveal a surface deformation envelope consistent with the InSAR for the first event, but could not discern deformation unique to the second event. New rupture length versus magnitude scaling relationships developed for non extended cratonic regions as part of this study allow for the distinction between "visible" surface rupture lengths (VSRL) from field mapping and "detectable" surface rupture lengths (DSRL) from remote sensing techniques such as InSAR, and suggest longer ruptures for a given magnitude than implied by commonly used scaling relationships.

1 Introduction

Within the stable continental regions (SCRs) of the world, defined by Johnston et al. (1994) as "areas where the continental crust is largely unaffected by currently active plate boundary processes", large and potentially damaging earthquakes are rare (Johnston, 1994b; Schulte and Mooney, 2005). Consequently, mechanisms for strain accumulation and localized release as earthquakes are poorly understood (Talwani, 2014; Calais et al., 2016; Craig et al., 2016; Liu and Stein, 2016; Salditch et al., 2020) and the epistemic uncertainty associated with fault--displacement hazard (e.g. Moss and Ross, 2011; Moss et al., 2013), and the recurrence and fault--source model components of seismic--hazard assessments (e.g. Stein, 2007; Leonard et al., 2014; Griffin et al., 2020; Allen, 2020), is large. Constraint can be provided by the analysis of moderate--magnitude historical earthquake sequences supplemented by the paleoseismic record of large, surface-deforming events. Historical surface-deforming earthquakes are particularly valuable in this respect in that they allow for more robust interpretation of the paleoseismic record (e.g. through calibration of scaling relationships between surface rupture length and earthquake magnitude; Wells and Coppersmith, 1994; Clark et al., 2014b), and a broad range of tools exist with which to characterize the surface deformation and so deduce source properties (e.g. interferometric synthetic aperture radar (InSAR), and pixel tracking techniques for determining vertical and horizontal co-seismic displacements; Massonnet et al., 1993; Klinger et al., 2018; Zhou et al., 2018; Gold et al., 2019).

Broad agreement exists that SCR crust is not homogeneous with respect to seismogenic potential (Johnston, 1994a; Mooney et al., 2012; Clark et al., 2012). The majority of historical moment release in SCR settings is preferentially located in failed rifts of Cretaceous to Paleogene age (e.g. Johnston, 1994a; Schulte and Mooney, 2005; Bonini et al., 2012; Talwani, 2014), and associated with pronounced lateral gradients in lithospheric thickness such as at the boundaries of cratons (e.g. Mooney et al., 2012) (Table 1). The largest recorded historical SCR earthquakes have occurred in failed rift settings; within the Reelfoot Rift (Mueller and Pujol, 2001) and the Rann of Kachchh (Rajendran et al., 2008). While typically being characterized by a lack of significant neotectonic relief (White et al., 2009; Talwani, 2014; Goedhart and Booth, 2016; Hornsby et al., 2019), there are notable exceptions where evidence is preserved for strain localization over many seismic cycles; typically, but not exclusively associated with the bounding faults of the failed rifts. Examples include the Rann of Kachchh of India (Rajendran et al., 2008; Rastogi et al., 2014), the Tapti Fault in peninsular India (Copley et al., 2014), the Reelfoot Rift in the central United States (van Arsdale, 2000; Cox et al., 2013), and the Otway, Flinders and Strzelecki ranges of eastern Australia (Sandiford, 2003a, b; Celerier et al., 2005; Quigley et al., 2006; Hillis et al., 2008; Braun et al., 2009; Clark et al., 2012) (Figure 1).

While accounting for less than 10% of historical global SCR moment release (Schulte and Mooney, 2005), non-extended SCR crust accounts for more than two-thirds of the surface deforming earthquakes documented (Table 1), and is locally associated with a rich paleoseismic record (e.g. Crone and Machette, 1995; Rajendran et al., 1996; Crone et al., 2003; Wheeler, 2006; Clark et al., 2008; Estrada, 2009; Quigley et al., 2010; Clark, 2010; Clark et al., 2012; Clark et al., 2015; Zellman and Ostenaa, 2016). Within the Australian SCR, Leonard et al. (2014) divided the non-extended part into Precambrian and Phanerozoic ~~parts~~elements based on differences in seismogenic potential implied by the character of neotectonic features (after Clark et al., 2012; Figure 1). The older crust was ~~considered to have~~associated with a lower seismogenic potential consistent with the hypothesis proposed by Mooney et al. (2012), that seismogenic potential is inversely proportional to lithospheric thickness. Perhaps counter-intuitively, the historical record of seismicity and of surface rupture~~,~~ is particularly rich in the Australian Precambrian non-extended SCR (Leonard, 2008; Clark, 2010; Leonard and Clark, 2011), which has hosted nine of the ~~twelve~~fifteen historical earthquakes documented to have produced surface ruptures in SCR crust globally (Table 1, Figure 1). In this paper we report on the geological setting and characteristics of the most recent of the nine surface rupturing earthquakes in the Australian Precambrian SCR crust; the 2018 M_W 5.3 Lake Muir earthquake. The earthquake was followed by an extensive aftershock swarm, and ~~after 51 days by~~ a proximal M_W 5.2 earthquake 51 days after the 16th September event, ~~-~~which deformed but did not break the surface. InSAR observations of surface deformation relating to both M_W >5.0 events were validated using field observations, unmanned aerial vehicle (UAV)-acquired high resolution digital elevation data, and hypocentres calculated from a local seismic network deployed in the days following the first, M_W 5.3, event. Analysis of the Lake Muir earthquake sequence provides guidance as to how other moderate to large magnitude SCR seismic sequences might be interpreted (e.g. Adams et al., 1992; Bent, 1994; Baumbach et al., 1994), and further constraint for models describing localized strain release as earthquakes in non-extended SCR crust worldwide.

~~In Australia, nine earthquakes are known to have produced surface rupture in historical times (Table 1, Figure 1). These ruptures are located exclusively in the Precambrian cratonic crust of central and western Australia (Clark et al., 2014a), and are associated with moment magnitude (M_W) events in the range of 4.73 – 6.76~~ (Clark et al., 2014b; Clark and Allen, 2018)~~. The 2007 Katanning M_W 4.73 event was the first earthquake in Australia where the surface deformation field was imaged by InSAR (Dawson et al., 2008), a technique which enables the mapping in unprecedented detail of surface deformation relating to moderate to small, shallow earthquakes (Dawson and Tregoning, 2007); much greater than could be mapped on the ground using traditional paleoseismological means. The InSAR results for the Katanning event, derived from Japanese ALOS-PALSAR data, showed surface deformation along a linear front ~1.26 km in length, of which 0.2 km was recognisable on the ground as a scarp up to 0.1 m high (Vic Dent, pers. comm. 2007). This finding dramatically reduced the expected threshold magnitude for surface rupture in cratonic Australia, and offered a means of gaining a more comprehensive understanding of the structural and seismotectonic context, and the landscape effects, of the remarkably shallow intraplate ruptures experienced in cratonic Australia. In this paper we report on the geological setting and characteristics of the surface deformation relating to two M_W >5.0 earthquakes that occurred in 2018 near Lake Muir in the southwest of Western Australia, as imaged using Sentinel-1 InSAR data. The InSAR observations of surface deformation were validated using field observations, unmanned aerial vehicle (UAV) acquired high resolution digital elevation data, and hypocentres calculated from a local seismic network deployed in the days following the first, M_W 5.3, event.~~

1.1 The Lake Muir Earthquake Sequence

The M_L 5.7 (M_W 5.3) Lake Muir earthquake occurred at 04:56:24 (UTC) on 16th September 2018 in a rural area of southwest Western Australia, ~60 km east of the town of Manjimup, and a similar distance north of the town of Walpole (Figure 2). Approximately 20 km from the epicentre, relatively modest Modified Mercalli Intensity (MMI) values of VI were reported (Allen et al., 2019). With the exception of one unoccupied dwelling in the immediate epicentral area, which was extensively damaged, only minor damage and no injuries were reported. The event was widely felt throughout the Perth Basin, including the Perth metropolitan region, over 300 km away. Focal mechanisms suggest a reverse faulting mechanism, with a minor dextral transcurrent component, and moderately east and northwest dipping nodal planes (Figure 2, Table 2). Geoscience Australia recorded a magnitude M_L 3.4 foreshock three days prior to the main shock. A protracted aftershock sequence, comprising hundreds of located events, was punctuated by a M_L 4.~~7~~ 6 event on 12th October at 16:31:30 (UTC) (Figure 3, Table 2). Almost two months after the 16th September M_W 5.3 event, a M_L 5.4 (M_W 5.2) event occurred on the 8th November at 21:07:01 (UTC). Within the error estimates of the original hypocentral determinations, this event was co-located with the 16th September event (see weblinks in Table 2). The focal mechanisms calculated for the November event indicate predominantly dextral strike-slip faulting, with steeply northwest and southwest dipping nodal planes. The percentage double-couple from the U.S. Geological Survey (USGS) W-phase moment tensor solution is 31% (Figure 2, Table 2). This event was felt much more strongly and widely than the slightly larger first event, with MMI of VII to VIII being recorded close to the epicentre. There are several factors that might explain the relatively greater number (and density) of felt reports from the 8th November

earthquake, including: 1) the time of day, which was early morning, when people are more likely to be stationary and thus more likely to perceive ground shaking; 2) differences in the ground motion radiation pattern and/or stress drop of the earthquake that may have yielded greater shaking in population centres at perceptible frequencies; and/or 3) greater community awareness of the earthquake sequence and where to find sources of further information. Surface rupture relating to the September event was initially identified with InSAR (Figure 2), and has been subsequently verified by ground survey (this paper).

1.2 Geological and seismotectonic setting of the Lake Muir earthquake sequence

The Lake Muir earthquake sequence occurred within 1700-1600 Ma rocks of the Biranup Zone of the Proterozoic Albany Fraser Orogen (Fitzsimons and Buchan, 2005; Spaggiari et al., 2009) (Figure 2). During the Mesoproterozoic Albany Fraser ~~orogeny~~ Orogeny these rocks were thrust to the north over the 3000-2600 Ma rocks of the Northern Foreland of the Albany Fraser Orogen (the portion of the Archaean Yilgarn Craton that was reworked during the Albany–Fraser Orogeny) along moderately south-dipping faults. In the Lake Muir region, the dominant east to east-southeast striking structural grain is associated with the major structures bounding these thrust sheets. East-striking structural and lithological trends relating to the Albany Fraser Orogen are ~~cut~~ transected by northwest trending structures related to Proterozoic to earliest Phanerozoic movement on the Darling Fault Zone to the west (Janssen et al., 2003). The Boyagin dyke swarm cuts across much of the southwest, including the Yilgarn Craton and Albany–Fraser Orogen (Prider, 1948; Myers, 1990a; Harris and Li, 1995), and is subparallel to this structural trend. Minor north- and northeast-trending structures may relate to Gondwana breakup or later movement focused on the Darling Fault, parallel structures to the west thereof (e.g., the Dunsborough and Busselton faults), and associated oblique structures (Harris, 1996; Olierook et al., 2015). Eocene alluvial sediments (Werillup Formation) and marine siltstone and sandstone (Pallinup Formation) locally infill topography in the crystalline basement (Wilde and Walker, 1984). Deposits have been correlated to map a Paleogene paleo-channel system (Smith, 2010). These sediments, and ferricrete developed within them, are reported to be locally faulted by up to 5-7 m vertically based upon evidence from drill holes (Chakravartula and Street, 2000; Smith, 2010). The sparsity of boreholes precludes determination of fault orientation.

The Lake Muir region lies near to the southern boundary of a broad band of relatively high seismicity crossing the southwest corner of Western Australia known as the Southwest Seismic Zone (SWSZ, Doyle, 1971), which is one of the most seismically active regions in Australia (e.g. Leonard, 2008; Allen et al., 2018). Earthquake activity in the SWSZ appears to have increased significantly since the 1940s (Leonard, 2008), and it has generated five of the nine known Australian historic surface ruptures (all associated with reverse faulting, Table 1). In addition to large shallow events and scattered smaller events, the SWSZ has produced several dozen earthquake swarms in the last 40 years, including the Burakin swarm of ~~2001~~2000-2002 during ~~which~~ where ~18,000 events of mixed focal mechanism (including six events in the magnitude range M_W 4.0-4.6~~three above M_L 5.0~~) were recorded in a period of only a few months (Leonard, 2002; Allen et al., 2006; Dent, 2016). While most swarm centres occur within the SWSZ, they have a broader distribution across the southwest of Western Australia ~~(Dent, 2016),~~ (Dent, 2016); an essentially random pattern that is similar to fault scarps relating to pre-historical events (Clark, 2010; Clark et al., 2012).

The relatively uniform spatial distribution of north-trending reverse fault scarps is consistent with scarp formation under conditions imposed by the contemporary east-west oriented compressive crustal stress regime (e.g. Rajabi et al., 2017b), and suggests that seismogenic strain release is uniformly distributed over the Yilgarn Craton over the timescale recorded in the land surface (*ca.* 100 kyr or more) (Leonard and Clark, 2011).

1.3 Landscape context of the Lake Muir earthquake sequence

Interrogation of a 2012 LiDAR dataset (see Supplementary Information) revealed the presence of ~~grain~~ an alignment of valleys and ridges ~~in the landscape~~ that mimics structural trends evident in the continental- and regional-scale magnetic data (cf. Figures 2 and 3) (Chakravartula and Street, 2000; Milligan and Nakamura, 2015). The main ridge-line, valley and drainage trends in the study area are broadly to the east-southeast and north, with a subordinate northwest trend (black double-ended arrows in Figure 3). Ridges are subdued, broad and undulating. Valley floors are flat-bottomed, and are locally occupied by lakes and swamps, implying the presence of significant ~~alluvial or~~ sedimentary infill (cf. Commander et al., 2001; Smith, 2010). Lunettes are developed on the east and southeast sides of most lakes, often with evidence for minor remobilisation into parabolic dunes. Knick-point retreat from a regional topographic low to the southwest occupied by Lake Muir is observed in several instances to be rejuvenating the drainage within flat-bottomed valleys, resulting in the removal of valley-fill sediments and the accentuation of structural trends evident in the alignment of adjacent linear ridges. There is no ~~obvious~~ landscape evidence for sharp vertical dislocations of valley floor sediments that might relate to Late Pleistocene or Holocene surface-rupturing seismic events.

2 Methods

2.1 InSAR processing method

Since the 1992 M_W 7.3 Landers earthquake (Massonnet et al., 1993), remote sensing techniques have been shown to be valuable tools for observing surface deformation and damage patterns relating to earthquakes in a range of tectonic settings (e.g. Livio et al., 2017; Klinger et al., 2018; Wang et al., 2019; Gold et al., 2019; Scott et al., 2019). Interferometric Synthetic Aperture Radar (InSAR) in particular has greatly improved the detectability of surface faulting, and surface deformation, especially relating to small to moderate sized earthquake sequences in remote or poorly instrumented areas, such as SCRs (Satyabala, 2006; Dawson et al., 2008; Amarjargal et al., 2013; Livio et al., 2017; Gardonio et al., 2018). Surface deformation relating to eleven SCR earthquakes has been imaged using InSAR (Table 1). Following the launch of Sentinel-1A and Sentinel-1B missions in 2014 and 2016 respectively, there is now a near-global coverage of SAR acquisitions every 12 days (https://sentinel.esa.int/web/sentinel/missions/sentinel-1/overview). The availability of this rich data set has enabled global systematic studies of earthquake detectability in InSAR data (e.g. Barnhart et al., 2019; Funning and Garcia, 2019) and, for the first time in an SCR setting, has allowed us to construct coseismic interferograms for two events within the same SCR seismic sequence.

For each of the two earthquake events we generated a coseismic interferogram from two Sentinel-1 interferometric wide swath SAR images (earthquake 1: 14th and 26th September 2018; earthquake 2: 1st and 13th November 2018) using a standard interferometric SAR processing workflow implemented with the Gamma software (Wegmüller and Werner, 1997). The topographic component of the phase signal was removed using a 1-arc second SRTM digital elevation model (Geoscience Australia, 2011) and the orbital component was removed using Precise Orbital Ephemerides (~~POD~~POE) products. Each interferogram was sub-sampled (multi-looked) eight times in range and two times in azimuth to reduce phase noise. An adaptive spatial filter (Goldstein and Werner, 1998) with exponent 0.5 was applied to each interferogram to further reduce phase noise prior to automatic unwrapping using a minimum cost flow algorithm (Costantini, 1998). The automatically unwrapped interferogram for the September earthquake had significant errors due to poorer phase coherence around the surface rupture zone. A manual approach to unwrapping this interferogram was therefore applied using the branch-cut method (Goldstein et al., 1988).

2.2 Field observation and UAV digital terrain models

The epicentral region of the earthquakes were visited over three days (12-14th November 2018), less than a week after the November event. The scarp produced by the September event was mapped, and evidence for rejuvenation of the scarp during the November event was assessed. A hand trench was excavated across the central section of the September scarp to assess fault dip and displacement.

Because InSAR captures a single displacement vector in the radar line of sight (LOS), and commonly decorrelates in regions close to earthquake surface ruptures where displacement gradients exceed the Nyquist sampling rate or cause pixels to no longer overlap (e.g. Hamling et al., 2017; Metzger et al., 2017; Gold et al., 2019), it is desirable to obtain independent validation data. In order to recover part of the surface vertical deformation envelope associated with the events, aerial photographs were acquired with a DJI Phantom 4 unmanned aerial vehicle (UAV) ~~UAV~~ in an approximately 500 m-wide swath along a 2 km length of the September event scarp. An approximately 2 km-long cross-line was also flown, extending eastward from the scarp across the region of most significant surface deformation indicated in the InSAR imagery (Figure 3). Ground control was provided by an RTK GPS, with mean horizontal and vertical measurement uncertainties of 0.026±0.025 m and 0.056±0.~~055~~ 055 m, respectively. A third mission covered the southern extent of surface deformation indicated in the InSAR imagery (~~Figure~~ Figure 3). The results of this mission are presented in the Supplementary Information (Figure S1).

The image dataset was processed using a Structure-from-Motion (SfM) and multi-view stereo approach, implemented in the software Agisoft Photoscan Pro 1.4.3 (Agisoft LCC). The resulting dense point cloud achieved a standard deviation of the location differences between it and the control points of 0.09 m in the horizontal and 0.01 m in the vertical, which is comparable to other studies using similar ground control point (GCP) densities (e.g. Gindraux et al., 2017). Several studies of factors impacting local photogrammetry-derived Digital Terrain Model (DTM) accuracy (e.g. Tonkin and Midgley, 2016; Gindraux et al., 2017) report a vertical accuracy decrease of ~0.1 m for every 100 m increase in the distance to the closest GCP. In our

study the maximum distance from a control point is in the order of 200-300 m. A 6 cm-resolution DTM was produced from the dense point cloud.

The elevation values from a LiDAR dataset collected by the Western Australia Government Department of Biodiversity, Conservation and Attractions in 2012 were subtracted from the UAV DTM produced in this study, to produce a ~~DEM~~ DTM of difference (DoD, Williams, 2012). The average magnitude of the uncertainties associated with the elevation values for the LiDAR dataset is reported as 0.063±0.074 m. The combined location uncertainty in the DoD might therefore be expected to be in the order of 0.1 - 0.2 m. Details of the processing steps are presented in the Supplementary Information.

The focal mechanism computed for the September earthquake (Figure 2) indicates almost pure reverse motion. In this instance, the majority of landscape change would be expected to be vertical, and so detectable in the DoD. In contrast, the November earthquake was dominantly strike-slip (Figure 2). The deformation envelope detectible with the deployed technologies should therefore relate almost exclusively to the September reverse faulting event, with further deformation from the November event remaining largely undetected. To quantify vertical surface displacement associated with the September earthquake, we extracted swath profiles through the DoD (and the unwrapped InSAR images) parallel and perpendicular to the rupture using swath profiler tool for ESRI ArcGIS (Pérez-Peña et al., 2017). The swath profiles sample the topography perpendicular to the profile to a set distance either side of the profile line. A range of statistics (percentiles, quartiles, max/min/mean) might then be assessed in order to account for the noisy character of the UAV-derived DTM.

2.3 Rapid deployment aftershock kits

Within five days of the 16th September event five seismic rapid deployment kits (RDKs) and three GPS kits were deployed in the epicentral region (Figure 2). The seismic sensors included four short-period Lennartz LE-3Dlite seismometers and one Trillium Compact seismometer. The short-period instruments were paired with Nanometrics Titan accelerometers recording at 200 Hz to capture any strong ground motions from the aftershock sequence. The RDK locations (prefixed LM on Figure 2) were selected to maximise azimuthal coverage of the study area taking into account the location of one permanent Australian National Seismic Network (ANSN) station near Rocky Gully (RKGY), fortuitously located 24 km from the epicentre of the 16th September earthquake. The network geometry also considered the capture of ground-motion data at a range of source-receiver distances for subsequent attenuation studies. One RDK (LM01) was deployed at the initial epicentral location of the 16th September event. Waveform data were telemetered in real-time to the National Earthquake Alerts Centre at Geoscience Australia to support real-time aftershock detection and analysis. The RDK locations therefore required adequate connection to local 3G and 4G telecommunication networks. Additional factors considered in the deployment configuration were the local site geology, availability of sunlight to power the sensors, and land access.

The three GPS kits were deployed on existing survey marks within a broader network covering the SWSZ, one of which was last occupied in 2012. The survey marks used (SWSZ45, SWSZ46, SWSZ48) were approximately 36, 65 and 25 km away from the epicentral region, respectively (Figure 2). Processing of the acquired GPS data from the SWSZ46 site produced an anomalous vertical displacement signal indicating 12 mm of subsidence. This signal could not be reconciled with the surface

deformation related to the earthquakes, which was constrained to a near-field region smaller than 10 km from the surface rupture (Figure 2), and so is not discussed any further here.

3 Results

3.1 Field observations

Initial reports from local residents following the September earthquake indicated the presence of west-facing fault scarps intersecting several farm tracks (e.g., Figure 4a), loss of tension in an east-west running fence line (GDA94/MGA50, 479590 mE, 6192140 mN), and cracking in farm dam walls related to lateral spreading (Figure 4b). Field investigation demonstrated that the track intersections could be linked to form an approximately 3 km-long, concave-to-the-east, west-facing crescentic scarp (Figure 3). In detail, the scarp comprises a series of left and right stepping *en echelon* segments 100 – 200 m long. In the central 2 km of the scarp, each segment is associated with up to 20 – 40 cm of vertical displacement (Figure 4c, 4d). The morphology of individual scarp segments show little evidence for a strike-slip component to motion, varying between discrete thrust surface rupture with local fault-parallel folding and cracking, to discrete thrust surface rupture with mole tracks (cf. Lin et al., 2004) and extensional fissuring associated with topographic bulges. Where the scarp crossed drainage lines, presumably associated with metres of sandy alluvial sediments, it becomes a broad warp, often associated with extensional fissuring parallel to the warp-crest, and warp-perpendicular cracking at step-overs.

A hand trench 2.3 m long and 1.2 m deep was excavated perpendicular to the scarp trace at a location where the vertical displacement was in the order of 0.3 – 0.4 m (Figures 4c & 5). Here, the scarp has an average trend of ~~0~~25°, and scarp segments are right stepping (GDA94/MGA50, 479290 mE, 6191500 mN). The exposed stratigraphy consists of an approximately 0.10-0.12 m thick organic-rich grey brown silty sand overlying ~0.4 m of pale grey medium sand that becomes pisolitic with depth (Figure 5b,c). This layer in turn overlies an orange/red mottled grey clayey sand to the bottom of the trench. We interpret the profile to reflect an *in-situ* weathering profile developed in Albany-Fraser Orogen bedrock. Approximately 0.18-0.20 m of the pre-event organic-rich sandy soil had been over thrust along a 20° east-dipping reverse fault that steepened to 30° towards the base of the trench (Figure 5c). A vertical scarp-parallel tension fissure ~0.7 m east of the trench suggests that the fault dip steepens again at shallow depth (Figure 4c). Drag of layering in the hanging wall along the fault resulted in the formation of a prominent hanging-wall fold. The total vertical deformation at this site is shared approximately equally between discrete slip across the fault plane and folding.

South of 479130 mE, 6191120 mN (GDA94/MGA50) the scarp steps 50 m to the west, the general scarp strike is 355°, and scarp segments become left-stepping. The scarp is associated with a 0.2 – 0.3 m vertical landscape step which extends some 400 m south from this location, before entering dense pine plantation and becoming difficult to follow due to extensive landscape disturbance (e.g., furrowing), and a thick layer of organic matter cloaking the ground surface (Figure 4d). Within the pine forest, the scarp maintains a vertical displacement of 0.2 – 0.4 m, before stepping again 50 m to the west at 479190 mE, 6190050 mN (GDA94/MGA50).

The segments south of the step-over strike ~340 – 350° and decrease in vertical displacement from ~0.3 m to ~0.1 m at the most southerly intersection of the scarp with a farm track (GDA94/MGA50, 479320mE, 6189440mN). At this track intersection, observed after the November event, the scarp comprises dominant southeast-trending elements which are locally offset (left-stepping) across east-trending lineaments. These become tensional fissures on the eastern up-thrown side of the scarp. The vertical displacement across the scarp at this location is approximately 0.1 m. Landowners report that there was a 'freshening' [rejuvenation] of the scarp at this location following the November event. The presence of fine cracking details in November, given there were significant rainfall events in October, support these anecdotes. The observations are consistent with a reverse oblique (sinistral) reactivation of this segment of the scarp. South of the track intersection, the scarp is lost in bushland. However, heavy tree limb fall, and the occasional toppled tree, was observed along strike for a further ~ 400 m to the southeast, suggesting strong localised ground shaking during the September event (Figure 3).

3.2 Wrapped and unwrapped Sentinel-1 interferograms for both events

The wrapped interferogram for the September event shows an extent of surface deformation ~ 12 km in an east-west direction and ~ 8 km in a north-south direction (Figures 2, 6a). A linear surface deformation front relating to the rupture can be traced for approximately 5 km. The central ~3 km corresponds to the fault scarp mapped on the ground. The unwrapped interferogram (Figure 6b) shows a broad shallow lobe of negative line of sight (LOS) change that extends from the west to the surface scarp (equivalent to ~2.5 fringes in the wrapped image). From the east, a broad shallow lobe of positive LOS change (~2 fringes in the wrapped image) transitions to a tight (~1.5 km wide) band of negative LOS change characterised by at least 10 fringes. The images lose coherence in the 200 – 300 m east of the scarp, and in proximity to Lake Noobijup (cf. Figure 3). Coherence is also partly lost beneath an approximately 2 km wide (N-S) easterly trending band of pine forest (see Figures 3 and 6a for location).

The unwrapped interferogram for the September event (Figure 6b) shows a maximum LOS displacement towards the satellite of approximately 0.20 – 0.24 m along the eastern side of the central ~1.5 – 2.0 km of the scarp. These values are approximately half the maximum scarp height recorded by UAV field measurement, and approximately one third the maximum magnitude of slip along the fault plane that might be calculated from the trench exposure (see also next section). The southern 1.3 km of scarp mapped on the ground occurs mainly beneath pine forest and the unwrapping algorithm failed to reproduce measured scarp heights of 20 – 40 cm in this area. Similarly, the unwrapping algorithm performed poorly in the swampy vegetated land proximal to Lake Noobijup.

The hanging wall uplift diminishes to the east of the scarp and is fringed by a broad region of positive LOS change, corresponding to depression of the land surface. The deepest region of depression of the ground surface is centred on Lake Noobijup (~ 13 cm LOS increase). This area also corresponds to the highest density of aftershocks following the September mainshock (Figures 3 and 6b). The depressed region has well-defined northern and southern extents, terminating at east ~~to~~ and south-east trending structures, respectively. ~~The orientation of these structures suggests that they might have~~

~~accommodated a significant strike-slip component to motion, in addition to vertical motion.~~ The areal extent of the depressed region is surprisingly large for a reverse fault rupture (cf. King et al., 1988; Ellis and Densmore, 2006).

The InSAR images for the November event (Figures 6c & d) exhibit the classic quadrupole pattern of an almost pure strike-slip rupture, and are consistent with a maximum of ~5 – 8 cm of right lateral slip having occurred at the surface relating to rupture of a northeast-trending, steeply northwest dipping fault. This contrasts with the focal mechanism for the event, which suggests an oblique compressive rake (Figure 2). Although the deformation pattern shows a sharp linear discontinuity for ~ 1 km either side of the intersection of the November failure plane with the September rupture plane, simple forward modelling using a finite rectangular elastic dislocation model (Okada, 1985) suggests that a discrete surface rupture may not have been produced (i.e., the rupture tip remained buried) (Figure S~~3~~4). Indeed, structures unambiguously relating to the main rupture were not observed in the field. Potential evidence for secondary surface deformation relating to the main failure plane of this event was seen as a series of 'fresh' looking east-trending left-stepping dilatational cracks expressed in a boundary track at 478970 mE, 6190390 mN (GDA94/MGA50). No vertical displacement was observed to be associated with these features.

The deformation pattern relating to the November event is also seen to be influenced by the northwest trending structure that forms the southern termination of the September event. This lineament is discernible in the November event unwrapped InSAR from the intersection of the surface projection of the rupture planes to approximately 1.8 km southeast (Figure 6d). Minor reverse-oblique movement on this structure during the November event may have been responsible for the reports of a local 'freshening' of the September scarp.

3.3 Comparison of UAV-derived and InSAR-derived deformation surfaces

Part of the vertical displacement envelope resulting from the September earthquake was recovered by differencing the DTM acquired by UAV and the 2012 LiDAR dataset (Figure 7; see Section 2.2 and Supplementary Information for methods). Scarp-parallel and perpendicular profiles through the resulting DTM of difference (DoD) ubiquitously show a larger displacement magnitude than the InSAR-derived LOS displacement estimates (Figure 7b, c). However, the general form of the two deformation envelope estimates is consistent. A broad uplifted region to the east of the scarp trace in the DoD corresponds to the area of greatest uplift evident in the InSAR data (Figure 7a). Further, the InSAR LOS phase image indicates that the eastern end of the DoD profile is located in a broad region of topographic depression relative to the far field (~2 fringes), while the western end is raised relative to the far field (~2.5 fringes) (cf. Figure 7c blue line and Figures 6a and b). This is reflected in a ~0.3 m vertical difference between eastern and western ends of the UAV DoD profile.

Importantly, the UAV DoD captures deformation close to the scarp trace where the InSAR images lose coherence. For example, the InSAR data did not image a ~ 0.1 m deep foot-wall depression that occurs within ~100 m to the west of the scarp trace. Along the ~2 km length of scarp that was covered by the UAV DoD, the average height of the scarp, as measured along a 100 m-wide swath profile (Figure 7b), is 0.46 ± 0.11 m. The landscape dislocation is shown to be sharpest in the ~10-30 m east of the scarp trace, and consistent in magnitude with that measured by RTK GPS at the location of the trench (cf. Figures 5 and 7c). The topography then continues rising at a lower rate to a maximum vertical displacement within ~200 m east of the

scarp trace, before falling relatively smoothly over a kilometre (Figure 7c). The fact that uplift associated with the fault tip is distributed over the ~200 m east of the scarp trace suggests that the scarp-parallel DoD swath profile, spot measurements of scarp height (green dots in Figure 7b), and the 2-D UAV profiles (red dots in Figure 7b), all underestimate total vertical deformation to some degree. A similar result was derived for the 2018 Petermann Ranges earthquake surface rupture (Gold et al., 2019).

No surface expression or ground cracking was observed on the ground along the southeast-trending feature imaged in the InSAR-derived LOS displacement data at the southern end of the September rupture (cf. Figure 6b). However, a DoD constructed over the area (see Figure 7a for mission outline, and Figure S1 for results) revealed the presence of a very subtle (≤5 cm high) linear topographic feature, extending over ~560 m, which was coincident with the surface displacement implied by the InSAR data (Figure 7b).

~~The vertical displacement envelope resulting from the September earthquake was recovered by differencing the UAV DTM and the 2012 LiDAR, producing a DTM of difference (DoD) (Figure 7; see also Supplementary Information). The 1st and 3rd quartile values (Figure 7c) show that within the 100 m wide swath of the profile, elevation values from the UAV derived DTM are consistently within 0.1 m of the LiDAR dataset. In general, the UAV DoD (Figure 7a,c) shows a broad uplifted region to the east of the scarp trace, which reduces in amplitude relatively smoothly towards the east. Within the ~100 m west of the scarp the land surface has been depressed into a ~ 0.1 m deep foot wall depression, before rising again further west. There is a ~0.3 m vertical difference between eastern and western ends of the UAV DoD profile.~~

~~Comparison against the InSAR derived LOS displacement data (cf. Figure 7c blue line and Figures 6a and b) suggests that the eastern end of the DoD profile is located in a broad region of topographic depression (~2 fringes), while the western end is raised relative to the far field (~2.5 fringes). Scarp parallel and perpendicular profiles through the InSAR derived LOS displacement data ubiquitously show a smaller displacement magnitude than the vertical deformation estimates from the UAV DoDs (Figure 7b,c).~~

~~Along the ~2 km length of scarp that was covered by the UAV DoD, the average height of the scarp, as measured along a 100 m wide swath profile (Figure 7b), is 0.46 ± 0.11 m. Note that at the intersection of the scarp perpendicular profile and the scarp parallel profile, the scarp parallel profile under estimates the true vertical deformation by up to 0.1 m. This is the result of deformation being locally distributed up to 100 – 150 m from the scarp front (e.g., Figure 7c). While the full envelope of deformation has been captured within the uncertainty bounds of the swath measurements, it can be anticipated that spot height measurements, and to a lesser degree UAV 2 D profiles, might also locally underestimate vertical deformation as variability along and across strike is not sampled (Figure 7b).~~

~~No surface expression or ground cracking was observed on the ground along the southeast trending feature imaged in the InSAR derived LOS displacement data at the southern end of the September rupture (cf. Figure 6b). However, a DoD constructed over the area (Figure 7a, and Supplementary Information) revealed the presence of a very subtle (≤5 cm high)~~

~~linear topographic feature, extending over ~ 560 m, which was coincident with the surface displacement implied by the InSAR data (Figure 7b).~~

3.4 Mainshock and ~~Aftershock~~ aftershock relocation

In the period from 16th September to 23rd November, 884 earthquakes were recorded on stations from the permanent ANSN network and the five rapid-~~-~~deployment aftershock kits temporarily installed in the epicentral region. These events include the largest aftershock (13~~2~~th October, M_L 4.~~7~~6), and the November M_W 5.2 event. Initial locations for these events were computed using the SeisComP3 seismological software (Weber et al., 2007) and the LocSAT location algorithm (Bratt and Bache, 1988). *P*- and *S*-wave arrival times were manually picked and reviewed by Geoscience Australia seismic analysts. The mean location uncertainties in this dataset were found to be 3.39 km in the horizontal direction, and 2.33 km in the up direction. To better constrain the location and pattern of aftershocks, events from this dataset were input for relocation using the HypoDD double-difference relative location algorithm (Waldhauser and Ellsworth, 2000), implemented in the software HypoDDpy (Krischer, 2015) (see Supplementary Information for detail). The HypoDD algorithm minimizes errors in hypocentral locations that are commonly attributed to uncertainties in Earth structure along the event-station ray path. The final relocation included a subset of 470 events from this catalogue (Figures 3 and S2). The mean location uncertainties in the relocated dataset were found to be 63 m, 116 m, and 228 m in the east, north and up directions, respectively.

Both the largest aftershock (M_L 4.~~7~~6) and the November M_W 5.2 event did not meet criteria for relocation in HypoDD using nearby seismic stations. However, both events were clearly recorded with good azimuthal coverage at regional and teleseismic distances. Based on waveforms from 19 stations in Australia, Antarctica, Kazakhstan, Mongolia and Thailand a separate relative location of these two events was calculated, together with the September M_W 5.3 main shock, by manually aligning the distant waveforms and performing a Joint Hypocentre Determination (Pujol, 2000; Fisk, 2002; see Supplementary Information for detail). The September and November earthquakes were then anchored to the M_L 4.~~7~~6 aftershock location, which was well constrained in an absolute sense, as it occurred within ~0.6 km of the LM01 seismograph station. In this way a better estimation of the absolute location of the point of initiation for both the September and November earthquakes was produced (Table 2). For calculations, the depths for all three~~3~~ events were fixed to 2 km. This is justified in that the calculations were performed using P phases from regional and teleseismic stations, so the epicentral solutions are fairly insensitive to depth. The depth estimates presented in Table 2 relate to the initial locations calculated using the permanent ANSN network, which was supplemented by the five rapid deployment aftershock kits for the latter two events.

The relocated position of the September M_W 5.3 epicentre is seen to coincide with the region of most prominent surface uplift imaged in the unwrapped InSAR image (Figure 6b), and the greatest scarp height (Figure 7a). Aftershock ~~Epicentres~~ epicentres occurring in the interval between the September and November main shocks are located predominantly east of the line of the surface rupture (Figure 6a, b). The associated hypocentres occur ~~in a band~~ between ~1.5 km and 4 km depth, and below a plane extending from the trailing edge of the surface rupture dipping at ~~30~~50° to the east (Figure 8). ~~Although c~~Considerations of the preservation of seismic moment (i.e. M0 = shear modulus x fault area x average displacement, Hanks and Kanamori, 1979)

suggest that the September rupture is unlikely to have extended beyond ~ 1 km depth, ~~this distribution is consistent with a slightly steeper dip for the rupture than was indicated by the surface trenching, as suggested by the vertical tension fissure east of the scarp at the trench location (Figure 4c)~~implying that few if any of the aftershocks nucleated on the rupture plane. This is particularly the case for the largest aftershock (M_L 4.~~7~~6) – the uncertainty ellipse for this event occurs almost entirely below the depth of other aftershocks. A linear cluster of hypocentres is located directly below the south-eastern end of the rupture, parallel to the northwest-southeast oriented southern terminal structure at the surface (Figure 6b). Similarly, a loose cluster of hypocentres, including the M_L 4.~~7~~6 aftershock, underlies the east-west trending valley bounding the northern end of the reverse rupture imaged in the InSAR data (Figures 3 and 6a). Steep dips for terminal structures at the northern and southern ends of the reverse rupture are consistent with their orientation ~~sub-parallel~~at a low angle to the easterly maximum horizontal compression direction (S_{Hmax}) of the extant crustal stress field (cf. Rajabi et al., 2017b).

The central ~5 km of the September rupture, where the most significant surface displacement was observed, was modelled for Coulomb stress changes (e.g. Lin and Stein, 2004; Toda et al., 2005) (Figure 8, see Supplementary Information for detail of method and parametrisation). A dip of 50° to the east was assigned to the rupture for modelling purposes, consistent with the USGS focal mechanism for the event (Table 2), and with field data and modelling of the compressional reactivation of reverse faults (Sibson et al., 2012). The value is significantly different to the 30° dipping rupture plane exposed in the trench. We reconcile the two values in that the near surface may not be a good indicator of the fault dip at depth (cf. King et al., 2019, Figure 4). This is supported by the prominent tension fissure east of the scarp at the trench location, which indicates a steeper rupture dip at depth at least locally (Figure 4c). As the focal mechanism of the aftershocks are not known, results are presented with stresses resolved for both reverse and strike-slip (Figures 8a and 8b, respectively). In both cases, ~~Increases~~increases in Coloumb stress are modelled to have occurred down dip of the trailing edge of the rupture plane, and to a lesser degree in the footwall block at depth~~, down dip of the rupture plane, . and beyond the tips of the rupture to the north and south.~~ The majority of aftershock hypocentre locations show excellent correlation with the volume~~s~~ of increased Coulomb stress down-dip of the rupture plane. Hypocentres in the footwall block only occur in regions of increased Coulomb stress if it is resolved for optimal strike-slip faults (Figure 8b). A broad region of shallow stress relief above the trailing edge of the rupture corresponds with landscape depression imaged in the InSAR (cf. Figure 6b)~~Aftershock hypocentres plot predominantly in a volume down-dip from the rupture, where the Coulomb stress increased. The concentration of hypocentres at the northern end of the rupture occur along the line of intersection of the down-dip extension of the east-dipping rupture, and the east-west trending northern terminal structure, also within a volume of increased Coloumb stress. The greatest area of landscape depression imaged in the InSAR (Figure 6b), corresponding with Lake Noobijup, occurs above a region of stress relief beyond the trailing edge of the rupture~~.

As mentioned in section 3.2, simple forward modelling using a finite rectangular elastic dislocation model (Okada, 1985) (Figure S~~3~~4) suggests that a discrete surface rupture may not have been produced during the November strike-slip event. Based upon the InSAR surface deformation envelope (cf. Figure 6c), a rupture ~ 4 km~~--~~long and extending from 1.0 - 2.5 km~~--~~depth is preferred (Figures S3 and S4). If Coloumb stress changes resulting from the September rupture are resolved ~~onto the plane~~

~~of the November rupture (i.e., the dextral strike-slip receiver fault)~~for optimally oriented strike slip receiver faults ~~(Figure S3)~~, the plane of the November rupture is seen to be positively stressed over more than half of its area (Figure S4b). The case might then be made that the November event was triggered by static stress changes associated with the September event (cf. Mohammadi et al., 2019). However, additional factors may be involved as ~~The~~ the stress increase is only in the order of ~~approximately~~ 0.~~4~~1-0.~~5~~2 MPa in the region of nucleation of the November earthquake.

The November M_W 5.2 main shock is located within a diffuse elongated cluster of dependant aftershock hypocentres at ~3 - 4 km depth which trends parallel to the northeast-southwest orientation of the surface deformation front imaged in the InSAR data, offset to the southeast by 0.25-1.5 km (Figures 6c, d). Hypocentres predominantly occur at a greater depth than the preferred November event rupture plane (Figure S4b).~~The location of the hypocentre of the November M_W 5.2 main shock is consistent with the earthquake nucleating along the line of intersection between a sub-vertical northeast-southwest trending plane, and the September event rupture plane. This might potentially explain the poor double couple focal mechanism calculated for the event (Figure 2). Aftershock hypocentres occur between ~3 km and 4.3 km depth in a volume bound by the northeast-southwest trending, steeply dipping, rupture plane of the November M_W 5.2 event, and the 30° dipping extension of the September event rupture plane.~~

~~**3.5 Relationship between moment magnitude and surface rupture length amongst Australian cratonic earthquakes**~~

~~Clark *et al.* (2014b) provided scaling relationships between surface rupture length and moment magnitude for reverse faulting earthquakes occurring in Australian non-extended cratonic settings. Their relationships demonstrate that in this tectonic setting, earthquakes tend to produce longer earthquake ruptures than may be expected when compared to existing rupture scaling relationships~~ (e.g. Wells and Coppersmith, 1994; Leonard, 2014)~~. It is hypothesised that in these regions shallow crustal detachments~~ (Dentith et al., 2000; Drummond et al., 2000)~~ or, alternatively, large shallowly dipping thrust faults~~ (Goleby et al., 1989; Camacho et al., 1995; Korsch et al., 1998)~~ combined with high near-surface stresses~~ (Denham et al., 1980; Denham et al., 1987)~~ may favour the occurrence of earthquakes at shallow depths. This suggests that relatively narrow fault widths are available for seismogenic rupture, likely leading to large rupture length-to-width aspect ratios for small-magnitude earthquakes. Since the Clark *et al.* (2014b) relationship was presented, the Australian continent has experienced two further surface-rupturing earthquakes with the occurrence of the 2016 Petermann Ranges and 2018 Lake Muir events (see Table 1). Including these new data, the Clark *et al.* (2014b) scaling relationships are reviewed and updated.~~

~~With the availability of high-resolution InSAR observations, the extent of earthquake surface deformation can be more readily identified and mapped. Differences between the total "visible" surface rupture lengths (*VSRL*) from field mapping and "detectable" surface rupture lengths (*DSRL*) from InSAR observations are evident, with the latter observations being longer where these observations are available (Table 1). Consequently, regressions are undertaken between: 1) *VSRL* and M_W; and; 2) *DSRL* and M_W. The regression takes the following form:~~

~~$SRL = a + b \times M_W$ (1)~~

where *SRL* is the generic term given to either *VSRL* or *DSRL* and *a* and *b* are coefficients to be determined through regression (Table 3). When *DSRL* from InSAR observations is unavailable, the *DSRL* value is assumed to be equivalent to *VSRL*. It is recognised that this may yield an underestimate of the total rupture length, *DSRL*.

Figure 9a, b shows the least squares relationships relative to other rupture length scaling relationships used for non-extended cratonic regions. In general, the updated regressions suggest longer surface ruptures for a given earthquake magnitude, with likely convergence of *DSRL* with Clark *et al.* (2014b) near M_W 7.0.

Because of the likely biases imposed from assuming *DSRL* = *VSRL* for those ruptures that do not have available InSAR observations, a relationship between the ratio of *VSRL*:*DSRL* and *VSRL* is constructed using limited data from three earthquakes where independent *VSRL* and *DSRL* estimates exist (Figure 9c). It is assumed that earthquakes with decreasing magnitudes and increasing depth will be expressed at the Earth's surface with decreasing *VSRL* discoverability. The ratio of *VSRL* and *DSRL* could thus be used as a correction factor that could be applied to *VSRL* observations where independent estimates of *DSRL* do not exist. A literature search did not yield any additional data that could be added to the available dataset, particularly for reverse mechanism ruptures in non-extended cratonic regions. The proposed *VSRL* to *DSRL* correction factor, γ, can be calculated following:

$$\gamma = \min(\delta, 1.0) \quad (2a)$$

where:

$$\log_{10}\delta = 0.362 \times \log_{10} VSRL - 0.540 \quad (2b)$$

The corrected detectable surface rupture length (*DSRL*'), can thus be determined following:

$$DSRL' = VSRL / \gamma \quad (2c)$$

Supplementing the values of *DSRL*' for events where *DSRL* is not directly measured, revised rupture scaling relationships between *DSRL*' and M_W can be developed (Figure 9d; Table 3). These revised scaling relationships demonstrate longer rupture lengths for smaller magnitude earthquakes with lower standard deviation of the residuals (Table 3)

The authors recognise that these relationships are highly conjectural and are based on very limited data. Consequently, the authors invite additional researchers to augment these data to fully scrutinise the legitimacy of the relationships. Nevertheless, these fault scaling approaches may have future utility in the improving the characterisation of neotectonic fault scarps and their potential characteristic magnitudes. Should these approaches be refined, they may lead to a decrease in characteristic magnitudes on neotectonic fault scarps in non-extended cratonic regions, such as central and western Australia.

4 Discussion

4.1 Characteristics of the Lake Muir surface rupture sequence

The comparison of field observations, InSAR imagery, and aftershock earthquake catalogue has permitted exploration of the surface and sub-surface deformation field related to the Lake Muir earthquake sequence in unprecedented resolution. The September rupture, as mapped using traditional paleoseismological means, is revealed to be part of a more extensive deformed

region, involving both uplift and depression of broad areas proximal to the surface rupture. Furthermore, the spatial and temporal relationship between September and November $M_W > 5.0$ events reveals a dependency with ~~important~~ implications for how other earthquake swarms could be interpreted.

4.1.1 Reconciling UAV vertical displacement and InSAR LOS displacement measurements

InSAR measures displacement in the one-dimensional LOS of the SAR sensor. Three dimensional displacements of the ground surface are therefore mapped into a one-dimensional geometry. If InSAR data from different viewing geometries (e.g., ascending and descending orbital passes of the SAR satellite) is available, then vertical and horizontal components of displacement can be resolved (Fuhrmann and Garthwaite, 2019). Unfortunately, this is not the case for the Lake Muir earthquake, where only descending-pass Sentinel-1 SAR data is available. Displacement measurements derived from InSAR analysis of this data must therefore be interpreted in the LOS, and horizontal and vertical signals cannot be unambiguously separated.

This is problematic when attempting to reconcile the single-geometry InSAR LOS data with the absolute elevation changes captured by the UAV (e.g., Figures 7b and c). However, the descending orbit of the Sentinel-1 data used here has a ground azimuth of 196°, and the SAR sensor looks perpendicularly to the right of this orbit direction (i.e., 286°). The LOS of the SAR sensor is very close to the P-axis of the focal mechanism of the September earthquake (288°). If the earthquake resulted in almost pure thrust motion along the line of the P-axis, as suggested by the focal mechanism (±10°), the single InSAR viewing geometry should be sensitive to the full surface deformation field. The geometry problem is thus reduced approximately to a vertical plane containing the LOS vector and the slip vector.

We use the above understanding to empirically derive a multiplicative factor of 2.75, which produces a generally good match between the forms of both scarp-perpendicular and scarp-parallel InSAR LOS and UAV vertical displacement profiles (Figure 7b and 7c, dashed black lines). This factor is consistent with our assumption of a 50° fault dip, given the ~41° side look angle of the Sentinel-1 sensor at our field location. It is useful to apply this factor to 'correct' the InSAR profile to enable a comparison of the UAV and InSAR data. There are two locations on the profiles where the match is poor. Firstly, the corrected InSAR LOS profile underestimates the vertical displacement compared to the UAV profile from 2750 - 3250 m along the profile in Figure 7b. This region corresponds to a 50 m left step in the scarp, and a 25° change in strike direction (Figure 7a). The assumption that the InSAR LOS direction is parallel to the slip vector breaks down here. Secondly, the InSAR profile has not resolved the narrow footwall depression that is apparent in the UAV DoD (Figure 7c). Much of the region occupied by the proximal footwall was masked as the result of lack of coherence of the InSAR signal.

4.1.2 Character of surface deformation~~: subsidence in the hanging wall relating to the September event~~

The average magnitude of vertical surface deformation along the discrete surface rupture trace, as indicated by the UAV DoD data, and locally validated by the corrected InSAR LOS displacement profile (Figure 7b), is 0.46±0.11 m over the central ~~2~~ 2 km of the rupture. The corrected InSAR LOS displacement profile suggests that displacement tails off smoothly to the north

from this central plateau (Figure 7b). To the south of the central plateau, there is a step to higher vertical displacement where the scarp changes orientation (2750 - ~~3000~~ 3250 m along the profile), and then a fall to the southern extremity. The exact shape of the southern tail, defined by point measurements and 2-D UAV profiles, is largely obscured beneath pine forest. ~~A~~ The scarp-perpendicular profile through the UAV and corrected InSAR data (Figure 7c) shows that very little subsidence has occurred in the footwall of the fault (i.e., it is absent in the corrected InSAR data, and seen as a very narrow trough in the UAV DoD), and that the hanging wall uplift relating to the rupture tails off over the ~ 1.0 – 1.5 km to the east of the scarp, falling to a broad area of subsidence up to ~ 0.3 m below the foot wall level. The rupture is bound to the north and south by ~~steeply dipping~~ highly orthogonal structures that are likely steeply dipping, and in the case of the southern structure ~~to have~~ accommodated dominantly tear or strike-slip displacement during the September event. These structures bracket the broad region of ground subsidence that occurred to the east of the uplifted hanging wall region (e.g., Figure 6b). ~~Consistent with the fault dip measured in the trench (Figure 5c), and deduced from the InSAR correction factor (Figure 7b), elastic~~ Elastic dislocation modelling indicates that for shallow to moderate reverse fault dips ~~of less than ~ 35–40°~~, subsidence should occur above the buried trailing edge of the fault rupture (Okada, 1985; King et al., 1988; Ellis and Densmore, 2006). ~~A rupture width of <2 km is implied, as compared to the ~ 5 km subsurface rupture length (not including the southeast segment, Figure 7a).~~ The area of footwall subsidence observed, an area ~1.5 times that of the uplifted region, is surprisingly large compared to what might be expected given our preferred fault dip of 50°. Further, the region of greatest subsidence at the northern end of the rupture, coincident with Lake Noobijup, is not predicted by simple modelling. While ~~R~~rupture complexity ~~is implied~~ relating to an interaction between the rupture plane and the northern bounding structure could explain this result, a plausible alternative is settlement relating to the sedimentary materials filling the Lake Noobijup Basin.

~~The rupture is bound to the north and south by steeply dipping highly orthogonal structures that are likely to have accommodated dominantly tear or strike-slip displacement during the September event. These structures bracket the broad region of ground subsidence that occurred to the east of the uplifted hanging wall region (e.g., Figure 6b); an area ~ 1.5 times that of the uplifted region. The magnitude of the InSAR LOS displacement/subsidence is greatest beneath Lake Noobijup (Figure 6b).~~ As field observations failed to find any obvious surface structural development or cracking in this region, the presence of ~~a~~ subsidence ~~trough~~ may not have been ~~discovered~~ recognised if not for the InSAR data.

In the generally low-relief landscapes typical of intraplate regions, such depressions may have significant impacts on surface and subsurface hydrology. A potential analogue is the 'back-scarp zone' mapped in the hanging wall of the 1968 Meckering surface rupture (Gordon and Lewis, 1980) (see Figure 1 for location; Table 1). The back-scarp zone is an arcuate convex-to-the-east band of normal faulting and slumping ~ 3 km wide which joined the tips of the concave-to-the-east reverse fault rupture. A single levelling line across the back-scarp zone identified a 0.3 m depression of the land surface, contrasting to the ~ 1.5 – 2.0 m of throw across the scarp ~ 10 km to the west (Gordon and Lewis, 1980). Changes in hydraulic gradient raised the flood level at Meckering town site by an estimated 12 cm, forcing the relocation of the town to higher ground. In the case of the September Lake Muir event, the hydrology of the important wetland habitat of Lake Noobijup (e.g. Smith, 2010) may be permanently affected by a combination of subsidence, and re-plumbing of the local fractured rock hydrology. ~~There has~~

~~been no systematic search to determine if hanging wall subsidence is a characteristic of reverse faults in Phanerozoic eastern Australia (cf. Clark et al., 2012). However, the position of the Wakool and Gunbower fans on the distal hanging wall of the Cadell Fault Block (e.g. Clark et al., 2015) is worthy of investigation in this respect (see Figure 1, location e).~~

4.1.3 Co-location of thrust and strike-slip ~~events~~surface deformation envelopes

In statistical seismology the uncertainties attached to the calculated locations of small to moderate sized events forming part of a sequence typically precludes analysis of the detailed temporal, spatial and/or structural relationships between failure surfaces, even with dense instrument networks and sophisticated techniques such as double difference or joint hypocentre relocation (Waldhauser and Ellsworth, 2000). For the Lake Muir sequence, the InSAR data provides compelling evidence for co-location of the surface deformation envelopes relating to the two largest events (Figure 6), and the quadrupole surface deformation pattern for the November event allows the geometry of the source fault to be confidently interpreted, which would not have been the case given only the focal mechanism. Our temporary seismograph network has allowed us to achieve hypocentral location uncertainties of better than 300 m (see Section 3.4) for all bar the three largest events (see Section 3.4; Table 2). ~~Hence, t~~The combination of InSAR, ~~the~~ aftershock data, ~~InSAR,~~ field observations and regional aeromagnetic data (cf. Chakravartula and Street, 2000; Milligan and Nakamura, 2015) ~~(cf. Milligan and Nakamura, 2015)~~ therefore provides an ~~unprecedented~~ opportunity, unprecedented in Australia, to examine the relationships between the two $M_W > 5.0$ events, ~~and thereby gain a better understanding of the distribution of~~ the associated smaller-magnitude seismicity, and host geological structures.

The inferred 50° easterly dip of the rupture plane associated with the September main shock is steeper than might be expected presuming fault formation or reactivation at optimal orientations with respect to a horizontal σ1 in a simple Andersonian compressional stress regime (Anderson, 1905; Anderson, 1951). However, the value is not unreasonable (cf. Sibson et al., 2012) as it is likely that the very shallow Lake Muir Rupture reactivated pre-existing structures evident as north to northeast valley trends in the LiDAR (Figure 3) overlying minor lineament trends in the magnetic data (Figure 2). Aftershock hypocentre locations don't define the rupture plains for the Lake Muir sequence, whereas this is the expectation (e.g. Henry and Das, 2001; Yabe and Ide, 2018) and commonly the case where explored (Bowman et al., 1990; Gupta et al., 1998; King et al., 2018).

~~Intersections may have also played a role in nucleating subsequent events within the sequence.~~ Aftershock hypocentres predominantly occur deeper than the trailing edge of the rupture, and within a volume of positive Coulomb stress change down-dip of the rupture plane (Figure 8). The greatest density of aftershocks, including the largest aftershock (M_L 4.6), occurs where this volume of positive Coulomb stress change underlies the ~~paleo channel~~ linear valley bounding the northern end of the rupture, potentially where the positive stress volume intersects the steep structures imaged in the magnetics underlying the ~~channel~~valley. Similarly, aftershocks underlying the southern terminal structure of the rupture occur where Coulomb stress increased, but well below the expected extent of the rupture plane.

~~Intersections between pre-existing basement structures may well have played an important role in nucleating the larger events within the sequence~~ (cf. Talwani, 1988; Dentith and Featherstone, 2003; Talwani, 2014)~~. The September M_W 5.3 event appears~~

~~to have nucleated at the intersection between a sub vertical (or steeply south dipping) east trending fault and the ~30° east dipping main rupture plane. The rupture propagated upward, rupturing the ground surface to produce the observed scarp, and towards the south, ultimately terminating against a sub vertical northwest trending structure. Aftershock hypocentres are located ubiquitously deeper than the trailing edge of the rupture, and below the down dip extension of the rupture plane. The greatest density of aftershocks, including the largest aftershock (M_L 4.7), occurs at the northern end of the rupture, proximal to the northern bounding fault. This aftershock concentration is spatially coincident with the region of greatest land surface subsidence (Figure 6b). In general, the volume in which aftershocks are located corresponds to a volume of positive Coulomb stress change resulting from the main shock (Figure 8).~~

As best as can be determined given the uncertainty in modelling the depth extent and dimensions of the September and November rupture planes (Figures 8, S3 and S4), they appear to ~~have be~~en ~~en~~ spatially distinct, despite coincidence of the surface deformation envelopes (Figure 6). Further, static stress modelling suggests that while over half of the November M_W 5.2 rupture plane was promoted towards strike-slip failure by the September M_W 5.3 event ~~(Figure S4)~~, the nucleation point for the November rupture does not appear to ~~have occurred~~be in the most highly stressed region proximal to the trailing edge of the September rupture (Figure S4) (for other examples, see: Steacy et al., 2013; Mohammadi et al., 2019). The September and November rupture planes are certainly near enough for dynamic stress triggering to be considered as a mechanism for the November failure (cf. Gomberg and Johnson, 2005). However, the memory of fault gouge softening resulting from dynamic strains, termed 'slow dynamics' (Johnson and Jia, 2005), typically only extends over several hours or days after the wave energy has disappeared. Prolonged triggered sequences require a multistage process such as continued triggering through a secondary cascade (Felzer et al., 2003; Johnson and Jia, 2005; Brodsky and Elst, 2014; Meier et al., 2014; Mohammadi et al., 2019). In this ~~respect~~context the M_L 4.~~7~~6 aftershock might be important. Permeability enhancement leading to drainage or pore pressure redistribution on faults (Hill et al., 1993; Townend and Zoback, 2000; Brodsky et al., 2003) is an alternative possibility that might have a long~~er~~ time constant ~~more~~ appropriate to the Lake Muir sequence. Redistribution of pore fluid pressure might also explain the location of ~~some~~the minority of aftershock hypocentres in regions modelled to have experienced static coulomb stress reductions as a result of the September main shock (e.g. Figure 8). This could be the topic for a future, more focussed study.

A further contributing factor to the spatial mismatch between November hypocentre and the region of highest positive coulomb stress change might be found in an examination of the character of the regional stress field. The modelled trajectory of the maximum horizontal compressive stress (S_{Hmax}) in the southwest of Western Australia is roughly east-west (88±18°, Rajabi et al., 2017b). This orientation is consistent with the principal compressive axis (P-axis) orientations for both Lake Muir main shocks (Figure 2), allowing for the ~~the~~ poorly quantified uncertainties in moment tensor solutions (cf. Valentine and Trampert, 2012). The similarity in P-axis trends implies that the stress drop associated with the September M_W 5.3 event was small compared to the extant differential stress ($\sigma1$-$\sigma3$, e.g. Hardebeck and Okada, 2018), and that the change in stress regime between events relates to transposition of the intermediate and minimum principal stress axes. Rajabi et al. (2017a) model the stress regime in the Lake Muir region to favour thrust faulting close to the surface (~1 km), and to favour a progressively

greater strike-slip component to failure with depth. The transposition of principal stress axes between ruptures, and the apparent location of the nucleation point of the November strike-slip event near the base of the rupture plane, may relate to this changing depth-character of the stress field.

~~As best as can be determined given the uncertainty in the location estimate (i.e., several kilometres~~±1.05 km, Table 2~~), the November M_W 5.2 earthquake nucleated near the centre of the volume of positive Coulomb stress change relating to the September event, potentially along the line of intersection between the down dip extension of the September rupture and the November rupture plane. A comparison of InSAR images (Figures 6a & c) indicates a spatial coincidence of surface deformation envelopes, with the northeast striking rupture plane relating to the November event crossing the September rupture near the centre of both ruptures. The quadrupole deformation pattern for the November event suggests an almost pure strike slip mechanism, as compared to the oblique compressive focal mechanism for the event (Figure 2, Table 2). A stress condition favourable for strike slip failure may have arisen as a result of local stress rotation following the September event. The phase interferogram for the November event also shows a linear fringe boundary coinciding with the southern part of the September rupture (Figure 6c), consistent with the anecdotal evidence for minor reactivation of the rupture. In terms of a simple conceptual block model, the southern side of the November dextral strike slip rupture moved to the southwest, and in doing so may have caused a partial reverse reactivation of the September rupture plane. Simultaneous failure along both trends, perhaps originating as a stress concentration at the intersection of the trends (e.g. Talwani, 1988), may explain the 31% double couple for the November event moment tensor. Aftershocks following the November event were confined largely to the volume beneath the down dip extension of the September rupture plain, and southeast of the November rupture plain.~~

4.2 Stress triggering and moderate to large magnitude non-extended SCR earthquake sequences

Whereas there is an emerging body of literature concerning human-induced/triggered earthquake sequences in SCRs (e.g. Keranen et al., 2013; Skoumal et al., 2015; Peterie et al., 2018), relatively little has been published on natural earthquake sequences (e.g. Chiu et al., 1984; Špičák, 2000; Allen et al., 2006). The latter appear to be an important component of intraplate seismicity, especially in non-extended SCR crust (e.g. Lopes et al., 2010; Clark et al., 2014a; Dent, 2016). Evidence for the spatial coincidence of ~~similar~~ similar-magnitude ~~moderate~~ moderate- to large-sized ~~SCR~~ earthquakes as part of these sequences, often with mixed focal mechanisms such as the Lake Muir sequence, is ~~with different failure mechanisms is~~ rare ~~in Australia~~but not unprecedented~~, typically as the result of large uncertainties in epicentral location estimates~~. For example, the 1988 M_W 6.76 Tennant Creek earthquake sequence (Figure1; Table 1) began with three surface rupturing earthquakes of similar reverse mechanism within a 12-hour period (Choy and Bowman, 1990; Bowman, 1992; Crone et al., 1997). Static stress triggering can account for the progression of events within the sequence (Mohammadi et al., 2019), with the rupture planes for the three largest events occurring well within a fault length of each other (cf. Caskey and Wesnousky, 1997). The sequence continues to this day, producing occasional events sufficiently large to deform the Earth's~~2~~ surface (Table 1). Of seven focal mechanisms constructed for the sequence, ~~5~~five are reverse faulting events with a similar P-axis orientation, and two are normal faulting events with tension axes coinciding with the compression axes of the reverse events (Clark and

Leonard, 2003). The normal faulting events may relate to visco-elastic relaxation, or adjustment (cf. DeVries et al., 2016). Similar normal faulting events were recorded in the aftershock sequence relating to the 1993 Killari-Latur earthquake (Gupta et al., 1998).

In the Eastern Canadian Precambrian Shield, the 1989 M_W 6.5 Ungava earthquake sequence involved a reverse mechanism surface rupture followed after 0.9 seconds by a larger strike-slip rupture approximately 5.2 km away (Adams et al., 1991; Bent, 1994). The focal mechanisms for the events share a common P-axis orientation (Bent, 1994), similar to the Lake Muir mainshocks. Pre-existing bedrock faults were assumed to have hosted the ruptures, but the spatial relationship between rupture planes was not determined, ostensibly because a surface rupture relating to the larger strike-slip event was not observed. One potential explanation proposed by Bent (1994) was that the focus of the strike-slip event was deeper, and so the event did not result in surface rupture.

A comparable sequence is documented from central Australia. ~~In central Australia, t~~The reverse mechanism surface-rupturing 2012 M_W 5.4 Ernabella earthquake (Clark et al., 2014b; Figure 1) was followed ~~fifteen~~15 months later by the strike-slip 2013 M_W 5.4 Mulga Park earthquake, which caused extensive surface cracking but no observed surface rupture (Clark and McPherson, 2013). The surface expressions relating to these events indicate that they were likely proximal (≤10 km separation) rather than co-located (Clark and McPherson, 2013). The first event occurred in the hanging wall of the crustal-scale Woodroffe Thrust Fault (cf. Camacho et al., 1995; Camacho and McDougall, 2000; Lin et al., 2005), and the second event in the foot wall, potentially at a depth of ~10 km (Kevin McCue pers. comm., 2013). Again, both events share a common P-axis orientation (Clark and McPherson, 2013). In common with the Lake Muir sequence, the moment tensor for the strike-slip event had a low percentage double couple, indicating rupture complexity.

The above examples comprise a class of seismicity in non-extended Precambrian SCR crust characterised by multiple moderate to large mainshocks sharing common compression axes. The similarity in P-axis trends of the focal mechanisms implies that the stress drop associated with each event was small compared to the extant differential stress (σ1-σ3, e.g. Hardebeck and Okada, 2018), despite the sometimes large magnitude of the main shocks. ~~(2000)~~The time interval between the largest events in a sequence varies greatly, as does the separation between rupture planes. Mohammadi (2019) explore these relationships in the context of the Tennant Creek earthquake sequence, and conclude that the time between two dependant events is proportional to the magnitude of the static Coulomb stress increase on the receiver fault plane (not necessarily at the hypocentral location), which in turn relates to the trigger-rupture magnitude and distance from the receiver fault. Multiple triggering mechanisms are required to explain time lags spanning several orders of magnitude (cf. Townend and Zoback, 2000; Gomberg and Johnson, 2005; Johnson and Jia, 2005; Meier et al., 2014).

The September 2000 to June 2002 Burakin earthquake swarm, located ~ 20 km north of the 1979 Cadoux surface rupture (Figure 1), ~~which involved approximately 18,000 closely co-located earthquakes (Leonard, 2002)~~ is ~~an perhaps an exception~~example of a different class of seismicity to the sequences discussed above~~, and may be considered to be broadly analogous to the Lake Muir sequence~~. Focal mechanisms were generated for the largest six ~~events~~ of the approximately 18,000-event swarm (Leonard, 2002)~~Burakin swarm~~, spanning a magnitude range from M_W 4.1 – 4.6 (Leonard et al., 2002; Allen et

al., 2006). ~~-~~These indicate a mixture of thrust and strike-slip ruptures, and one pure normal faulting rupture, with diverse compression axis orientations and all within a ~5 km radius. Preliminary joint hypocentre relocation suggests that these events, and several thousand smaller events, may have originated from as few as 3-4 source areas (Mark Leonard pers. comm., 2018). Aeromagnetic data (Milligan and Nakamura, 2015) indicate that the Burakin swarm area is characterized by a high lineament density, with major trends to the east, northeast and north. Static and dynamic stress interactions, or ~~Block-~~block motion following moderate events, may have stressed intersections between these trends, triggering further events with an eclectic mix of mechanisms with diverse P-axis orientations (cf. Talwani, 1988; Dentith and Featherstone, 2003; Talwani, 2014). This behavior, in contrast to the sequences that include larger events with focal mechanisms showing consistent P-axes (e.g. Lake Muir), may occur preferentially in regions of extremely heterogeneous geological structure, where high stress concentration around numerous cracks and faults within the structured volume results in failure on many local fractures at low stress (Mogi, 1963), thus reducing the probability of failure on a single large fracture.

~~In central Australia, the reverse mechanism of the 2012 M_W 5.4 Ernabella earthquake (Clark et al., 2014b; Figure 1) was followed fifteen months later by the strike-slip 2013 M_W 5.4 Mulga Park earthquake, which caused extensive surface cracking but no observed surface rupture (Clark and McPherson, 2013). The surface expressions relating to these events indicate that they were likely proximal (≤10 km separation) rather than co-located (Clark and McPherson, 2013). The first event occurred in the hanging-wall of the crustal-scale Woodroffe Thrust Fault~~ (cf. Camacho et al., 1995; Camacho and McDougall, 2000; Lin et al., 2005)~~, and the second event in the foot-wall, potentially at a depth of ~10 km (Kevin McCue pers. comm., 2013). Similar to the November Lake Muir event (Figure 2, Table 2), the moment tensor for the Mulga Park strike-slip event had a low-percentage double couple, indicating rupture complexity.~~

~~While it is plausible could be considered that dynamic and/or static stress changes from the 2012 Ernabella event triggered the 2013 Mulga Park event, it is also possible that in this case the components of the stress field conducive to thrust and strike-slip failure proximal to the highly structured Woodroffe Thrust crustal 'weakness' (Camacho and McDougall, 2000), were resolved onto spatially discrete structures.~~

4.~~2~~ 3 One-off ruptures from moderate to large magnitude earthquakes in ~~the cratonic regions of Australian~~ non-extended SCR

~~Conceptually, for the purposes of probabilistic seismic hazard assessment, a *fault source* is a seismogenic fault that has produced earthquakes in the past, and can be expected to continue doing so (Musson, 2012).~~ The Lake Muir sequence resulted in the production of a surface rupture, and more subtle landscape change (i.e., depression of Lake Noobijup), that might be expected to be persistent in the landscape for thousands of years (cf. Quigley et al., 2010; Clark, 2010; Leonard and Clark, 2011). Questions of whether Lake Noobijup may have a seismogenic origin aside, there is no landscape evidence for Late Pleistocene to Holocene surface rupture on the structures that failed during the 2018 sequence (Section 1.3). Similarly, no evidence was found for more than the 2018 displacement across *in situ* weathered materials in the hand trench (Figure 5). Further, no sharp landscape dislocations are evident that might relate to recent faulting of Paleogene paleo-channel sediments

(Section 1.2). If moderate to large earthquakes are assumed to recur on the faults that comprise the 2018 Lake Muir rupture, the long-term average uplift rate (i.e., the vertical component of the slip rate) is limited by the very low regional bedrock erosion rates of 1-5 m/Myr (e.g. Chappell, 2006).

~~Excluding the November M_W 5.2 event, for which a unique surface rupture could not be mapped in the field, t~~The September M_W 5.3 Lake Muir earthquake was the ninth event documented to have produced surface rupture in the Australian SCR in historical times (Figure 1, Table 1). These ruptures are located exclusively in the Precambrian SCR crust of central and western Australia (Figure 1), and none could have been identified and mapped using topographic signature prior to the historical event (see references in Table 1). For example, Crone et al. (1997) excavated trenches across the 1986 Marryat Creek and 1988 Tennant Creek ruptures and found that while each rupture in part exploited pre-existing bedrock faults, there was no unequivocal geomorphic, stratigraphic or structural evidence to suggest a penultimate event in the preceding 50-~~100~~ 100 kyr or more. A similar conclusion was made on the basis of trenching investigations of the 1968 Meckering surface rupture (see Clark and Edwards, 2018, and references therein).

Paleoseismological investigations of several faults in the same Precambrian SCR tectonic setting provide evidence for limited recurrence of large earthquakes, with up to four events documented on an individual fault within the last *ca.* 100 kyr (Crone et al., 2003; Clark et al., 2008; Estrada, 2009). These scarps - Roopena, Hyden, Lort River and Dumbleyung (see Figure 1 for locations) - all overlie simple through-going faults imaged in aeromagnetic data (Milligan and Nakamura, 2015). The two-to-five Quaternary events documented on the Hyden (Clark et al., 2008) and Lort River (Estrada, 2009) scarps are all that are evident across Late Neogene duricrust. While shallow trenches across the 2-5 m high Roopena scarp exposed Precambrian bedrock on both sides of the fault (Crone et al., 2003), nearby scarps are associated with an extended Neogene to Recent history of movement (Miles, 1952; McCormack, 2006; Weatherman, 2006). For example, the Randell and Poynton Faults, ~~on the northeastern Eyre Peninsula (South Australia)~~ immediately to the south of the Roopena scarp, are associated with 30-70 m of Pliocene and younger vertical displacement (McCormack, 2006). Scarps developed in the *ca.* 15 Ma surface of the Nullarbor Plain (Figure 1), which overlies Neoproterozoic mobile belt basement, are associated with up to 15-30 m of vertical surface displacement (Hillis et al., 2008; Clark et al., 2012), implying the recurrence a dozen or so neotectonic events per fault at most. In general, scarps developed within Archean and Paleoproterozoic crust tend to be more modest in height, less well connected (i.e., spatially isolated), and more complex in plan than scarps in Mesoproterozoic and Neoproterozoic crust (Clark et al., 2012). ~~The remarkable sequence of three 'one-off' surface breaking earthquakes in 1968, 1970 and 1979~~ (Meckering, Calingiri and Cadoux — Gordon and Lewis, 1980; Lewis et al., 1981) ~~raises interesting questions about the potential for multiple modes of upper crustal failure when stress thresholds are exceeded. The structurally 'complex' Meckering, Calingiri and Cadoux scarps (Figure 1) are 70–100 km apart; too distant for static stress changes to have promoted rupture (cf. Caskey and Wesnousky, 1997). Furthermore, the ruptures were sufficiently temporally separated that dynamic stress changes are unlikely to have promoted rupture (e.g. Belardinelli et al., 2003). The observations are consistent with the postulate that blocks of upper crust on the scale of ~10^4 square kilometres can unload in the space of a decade (Clark et al., 2012). In the case of southwest Western Australia, this process may be facilitated by a mid- to upper crustal architecture characterised by fundamental sub-~~

~~horizontal structural discontinuities (most notably at ~10 km and ~25 km depth)~~ (Everingham, 1965; Drummond and Mohamed, 1986; Goleby et al., 1993; Dentith et al., 2000)~~ that are compartmentalised by major moderately dipping fault systems, forming "super terranes" as envisaged by Wilde et al. (1996). Perhaps the presence of through-going faults perpendicular to the crustal stress field may mean the difference between an unloading scenario involving strain localization in successive events on a single fault (e.g., Dumbleyung), or on several proximal structures (e.g., Meckering). As mentioned in the previous section, intersection of structural trends, and rheological changes at the boundaries of mafic dykes have been proposed as stress concentrators, potentially promoting 'weakness'~~ (Everingham and Gregson, 1996; Dentith and Featherstone, 2003)~~.~~ A pattern is emerging in Australian Precambrian non-extended SCR where 'one-off' ruptures, as evidenced by the historic surface-breaking earthquakes, ~~(Figure 1, Table 1)~~ are filling the spaces between mapped multi-event neotectonic scarps (Figure 1~~, Table 1~~). ~~With few examples, it is not possible to draw conclusions with any certainty~~.

Elsewhere in Precambrian non-extended SCRs the record is consistent with the Australian examples, but more fragmentary. Seeber *et al.* (1993; 1996) excavated two trenches across the 1993 Killari earthquake rupture in Peninsular India. These authors found no evidence for a pre-exiting fault zone, but observe that the rupture followed foliation in Cretaceous basalt country rocks, which were estimated to be several hundred metres thick. A third trench revealed a section of the rupture that exploited a pre-existing fault zone in the basalts, which coincided with a lineament evident in satellite imagery (Rajendran et al., 1996). However, ~~(1996)~~ no evidence was found in the topography at all three trench sites, or along the lineament, for a Late Pleistocene to Holocene prior rupture. ~~Similarly, t~~The Ungava rupture in the Canadian Precambrian shield was found to be controlled by compositional layering and foliation within ~~a steeply dipping sequence of paragneiss and granite~~crystalline rocks containing concordant ductile high-strain zones (Adams et al., 1992), similar to the 2016 Petermann Ranges rupture in Australia (King et al., 2018). Although the landscape record was short, being in a recently de-glaciated region, the authors found no evidence to suggest that the Ungava rupture occurred on a fault that has hosted prior reactivation in the Phanerozoic.

The preponderance of 'one-off' and limited-recurrence faults suggests caution in applying a traditional elastic strain accumulation model to non-extended Precambrian SCR crust (cf. Braun et al., 2009; Clark, 2010). Indeed, over the last few decades, permanent and campaign GPS studies have failed to detect a tectonic deformation signal from which a strain budget could be calculated across all classes of SCR crust; in Australia (e.g. Tregonning, 2003), the central and eastern United States (Calais et al., 2005), eastern Canada (Mazzotti and Adams, 2005), and central Africa (Gardonio et al., 2018). Similar studies have used these observations, amongst others (e.g. Calais et al., 2005), to propose that one-off events and clusters of large events either deplete long-lived pools of 'fossil' lithospheric stress (Liu and Stein, 2016; Calais et al., 2016) and/or that there is an orders of magnitude difference in the timescales of elastic strain accumulation and seismogenic strain release (e.g. Clark et al., 2015; Craig et al., 2016). Hence, the underpinning assumption that a 'long-term slip rate' is a meaningful concept in all classes of intraplate crust, as per the prevailing plate margin paradigm, remains to be fully tested. Preliminary indications are that the concept may be useful for extended SCR crust worldwide (Sandiford, 2003b; Quigley et al., 2006; Cox et al., 2013; Copley et al., 2014; Rastogi et al., 2014), and for the non-extended Phanerozoic SCR crust of eastern Australia (Figure 1), where faults with up to a few hundreds of metres of neotectonic slip occur (cf. Sandiford, 2003a; Clark et al., 2015; Clark et

al., 2017). However, faults studied thus far in the Phanerozoic SCR crust of the eastern United States (Crone and Luza, 1990; Crone and Machette, 1995; Zellman and Ostenaa, 2016; Hornsby et al., 2019), and Mongolia (Amarjargal et al., 2013) seem more akin to the limited recurrence faults in Precambrian non-extended SCR, cautioning against a blanket application.

Conceptually, for the purposes of probabilistic seismic hazard assessment, a *fault source* is a seismogenic fault that has produced earthquakes in the past, and can be expected to continue doing so (Musson, 2012). Our results therefore urge caution when building 'active' faults into seismic hazard assessments in SCRs. Furthermore, in the absence of meaningful recurrence of large events, building relations for fault displacement hazard using rupture traces from Precambrian Australia is also fraught (cf. Boncio et al., 2018; Livio et al., 2019). Another implication for seismic hazard assessment involving the 'Lake-Muir' class of seismicity discussed herein, perhaps most ~~pertinently~~ significantly demonstrated by the 1989 Ungava rupture (Adams et al., 1991; Bent, 1994), is that the paleoseismic and neotectonics records of large earthquakes may be missing significant seismic moment in that not all main shocks within a sequence produce recognisable surface deformation.

~~This preponderance of 'one off' events suggests caution in applying a traditional elastic strain accumulation model to Precambrian SCR crust (cf. Braun et al., 2009; Clark, 2010). Indeed, over the last few decades, permanent and campaign GPS studies have failed to detect a tectonic deformation signal from which a strain budget could be calculated across all of Australia (e.g. Tregonning, 2003). Similar studies have used these observations, amongst others (e.g. Calais et al., 2005), to propose that one off events and clusters of large events either deplete long lived pools of 'fossil' lithospheric stress (Liu and Stein, 2016; Calais et al., 2016) and/or that there is an orders of magnitude difference in the timescales of elastic strain accumulation and seismogenic strain release (e.g. Clark et al., 2015; Craig et al., 2016). By virtue of the scarcity of data with which to validate such a model, the underpinning assumption that a 'long term slip rate' is a meaningful concept in an intraplate setting, as per the prevailing plate margin paradigm, remains to be fully tested. Indications are that the concept may be useful in the Phanerozoic stable continental region (SCR) crust of eastern Australia (Figure 1), where faults with up to a few hundreds of metres of neotectonic slip occur (cf. Clark et al., 2015; Clark et al., 2017). However, it is not so certain whether assigning a long term slip rate is meaningful for Precambrian SCR crust (e.g. Calais et al., 2016). In the absence of meaningful recurrence of large events, building relations for fault displacement hazard using rupture traces from cratonic Australia is fraught (cf. Boncio et al., 2018; Livio et al., 2019).~~

~~As was the case with the 2016 Petermann Ranges earthquake rupture (King et al., 2018; Polcari et al., 2018; Wang et al., 2019), the Lake Muir September event surface rupture was longer than might have been expected from scaling relationships between magnitude and surface rupture length (e.g. Wells and Coppersmith, 1994; Clark et al., 2014b; Leonard, 2014). New relationships developed as part of this study (Figure 9) allow for the distinction between "visible" surface rupture lengths (*VSRL*) from field mapping, and "detectable" surface rupture lengths (*DSRL*) from increasingly more readily available InSAR data that more closely define the complete rupture extent. Relative to the scaling relationships introduced by Clark et al. (Clark et al., 2014b; equivalent to the VSRL relationships presented here), the updated relationships include more data and yield~~

lower uncertainties, particularly when the *DSRL* is used. In general, the *DSRL* scaling relationships will yield longer ruptures for a given event magnitude, converging with the Clark et al. (2014b) scaling relationships near M_W 7.0. Users should exercise caution extending these relationships to lower magnitudes where the intersection of the rupture plane with the surface becomes less likely. Nevertheless, the relatively large rupture lengths observed for moderate to large earthquakes in non-extended Australian cratonic crust challenges notions that SCR earthquakes should yield higher stress drops (e.g., Allmann and Shearer, 2009), with smaller rupture areas (e.g., Brune, 1970). Conservation of high stress drop for SCR events, commensurate with Allmann and Shearer (2009), would require narrow down-dip rupture widths that yield large aspect ratios. The surface displacement field revealed in the InSAR suggests that the rupture width is < 2.0 km, suggesting non-uniform scaling between rupture length and width. Systematic analysis of stress drop for recent moderate to large ($M_W \geq 5.0$) Australian earthquakes should be undertaken to test the nature of stress drop relative to surface rupture to provide further constraint on the expected rupture dimensions of SCR earthquakes in Australia.

4.34 Insight into mechanisms for strain localisation in Stable Continental Region (SCR) crust

The preponderance of 'one-off' and limited recurrence faults suggests caution in applying a traditional elastic strain accumulation model to non-extended Precambrian SCR crust (cf. Braun et al., 2009; Clark, 2010). Indeed, over the last few decades, permanent and campaign GPS studies have failed to detect a tectonic deformation signal from which a strain budget could be calculated across all of Australia (e.g. Tregonning, 2003). Similar studies have used these observations, amongst others (e.g. Calais et al., 2005), to propose that one-off events and clusters of large events either deplete long-lived pools of 'fossil' lithospheric stress (Liu and Stein, 2016; Calais et al., 2016) and/or that there is an orders-of-magnitude difference in the timescales of elastic strain accumulation and seismogenic strain release (e.g. Clark et al., 2015; Craig et al., 2016). By virtue of the scarcity of data with which to validate such a model, the underpinning assumption that a 'long-term slip rate' is a meaningful concept in an intraplate setting, as per the prevailing plate margin paradigm, remains to be fully tested. Indications are that the concept may be useful in the Phanerozoic stable continental region (SCR) crust of eastern Australia (Figure 1), where faults with up to a few hundreds of metres of neotectonic slip occur (cf. Clark et al., 2015; Clark et al., 2017). However, it is not so certain whether assigning a long-term slip rate is meaningful for Precambrian SCR crust (e.g. Calais et al., 2016). In the absence of meaningful recurrence of large events, building relations for fault displacement hazard using rupture traces from cratonic Australia is fraught (cf. Boncio et al., 2018; Livio et al., 2019).

The September Lake Muir earthquake sequence occurred within rocks and on structures related to the Proterozoic Albany Fraser Orogen, immediately south of the deformed southern margin of the Archaean Yilgarn Craton (Fitzsimons and Buchan, 2005; Spaggiari et al., 2009), and sits astride a significant Bouguer gravity anomaly gradient parallel to the boundary (~400 mgal over ~30 km, Nakamura, 2016). The rocks that host the sequence contain several generations of structures relating to over 1.3 Gyr of Earth history, elements of which were exploited by both the Lake Muir M_W > 5 events and subsequent aftershocks. An obvious question is whether there is anything intrinsic to this crustal and/or structural setting that might predispose the region to moderate to large earthquakes?

At a local scale, the intersection of oblique sets of structures has been proposed as a stress concentrator, potentially leading to seismogenic failure in a critically stressed upper crust (Talwani, 1988; Dentith and Featherstone, 2003; Dentith et al., 2009). The same geometric complexity of structural elements that may promote initial failure might not be expected to be conducive to continued strain localisation, as the intersections will tend to displace and thus provide a barrier to further slip. This is consistent with the absence of landscape evidence for Late Pleistocene or Holocene rupture on or proximal to the faults that ruptured in the 2018 Lake Muir Sequence (cf. Figure 3). Further research is required to determine if Lake Noobijup has a tectonic origin, given the coincidence of the lake with the region of greatest subsidence during the September earthquake.

At a large scale, long-term broad-scale regional uplift along the northern margin of the Albany Fraser Orogen is suggested by the youthful relief of the Stirling Ranges (Cotton, 1949)(see Figure 1 and Figure 2 inset for location), and evidence for tens of kilometre-scale warping of Neogene ferruginous duricrust horizons along an axis perpendiculr to the ranges (John Myers, GSWA, pers. com. 2002; http://www.ga.gov.au/neotectonic-feature-distribution/home?featureId=442959). A series of lakes along the southern side of the Stirling Ranges, exhibiting progressively increasing elevation and decreasing incision into their banks towards the west, are also anomalous in this cratonic setting. While these anomalous landforms have not been studied in detail, from the perspective of causative mechanism or seismogenic potential the east-west axis of uplift (i.e., S_{Hmax} parallel) suggests an alternative to the lithospheric-scale, continental-compressive stress field induced, seismogenic buckling mode of deformation evidenced by the Flinders Ranges (Celerier et al., 2005; Sandiford and Quigley, 2009; Cloetingh et al., 2010; Quigley et al., 2010). A mechanism analogous to the contemporary plate motion driven uplift in the southern Australian Newer Volcanic field (Joyce, 1975; Davies and Rawlinson, 2014) may be appropriate. In this setting edge-driven mantle convection has resulted in broad, subdued uplift associated with the volcanic field (the Gambier uplift), and of the non-volcanic Padthaway uplift further west, since the Pliocene (e.g. Wallace et al., 2005; Quigley et al., 2010). Similar to the Stirling Ranges, the Padthaway uplift is almost parallel to the regional compression direction, and is not proven to be associated with any topography-forming recurrent faulting (Quigley et al., 2010).

Modelling suggests that uplift and seismogenesis may be a consequence of the structure of the margin itself, and not reliant on plate motion. The MacDonnell and Petermann Ranges in the Northern Territory (Figure 1) are associated with some of the largest Bouguer gravity anomalies in continental settings world-wide, outside regions of active tectonism (Kennett and Iaffaldano, 2013). Detailed interpretation of the gravity anomalies (Aitken et al., 2009; Aitken et al., 2009), together with the analysis of seismic reflection profiles (Korsch and Kositcin, 2010), indicates that the anomalies relate to wedge-shaped zones bounded by inclined faults, across which the Moho is displaced by up to 15 km (Goleby et al., 1989; Lambeck and Burgess, 1992; Korsch et al., 1998; Hand and Sandiford, 1999). Finite element modelling of the gravitational stresses relating to the crustal architecture across one such fault system, the Redbank Thrust Zone (located along the northern margin of the MacDonnell Ranges – Figure 1), indicates that the region is in broad-scale mechanical equilibrium, despite the local isostatic imbalance (Beekman et al., 1997). However, the models predict the possibility of intraplate seismicity in response to small changes in tectonic stress, since parts of the crust are already at or close to the failure limit. In the case of the Redbank Thrust Zone, the application of compressive stress in the form of the modern crustal stress field (Dickinson et al., 2002; Hillis et al.,

2008; Rajabi et al., 2017b) appears to have perturbed the mechanical equilibrium such that Late Pliocene silcretes have been domed across the axis of the MacDonnell Ranges (Senior et al., 1995), similar to that seen for the duricrust horizons in the Stirling Ranges. Critically, the most highly stressed parts of the Beekman *et al.* (1997) model is the shallow crust in the hanging wall, and the shallow to mid-crust in the footwall, of the structures controlling the isostatic imbalance. Circumstantially, the 2012 Ernabella earthquake (shallow hanging wall of the Woodroffe Thrust) and 2013 Mulga Park earthquake (moderate depth in the footwall of the Woodroffe Thrust) fit this model (Clark and McPherson, 2013; Clark et al., 2014b), as do the 1986 Marryat Creek (Machette et al., 1993; Crone et al., 1997) and 2016 Petermann Ranges (King et al., 2018; Polcari et al., 2018) ruptures, which occurred in the proximal hanging wall of the Woodroffe Thrust. Similar to the MacDonnell Ranges overlying the Redbank Thrust Zone, the Petermann Ranges overlying the Woodroffe Thrust are associated with tens of kilometre-scale landscape warping, as evidenced by the deranged Lake Mackay paleo-drainage (Sandiford et al., 2009).

Enhanced seismogenic potential is also modelled to result from variation in the thermal regime in association with significant lithospheric steps (Sandiford and Egholm, 2008), which are ubiquitously associated with the larger gravity anomalies (cf. Kennett et al., 2013; Kennett and Iaffaldano, 2013). The greater seismogenic potential manifests on the side of the boundary with the thicker lithosphere, by virtue of thermal weakening. The 2001 2002 Burakin earthquake swarm could potentially be attributable to this mechanism (Leonard, 2002; Allen et al., 2006). However, counter examples are provided by the paleo-earthquake scarps and earthquake swarms evenly distributed across the Yilgarn Craton (Clark, 2010; Dent, 2016). So, while a crustal/lithospheric architecture argument *may* be invoked to explain the Lake Muir earthquake sequence, such an argument is not universally applicable across the Precambrian SCR crust of Australia (cf. Figure 1).

4.3 Migration of the locus of moment release in the Southwest Seismic Zone

Pre-historical 'one-off' ruptures cannot generally be detected using widely available and areally extensive digital elevation data (e.g. SRTM, Clark, 2010). Irrespective, neotectonic fault displacements are typically < 5 m across much of the Precambrian SCR (Clark and Allen, 2018). An upper limit on the long-term rates at which the displacement has accrued is provided by regional bedrock erosion rates of < 5 m/Myr (Stone et al., 1994; Belton et al., 2004; Jakica et al., 2010). Displacement accumulation rates over the last 100 kyr can be as high as 30 m/Myr (Clark et al., 2008). Such rates are clearly unsustainable over the long term given the non-mountainous character of the landscape, leading researchers to propose that displacement is highly episodic in this setting (e.g. Crone et al., 1997; Crone et al., 2003; Clark et al., 2008). This finding is consistent with an analysis of the expected relief generation rates by Leonard & Clark (2011) which imply that the historical catalogue of seismicity in the Southwest Seismic Zone (SWSZ) is ten times that required to build the scarps (see also Braun et al., 2009). However, revised earthquake rate estimates based on the remediation of catalogue magnitudes for the NSHA18 (Allen et al., 2018) suggest that long-term forecasts of large earthquake rates in Precambrian crust may have been previously overestimated, which would provide an improved correspondence between the historical and pre-historical earthquake records. Nevertheless, the question remains as to whether the seismic activity within a given area containing neotectonic fault scarps is episodic on individual faults and so migratory within a region (e.g. Liu and Stein, 2016), or whether the locus of seismicity

migrates over time, never to return to previously active regions/faults, as suggested by the paleoseismology of the nine historical surface ruptures.

A plot of earthquake epicentres since 1960 colour coded by age (Figure 10), shows the central core of events that were used by Doyle (1971) to define the extents of the SWSZ. Much of this activity occurred in the two to three decades including and following the Meckering, Calingiri and Cadoux surface rupturing earthquakes. These epicentres are enclosed by a broad ring of more recent epicentres, framing the core on northern, eastern and southern sides. The epicentres, including rare ~ M_W 5 events (e.g., Lake Muir, Burakin), typically fill the interstices between the paleoseismic fault scarps (cf. Clark, 2010). Rarely can epicentres be confidently associated spatially with paleoseismic fault scarps (e.g. within 10 km). The pattern might be interpreted as a cascading destabilisation radiating outwards from the 1968-1979 surface ruptures. While having produced surface rupture in one instance (e.g., Lake Muir), it is not clear whether the destabilisation might be expected to trigger future M_W > 6 events, or if the larger earthquakes occur in response to an as yet unknown alternative mechanism.

Including eight of the nine earthquakes mentioned above, forty-two onshore earthquakes of magnitude M_W ≥5.0 are located in the Australian Precambrian cratonic crust (cf. Allen et al., 2018). Given that hypocentres are typically extremely shallow in the cratonic areas (Leonard, 2008; Clark et al., 2014a), these events may also have ruptured the ground surface, in which case a landscape record may exist and could be investigated to help understand their structural context.

4.4 Future use of InSAR for earthquake studies in Australia

There has been slow uptake of InSAR for earthquake studies in Australia. This is due in part to incomplete SAR data archives available for analysis, and the absence of earthquakes large and/or shallow enough to be detectable by InSAR. Dawson *et al.* (2008) were able to use L-band ALOS-PALSAR interferometry to study the deformation field of two very small earthquakes, but due to poor SAR data availability before and after earthquakes, and interferometric baseline restrictions, it was not possible to study all earthquakes that had occurred.

The C-band Sentinel-1 mission has been a game-changer for InSAR applications because of its near-global coverage and consistent repeat imaging strategy. The availability of this rich data set has enabled global systematic studies of earthquake detectability in InSAR data for the first time (e.g. Barnhart et al., 2019; Funning and Garcia, 2019). Following the launch of Sentinel-1A and Sentinel-1B in 2014 and 2016 respectively, there are now regular SAR acquisitions over the whole Australian continent every 12 days (from descending pass orbits). This means that co-seismic image pairs of 12 days are consistently available, which ensures that interferograms have a good chance of maintaining a coherent phase signal. This will result in many more Australian earthquakes being detected with InSAR in the future.

A limitation of the C-band InSAR is that it does not perform well in all land cover environments. Funning & Garcia (2019) showed that the main control on whether an earthquake is detectable by InSAR is governed by vegetation density and long spatial baselines. Although the latter is well-controlled with Sentinel-1 (with spatial baselines not usually exceeding a couple hundred metres), vegetation density is variable across the Australian continent. Magnitude and depth also play a role in earthquake detectability with InSAR (Dawson and Tregoning, 2007; Funning and Garcia, 2019). Large magnitude earthquakes

~~($M_W \geq 6.7$) produce surface deformation patterns over larger areas that are easier to detect, although localised decorrelation can occur near the rupture zone due to intense ground movement (e.g. Wang et al., 2019). Smaller magnitudes ($M_W \leq 6$) may be difficult to accurately detect due to the smaller spatial extent of deformation patterns. Furthermore, earthquakes that are shallower (< 5 km) are more likely to have a surface expression, while deeper ones may not.~~

5 Conclusions

A shallow M_W 5.3 earthquake near Lake Muir in southwest Western Australia on the 16th of September 2018 was followed on the 8th of November by a ~~co-located~~proximal M_W 5.2 event. Focal mechanisms produced for the events suggest reverse and strike-slip rupture, respectively. ~~Recent improvements in the coverage and frequency of~~In-SAR data ~~over Australia with the Sentinel-1 satellite constellation~~ has allowed for the ~~timely~~ mapping of the surface deformation fields relating to both earthquakes in unprecedented detail, and these are shown to be partly coincident. Field mapping, guided by the InSAR data, reveal that the first event produced an approximately 3 km-long and up to 0.4-0.6 m high west-facing surface rupture, consistent with slip on a moderately east-dipping fault. Interpretation of InSAR data shows that the surface scarp relates to a sub-surface rupture ~5 km long, bound at its north and southern extremities by ~~strike-slip~~ terminal structures, and to the east by a broad zone of landscape depression. The November event did not produce surface rupture.~~New data, and the recognition that InSAR data will increasingly allow for the distinction between "visible" surface rupture lengths (*VSRL*) from field mapping and "detectable" surface rupture lengths (*DSRL*), has prompted a recalculation of the Clark *et al.* (2014b) relation between rupture length and magnitude for SCR earthquakes. The regressions indicate that Australian SCR earthquakes tend to be longer for a given magnitude than elsewhere in the world~~ (e.g. Wells and Coppersmith, 1994; Leonard, 2014)~~.~~ Almost nine hundred aftershocks were recorded by a temporary seismometer deployment. Hypocentre locations correlate poorly with the rupture plane of their respective main-shocks but well with regions of modelled increase in Coulomb stress. The Lake Muir sequence is typical of a class of seismicity within non-extended Precambrian SCR crust involving multiple moderate to large mainshocks with focal mechanisms sharing common compression axes. Multiple triggering mechanisms must be invoked to explain time lags between mainshocks spanning several orders of magnitude.

In some cases, more than half the seismic moment release relating to sequences of this kind has no surface expression, and hence leaves no landscape record, despite typically very shallow hypocentres.

The September M_W 5.3 Lake Muir earthquake was the ninth event documented to have produced surface rupture in Australia in historical times (Figure 1, Table 1). These ruptures~~(Clark et al., 2012)~~ are located exclusively in the non-extended Precambrian SCR rocks of central and western Australia, and none could have been identified and mapped using topographic signature prior to the historical event. A consistent, more fragmentary record exists from analogous crust worldwide. The pattern is repeated with ruptures from the paleoseismic record, which show only very limited evidence for recurrence. Hence, the underpinning assumption that a 'long-term slip rate' is a meaningful concept in all classes of intraplate crust, as per the prevailing plate margin paradigm, remains to be fully tested. Within non-extended Precambrian SCR crust~~A pattern is also~~

~~emerging where 'one-off' ruptures, as evidenced by the historic surface-breaking earthquakes, are filling the spaces between mapped multi-event neotectonic scarps . Despite such observations, patterns of migration in intraplate seismicity, particularly in Precambrian SCR crust, are yet to be fully understood .~~, 'one-off' or 'limited recurrence' ruptures may be the norm, with obvious implications for seismic hazard assessment.

Data availability

Source parameters of the earthquakes prior to relocation were obtained from the Geoscience Australia catalog https://earthquakes.ga.gov.au/ (last accessed 08.02.2019). The original and relocated datasets are obtainable from the Geoscience Australia Github repository https://github.com/GeoscienceAustralia/GA-neotectonics/tree/master/Lake_Muir_Solid_Earth_data. Focal mechanisms for the three largest events were obtained from https://earthquake.usgs.gov/earthquakes/ as per Table 2. ~~The datafile and code written to regress the length versus magnitude data, and t~~The UAV DTM of difference GeoTIFF files are also obtainable from the Geoscience Australia Github repository, using the above link. The DCBA LiDAR dataset was used under licence and cannot be provided to third parties. The Sentinel-1 SAR data is available from https://copernicus.nci.org.au/sara.client/#/home and t~~T~~he precise orbital ephemerides products used ~~in~~ to correct~~ing~~ the InSAR data are available from https://qc.sentinel1.eo.esa.int/aux_poeorb/.

Author contribution

DC and SS designed the field experiments and executed them. GB relocated the ~~seismicity~~ aftershock data and wrote related sections of the manuscript and supplementary material. JD relocated the main shocks and wrote related sections of the manuscript and supplementary material. TA ~~developed the regression code for assessing relationships between moment magnitude and surface rupture length~~curated the seismological data and co-wrote related sections of the manuscript. SB acquired and processed the InSAR data. MG assisted SB in writing up related sections of the manuscript. DC prepared the manuscript with contributions from all co-authors.

Competing interests

The authors declare that they have no conflicts of interest.

Acknowledgements

Thanks to Roger Hearn of Manjimup for conducting the initial field reconnaissance and taking the first photos of the scarp. Thanks also to Rob De Campo and Mark Muir for providing access to their properties to conduct fieldwork. Guorong Hu of Geoscience Australia kindly processed the GPS data. Jasmine Rutherford from the Western Australia DBCA is warmly thanked for providing access to their LiDAR data. Cristiano Collettini and an anonymous reviewer are thanked for their comments, which greatly improved the quality of the manuscript. This manuscript is published with the permission of the CEO of Geoscience Australia.

References

Adams, J., Wetmiller, R., Hasegawa, H., and Drysdale, J.: The first surface faulting from a historical earthquake in North America, Nature, 352, 617619, 1991.

Adams, J., Percival, J., Wetmiller, R., Drysdale, J., and Robertson, P.: Geological controls on the 1989 Ungava surface rupture a preliminary interpretation, Geological Survey of Canada Paper, 92C, 147155, 1992.

Agisoft LCC: . Agisoft PhotoScan Pro 1.4.3. Available online: http://www.agisoft.com (accessed November 2018).

Aitken, A. R. A., Betts, P. G., and Ailleres, L.: The architecture, kinematics, and lithospheric processes of a compressional intraplate orogen occurring under Gondwana assembly: the Petermann Orogeny, central Australia, Lithosphere 1, 343-357, 2009.

Aitken, A. R. A., Betts, P. G., Weinberg, R. F., and Gray, D.: Constrained potential field modeling of the crustal architecture of the Musgrave Province in central Australia: evidence for lithospheric strengthening due to crust-mantle boundary uplift, Journal of Geophysical Research 111, B12405, http://dx.doi.org/10.1029/2008JB006194, 2009

Allen, T., Clark, D., Lawrie, S., Brenn, G., Dimech, J., Garthwaite, M., Glanville, H., Kemp, T., Lintvelt, C., Lumley, D., Pejic, T., Sayin, E., and Standen, S.: The 2018 Lake Muir earthquakes: Australia's ninth surface rupturing earthquake sequence in 50 years, Seismological Research Letters, 90 951, 2019.

Allen, T. I., Dhu, T., Cummins, P. R., and Schneider, J. F.: Empirical Attenuation of Ground-Motion Spectral Amplitudes in Southwestern Western Australia, Bulletin of the Seismological Society of America, 96, 572-585, 2006.

Allen, T. I., Leonard, M., Ghasemi, H., and Gibson, G.: The 2018 National Seismic Hazard Assessment for Australia – earthquake epicentre catalogue, Geoscience Australia Record 2018/30, doi: 10.11636/Record.2018.030, 2018.

Allen, T. I.: Seismic hazard estimation in stable continental regions: does PSHA meet the needs for modern engineering design in Australia?, Bulletin of the New Zealand Society for Earthquake Engineering, 53, 22-36, 2020.

Allmann, B. P., and Shearer, P. M.: Global variations of stress drop for moderate to large earthquakes, Journal of Geophysical Research: Solid Earth, 114, B01310, 10.1029/2008jb005821, 2009.

Amarjargal, S., Kato, T., Furuya, M. J. E., Planets, and Space: Surface deformations from moderate-sized earthquakes in Mongolia observed by InSAR, 65, 713-723, 10.5047/eps.2012.12.015, 2013.

Anderson, E.: The Dynamics of Faulting and Dyke Formation with applications to Britain (2nd edition), Oliver and Boyd, Edinburgh, 1951.

Anderson, E. M.: The dynamics of faulting, Transactions of the Edinburgh Geological Society, 8, 387–402, 1905.

Barnhart, W. D., Hayes, G. P., and Wald, D. J.: Global Earthquake Response with Imaging Geodesy: Recent Examples from the USGS NEIC, 11, 1357, 2019.

Bates, D. A.: Geological effects of the (Accra) earthquake, Gold Coast Geological Survey Bulletin, 13, 18-41, 1941.

Baumbach, M., Grosser, H., Schmidt, H. G., Paulat, A., Rietbrock, A., Ramakrishna Rao, C. V., Raju, P. S., Sarkar, D., and Mohan, I.: Study of the foreshocks and aftershocks of the intraplate Latur earthquake of September 30, 1993, India in Latur Earthquake, edited by H. K. Gupta, Memoir of the Geological Society of India, 35, 33– 63, 1994.

Beekman, F., Stephenson, R. A., and Korsch, R. J.: Mechanical stability of the Redbank Thrust Zone, Central Australia: Dynamic and rheological implications Australian Journal of Earth Sciences, 44, 215-226, 1997.

Belardinelli, M. E., Bizzarri, A., and Cocco, M.: Earthquake triggering by static and dynamic stress changes, 108, 10.1029/2002jb001779, 2003.

Belton, D. X., Brown, R. W., Kohn, B. P., Fink, D., and Farley, K. A.: Quantitative resolution of the debate over antiquity of the central Australian landscape: implications for the tectonic and geomorphic stability of cratonic interiors, Earth and Planetary Science Letters, 219, 21-34, 2004.

Bent, A. L.: The 1989 (Ms 6.3) Ungava, Quebec, Earthquake: a Complex Intraplate Event, Bulletin of the Seismological Society of America, 84, 1075-1088, 1994.
Boncio, P., Liberi, F., Caldarella, M., and Nurminen, F.-C.: Width of surface rupture zone for thrust earthquakes: implications for earthquake fault zoning, Natural Hazards and Earth System Sciences, 18, 241-256, https://doi.org/10.5194/nhess-18-241-2018, 2018.
Bonini, M., Sani, F., and Antonielli, B.: Basin inversion and contractional reactivation of inherited normal faults: A review based on previous and new experimental models, Tectonophysics, 522-523, 55-88, 2012.
Bowman, J. R., Gibson, G., and Jones, T.: Aftershocks of the 1988 January 22 Tennant Creek, Australia intraplate earthquakes: evidence for a complex thrust-fault geometry, International Geophysical Journal, 100, 87-97, 1990.
Bowman, J. R.: The 1988 Tennant Creek, Northern Territory, earthquakes: a synthesis, Australian Journal of Earth Sciences, 39, 651-669, 1992.
Bratt, S. R., and Bache, T. C.: Locating events with a sparse network of regional arrays, Bulletin of the Seismological Society of America, 78, 780–798, 1988.
Braun, J., Burbidge, D., Gesto, F., Sandiford, M., Gleadow, A., Kohn, B., and Cummins, P.: Constraints on the current rate of deformation and surface uplift of the Australian continent from a new seismic database and low-T thermochronological data, Australian Journal of Earth Sciences, 56, 99-110, 2009.
Brodsky, E. E., Roeloffs, E., Woodcock, D., Gall, I., and Manga, M.: A mechanism for sustained groundwater pressure changes induced by distant earthquakes, 108, 10.1029/2002jb002321, 2003.
Brodsky, E. E., and Elst, N. J. v. d.: The Uses of Dynamic Earthquake Triggering, 42, 317-339, 10.1146/annurev-earth-060313-054648, 2014.
Brune, J. N.: Tectonic stress and the spectra of seismic shear waves from earthquakes, J. Geophys. Res., 75, 4997-5009, 1970.
Calais, E., Mattioli, G., DeMets, C., Nocquet, J. M., and Stein, S.: Tectonic strain in plate interiors?, Nature Geoscience, 438, E9-E10, 2005.
Calais, E., Camelbeeck, T., Stein, S., Liu, M., and Craig, T. J.: A New Paradigm for Large Earthquakes in Stable Continental Plate Interiors, Geophysical Research Letters, 10.1002/2016GL070815, 2016.
Camacho, A., Vernon, R. H., and Fitzgerald, J. D.: Large volumes of anhydrous pseudotachylyte in the Woodroffe Thrust, eastern Musgrave Ranges, Australia, Journal of Structural Geology, 17, 371- 383, 1995.
Camacho, A., and McDougall, I.: Intracratonic, strike-slip partitioned transpression and the formation and exhumation of eclogite facies rocks: An example from the Musgrave Block, central Australia, Tectonics, 19, 978-996, 2000.
Caskey, S. J., and Wesnousky, S. G.: Static stress changes and earthquake triggering during the 1954 Fairview Peak and Dixie Valley earthquakes, central Nevada, Bulletin of the Seismological Society of America, 87, 521-527, 1997.
Celerier, J., Sandiford, M., Hansen, D. L., and Quigley, M.: Modes of active intraplate deformation, Flinders Ranges, Australia, Tectonics, 24, doi:10.029/2004&C001679, 2005.
Chakravartula, P. N., and Street, G.: Hydrogeological interpretation of airborne geophysical data Lake Muir–Unicup catchment, Western Australia, Unpublished Agraria Limited report, https://library.dbca.wa.gov.au/static/FullTextFiles/000308.pdf, 45p, 2000.
Chappell, J.: Australian landscape processes measured with cosmogenic nuclides, in: Regolith Geochronology and Landscape Evolution, edited by: Pillans, B., CRC LEME, Perth, 19-26, 2006.
Chiu, J.-M., Johnston, A. C., Metzger, A. G., Haar, L., and Fletcher, J.: Analysis of analog and digital records of the 1982 Arkansas earthquake swarm, Bulletin of the Seismological Society of America, 74, 1721-1742, 1984.
Choy, G. L., and Bowman, J. R.: Rupture process of a multiple main shock sequence; analysis of teleseismic, local, and field observations of the Tennant Creek, Australia, earthquakes of January 22, 1988, Journal of Geophysical Research, B, Solid Earth and Planets, 95, 6867-6882, 1990.
Clark, D., Dentith, M., Wyrwoll, K. H., Yanchou, L., Dent, V., and Featherstone, C.: The Hyden fault scarp, Western Australia: paleoseismic evidence for repeated Quaternary displacement in an intracratonic setting, Australian Journal of Earth Sciences, 55, 379-395, 2008.
Clark, D.: Identification of Quaternary scarps in southwest and central west Western Australia using DEM-based hill shading: application to seismic hazard assessment and neotectonics, International Journal of Remote Sensing, 31, 6297-6325, 2010.
Clark, D.: Neotectonic Features Database, Geoscience Australia. Australia, G. (Ed.), http://pid.geoscience.gov.au/dataset/ga/74056, Canberra, 2012.
Clark, D., McPherson, A., and Van Dissen, R.: Long-term behaviour of Australian Stable Continental Region (SCR) faults, Tectonophysics 566-567, 1-30, http://dx.doi.org/10.1016/j.tecto.2012.07.004, 2012.
Clark, D., and McPherson, A.: A tale of two seisms: Ernabella 23/03/2012 (Mw5.4) and Mulga Park 09/06/2013 (Mw 5.6), Australian Earthquake Engineering Society Newsletter, 2013/3, 7-11, 2013.
Clark, D., McPherson, A., and Allen, T.: Intraplate earthquakes in Australia, in: Intraplate Earthquakes, edited by: Talwani, P., Cambridge University Press, New York, 8-49, 2014a.
Clark, D., McPherson, A., Allen, T., and De Kool, M.: Co-seismic surface deformation relating to the March 23, 2012 MW 5.4 Ernabella (Pukatja) earthquake, central Australia: implications for cratonic fault scaling relations, Bulletin of the Seismological Society of America, 104, 24-39, doi: 10.1785/0120120361, 2014b.

Clark, D., McPherson, A., Cupper, M., Collins, C. D. N., and Nelson, G.: The Cadell Fault, southeastern Australia: a record of temporally clustered morphogenic seismicity in a low-strain intraplate region, in: Geological Society, London, Special Publication *Seismicity, Fault Rupture and Earthquake Hazards in Slowly Deforming Regions*, edited by: Landgraf, A., Kuebler, S., Hintersburger, E., and Stein, S., 2015.
Clark, D., McPherson, A., Pillans, B., White, D., and Macfarlane, D.: Potential geologic sources of seismic hazard in Australia's south-eastern highlands: what do we know?, Australian Earthquake Engineering Society 2017 Conference, Nov 24-26, Canberra, ACT, https://www.aees.org.au/wp-content/uploads/2018/2002/2420-Dan-Clark.pdf, 2017.
Clark, D., and Allen, T.: What have we learnt of cratonic earthquakes in the fifty years since Meckering?, Australian Earthquake Engineering Society 2018 Conference, Perth, Western Australia, 2018.
Clark, D., and Edwards, M.: 50th anniversary of the 14th October 1968 MW 6.5 (MS 6.8) Meckering earthquake. Australian Earthquake Engineering Society Pre-conference Field Trip, Meckering, 15 November 2018, Geoscience Australia Record, 2018/39, 47, 2018.
Clark, D. J., and Leonard, M.: Principal stress orientations from multiple focal plane solutions: new insight in to the Australian intraplate stress field, in: Evolution and dynamics of the Australian Plate, edited by: Hillis, R. R., and Muller, D., Geological Society of America Special Paper, 91-105, 2003.
Cloetingh, S., Burov, E. B., and Poliakov, A.: Lithosphere folding: Primary response to compression? (from central Asia to Paris basin) Tectonics, 18, 1064-1083, 2010.
Commander, P., Schoknecht, N., Verboom, B., and Caccetta, P.: The Geology, Physiology and soils of Wheatbelt Valleys, Proceedings of the Wheatbelt Valleys Conference, Perth, Australia., 28p, 2001.
Copley, A., Mitra, S., Sloan, R. A., Gaonkar, S., and Reynolds, K.: Active faulting in apparently stable peninsular India: Rift inversion and a Holocene-age great earthquake on the Tapti Fault, 119, 6650-6666, 10.1002/2014jb011294, 2014.
Costantini, M.: A novel phase unwrapping method based on network programming, IEEE transactions on geoscience and remote sensing, 36, 813–821, doi: 10.1109/36.673674, 1998.
Cotton, C. A.: A Review of Tectonic Relief in Australia, The Journal of Geology, 57, 280-296, 10.1086/625609, 1949.
Cox, R. T., Van Arsdale, R., Clark, D., Hill, A., and Lumsden, D.: A Revised Paleo-Earthquake Chronology on the Southeast Reelfoot Rift Margin near Memphis, Tennessee, Seismological Research Letters, 84, 402-408, doi: 10.1785/0220120142, 2013.
Craig, T. J., Calais, E., Fleitout, L., Bollinger, L., and Scotti, O.: Evidence for the release of long-term tectonic strain stored in continental interiors through intraplate earthquakes, Geophysical Research Letters, 43, doi:10.1002/2016GL069359, 2016.
Crone, A. J., and Luza, K. V.: Style and timing of Holocene surface faulting on the Meers Fault, southwestern Oklahoma, Geological Society of America Bulletin, 102(1), 1-17, 1990.
Crone, A. J., Machette, M. N., and Bowman, J. R.: Geologic investigations of the 1988 Tennant Creek, Australia, earthquakes - implications for paleoseismicity in stable continental regions, United States Geological Survey Bulletin, 2032-A, 51p, 1992.
Crone, A. J., and Machette, M. N.: Holocene faulting on the Cheraw Fault, southeastern Colorado another hazardous late Quaternary fault in the stable continental interior, EOS supplement (November 7, 1995), 76, F362, 1995.
Crone, A. J., Machette, M. N., and Bowman, J. R.: Episodic nature of earthquake activity in stable continental regions revealed by palaeoseismicity studies of Australian and North American Quaternary faults, Australian Journal of Earth Sciences, 44, 203-214, 1997.
Crone, A. J., de Martini, P. M., Machette, M. N., Okumura, K., and Prescott, J. R.: Paleoseismicity of Two Historically Quiescent Faults in Australia: Implications for Fault Behavior in Stable Continental Regions, Bulletin of the Seismological Society of America, 93, 1913-1934, 2003.
Davies, D. R., and Rawlinson, N.: On the origin of recent intraplate volcanism in Australia, Geology, 43, doi: 10.1130/G36093.1, 2014.
Dawson, J., and Tregoning, P.: Uncertainty analysis of earthquake source parameters determined from InSAR: A simulation study, Journal of Geophysical Research: Solid Earth, 112, 10.1029/2007jb005209, 2007.
Dawson, J., Cummins, P., Tregoning, P., and Leonard, M.: Shallow intraplate earthquakes in Western Australia observed by Interferometric Synthetic Aperture Radar, Journal of Geophysical Research, 113, doi:10.1029/2008JB005807, 2008.
Denham, D., Alexander, L. G., and Worotnicki, G.: The stress field near the sites of the Meckering (1968) and Calingiri (1970) earthquakes, Western Australia, Tectonophysics, 67, 283-317, 1980.
Denham, D., Alexander, L. G., Everingham, I. B., Gregson, P. J., McCaffrey, R., and Enever, J. R.: The 1979 Cadoux earthquake and intraplate stress in Western Australia, Australian Journal of Earth Sciences, 34, 507-521, 1987.
Dent, V. F.: A preliminary map of cluster locations in southwest Western Australia, 1990 – 2016, Joint Conference of the Australian Earthquake Engineering Society and the Asian Seismological Commission, Melbourne, Australia, Paper 391, 2016.
Dentith, M., Clark, D., and Featherstone, W.: Aeromagnetic mapping of Precambrian geological structures that controlled the 1968 Meckering earthquake (Ms 6.8): Implications for intraplate seismicity in Western Australia, Tectonophysics, 475, 544-553, 2009.
Dentith, M. C., Dent, V. F., and Drummond, B. J.: Deep crustal structure in the southwestern Yilgarn Craton, Western Australia, Tectonophysics, 325, 227-255, 2000.
Dentith, M. C., and Featherstone, W. E.: Controls on intra-plate seismicity in southwestern Australia, Tectonophysics, 376, 167-184, 2003.
DeVries, P. M. R., Krastev, P. G., and Meade, B. J.: Geodetically constrained models of viscoelastic stress transfer and earthquake triggering along the North Anatolian fault, 17, 2700-2716, 10.1002/2016gc006313, 2016.

Dickinson, J. A., Wallace, M. W., Holdgate, G. R., Gallagher, S. J., and Thomas, L.: Origin and timing of the Miocene-Pliocene unconformity in southeast Australia, Journal of Sedimentary Research, 72, 288-303, 2002.
Doyle, H. A.: Seismicity and structure in Australia, Bulletin of the Royal Society of New Zealand, 9, 149-152, 1971.
Drummond, B. J., and Mohamed, R. E.: Crustal structure in the Southwest Seismic Zone, Western Australia, Abstracts - Geological Society of Australia. 15; Pages 59-60. 1986.: Geological Society of Australia. Sydney, N.S.W., Australia. 1986., 1986.
Drummond, B. J., Goleby, B. R., and Swager, C. P.: Crustal signature of Late Archaean tectonic episodes in the Yilgarn Craton, Western Australia: evidence from deep seismic sounding, Tectonophysics, 329, 193-221, 2000.
Ellis, M. A., and Densmore, A. L.: First-order topography over blind thrusts, in: Tectonics, Climate, and Landscape Evolution, edited by: Willett, S. D., Hovius, N., Brandon, M. T., and Fisher, D. M., Geological Society of America, 2006.
Estrada, B.: Neotectonic and palaeoseismological studies in the southwest of Western Australia, PhD, School of Earth and Environment, The University of Western Australia, Perth, 2009.
Everingham, I. B.: The crustal structure of the southwest of Western Australia, BMR Record, 1965/97, 1965.
Everingham, I. B., and Gregson, P. J.: Magnetometer traverses across aeromagnetic anomalies near recent earthquake fault scarps in southwestern Australia, AGSO Record, 1996/55, 33, 1996.
Felzer, K. R., Abercrombie, R. E., and Ekström, G. r.: Secondary Aftershocks and Their Importance for Aftershock Forecasting, Bulletin of the Seismological Society of America, 93, 1433-1448, 10.1785/0120020229 %J Bulletin of the Seismological Society of America, 2003.
Fisk, M. D.: Accurate Locations of Nuclear Explosions at the Lop Nor Test Site Using Alignment of Seismograms and IKONOS Satellite Imagery, Bulletin of the Seismological Society of America, 92, 2911-2925, 10.1785/0120010268 %J Bulletin of the Seismological Society of America, 2002.
Fitzsimons, I. C. W., and Buchan, C.: Geology of the western Albany–Fraser Orogen, Western Australia — a fi eld guide, Western Australia Geological Survey, Record 2005/11, 32p, 2005.
Fuhrmann, T., and Garthwaite, M. C.: Resolving Three-Dimensional Surface Motion with InSAR: Constraints from Multi-Geometry Data Fusion, Remote Sensing, 11, 241, 2019.
Funning, G. J., and Garcia, A.: A systematic study of earthquake detectability using Sentinel-1 Interferometric Wide-Swath data, Geophysical Journal International, 216, 332-349, 2019.
Gardonio, B., Jolivet, R., Calais, E., and Leclère, H.: The April 2017 Mw6.5 Botswana Earthquake: An Intraplate Event Triggered by Deep Fluids, 45, 8886-8896, 10.1029/2018gl078297, 2018.
Geological Survey of Western Australia: 1:500 000 State interpreted bedrock geology of Western Australia, 2016. Geological Survey of Western Australia (Ed.), Perth, Western Austalia,, 2016.
Geoscience Australia: Geoscience Australia, 1 second SRTM Digital Elevation Model (DEM). Bioregional Assessment Source Dataset. Viewed November 2018. 2011.
Gindraux, S., Boesch, R., and Farinotti, D.: Accuracy Assessment of Digital Surface Models from Unmanned Aerial Vehicles' Imagery on Glaciers, Remote Sensing, 9, 186, 2017.
Goedhart, M. L., and Booth, P. W. K.: A palaeoseismic trench investigation of early Holocene neotectonic faulting along the Kango Fault, southern Cape Fold Belt, South Africa – Part I: stratigraphic and structural features, South African Journal of Geology, 119, 545-568, https://doi.org/10.2113/gssajg.119.3.545, 2016.
Gold, R. D., Clark, D., Barnhart, W. D., King, T., Quigley, M., and Briggs, R. W.: Surface rupture and distributed deformation revealed by optical satellite imagery: The intraplate 2016 Mw 6.0 Petermann Ranges earthquake, Australia, Geophysical Research Letters, 46, https://doi.org/10.1029/2019GL084926, 2019.
Goldstein, R. M., Zebker, H. A., and Werner, C. L.: Satellite radar interferometry: Two-dimensional phase unwrapping, Radio Science, 23, 713-720, 1988.
Goldstein, R. M., and Werner, C. L.: Radar interferogram filtering for geophysical applications, Geophysical Research Letters, 25, 4035–4038, doi: 10.1029/1998GL900033, 1998.
Goleby, B. R., Shaw, R. D., Wright, C., Kennett, B. L. N., and Lambeck, K.: Geophysical evidence for 'thick-skinned' crustal deformation in central Australia, Nature, 337, 325-330, 1989.
Goleby, B. R., Rattenbury, M. S., Swager, C. P., Drummond, B. J., Williams, P. R., Sheraton, J. W., and Heinrich, C. A.: Archaean crustal structure from seismic reflection profiling, Eastern Goldfields, Western Australia, Australian Geological Survey Organisation Record, 1993/15, 1993.
Gomberg, J., and Johnson, P.: Dynamic triggering of earthquakes, Nature, 437, 830-830, 10.1038/437830a, 2005.
Gordon, F. R., and Lewis, J. D.: The Meckering and Calingiri earthquakes October 1968 and March 1970, Western Australia Geological Survey Bulletin, 126, 229p, 1980.
Griffin, J. D., Allen, T. I., and Gerstenberger, M. C.: Seismic Hazard Assessment in Australia: Can Structured Expert Elicitation Achieve Consensus in the "Land of the Fair Go"?, Seismological Research Letters, 10.1785/0220190186, 2020.
Gupta, H. K., Rastogi, B. K., Mohan, I., Rao, C. V. R. K., Sarma, S. V. S., and Rao, R. U. M.: An investigation into the Latur earthquake of September 29, 1993 in southern India, Tectonophysics, 287, 299-318, https://doi.org/10.1016/S0040-1951(98)80075-9, 1998.

Hamling, I. J., Hreinsdóttir, S., Clark, K., Elliott, J., Liang, C., Fielding, E., Litchfield, N., Villamor, P., Wallace, L., Wright, T. J., D'Anastasio, E., Bannister, S., Burbidge, D., Denys, P., Gentle, P., Howarth, J., Mueller, C., Palmer, N., Pearson, C., Power, W., Barnes, P., Barrell, D. J. A., Van Dissen, R., Langridge, R., Little, T., Nicol, A., Pettinga, J., Rowland, J., and Stirling, M.: Complex multifault rupture during the 2016 Mw 7.8 Kaikōura earthquake, New Zealand, Science, 356, eaam7194, 10.1126/science.aam7194, 2017.

Hand, M., and Sandiford, M.: Intraplate deformation in central Australia, the link between subsidence and fault reactivation, Tectonophysics, 305, 121-140, 1999.

Hanks, T. C., and Kanamori, H.: A moment magnitude scale, Journal of Geophysical Research, 84, 2348-2350, 1979.

Hardebeck, J. L., and Okada, T.: Temporal Stress Changes Caused by Earthquakes: A Review, 123, 1350-1365, 10.1002/2017jb014617, 2018.

Harris, L. B.: Polyphase faulting in the Perth Basin and Yilgarn Craton margin, Western Australia: relationship to Upper Palaeozoic-Mesozoic tectonics of Gondwanaland, Gondwana nine. Ninth International Gondwana Symposium, Hyderabad, India, 10-14 January, 1994. Papers. Volume 2. Rotterdam: A.A. Balkema., p1051-1060; 3 fig, 35 ref, 1996.

Henry, C., and Das, S.: Aftershock zones of large shallow earthquakes: fault dimensions, aftershock area expansion and scaling relations, Geophysical Journal International, 147, 272-293, 10.1046/j.1365-246X.2001.00522.x, 2001.

Hill, D. P., Reasenberg, P. A., Michael, A., Arabaz, W. J., Beroza, G., Brumbaugh, D., Brune, J. N., Castro, R., Davis, S., dePolo, D., Ellsworth, W. L., Gomberg, J., Harmsen, S., House, L., Jackson, S. M., Johnston, M. J. S., Jones, L., Keller, R., Malone, S., Munguia, L., Nava, S., Pechmann, J. C., Sanford, A., Simpson, R. W., Smith, R. B., Stark, M., Stickney, M., Vidal, A., Walter, S., Wong, V., and Zollweg, J.: Seismicity Remotely Triggered by the Magnitude 7.3 Landers, California, Earthquake, 260, 1617-1623, 10.1126/science.260.5114.1617 %J Science, 1993.

Hillis, R. R., Sandiford, M., Reynolds, S. D., and Quigley, M. C.: Present-day stresses, seismicity and Neogene-to-Recent tectonics of Australia's 'passive' margins: intraplate deformation controlled by plate boundary forces, in: The Nature and Origin of Compression in Passive Margins, edited by: Johnson, H., Dore´ , A. G., Gatliff, R. W., Holdsworth, R., Lundin, E. R., and Ritchie, J. D., Geological Society, London, Special Publications, 71-90, 2008.

Hornsby, K. T., Streig, A. R., Bennett, S. E. K., Chang, J. C., and Mahan, S.: Neotectonic and Paleoseismic Analysis of the Northwest Extent of Holocene Surface Deformation along the Meers Fault, Oklahoma, Bulletin of the Seismological Society of America, 10.1785/0120180148 %J Bulletin of the Seismological Society of America, 2019.

Jakica, S., Quigley, M., Sandiford, M., Clark, D., Fifield, K., and Alimanovic, A.: Geomorphic and cosmogenic nuclide constraints on escarpment evolution in an intraplate setting, Darling Escarpment, Western Australia, Earth Surface Processes and Landforms, DOI: 10.1002/esp.2058, DOI: 10.1002/esp.2058, 2010.

Janssen, D. P., Collins, A. S., and Fitzsimons, I. C. W.: Structure and tectonics of the Leeuwin Complex and Darling Fault Zone, southern Pinjarra Orogen, Western Australia – a field guide, Geological Survey of Western Australia Record, 2003/15, 33p 2003.

Johnson, P. A., and Jia, X.: Nonlinear dynamics, granular media and dynamic earthquake triggering, Nature, 437, 871-874, 10.1038/nature04015, 2005.

Johnston, A. C.: Seismotectonic interpretations and conclusions from the stable continental region seismicity database, in: The earthquakes of stable continental regions-v. 1, Assessment of large earthquake potential, edited by: Johnston, A. C., Coppersmith, K. J., Kanter, L. R., and Cornell, C. A., Electric Power Research Institute, Palo Alto, California, 4-1-4-103, 1994a.

Johnston, A. C.: The stable continental region database, in: The earthquakes of stable continental regions-v. 1, Assessment of large-earthquake potential, edited by: Johnston, A. C., Coppersmith, K. J., Kanter, L. R., and Cornell, C. A., Electric Power Research Institute, Palo Alto, California, 3-1-3-80, 1994b.

Johnston, A. C., Coppersmith, K. J., Kanter, L. R., and Cornell, C. A.: The earthquakes of stable continental regions, Electric Power Research Institute Report., TR102261V1, 1994.

Joyce, E. B.: Quaternary volcanism and tectonics in southeastern Australia, Bulletin - Royal Society of New Zealand. 13; Pages 169-176. 1975.: The Royal Society of New Zealand. Wellington, New Zealand. 1975., 1975.

Kennett, B. L. N., Fitchner, A., Fishwick, S., and Yoshizawa, K.: Australian Seismological Reference Model (AuSREM): mantle component, Geophysical Journal International, 192, 871-887, 2013.

Kennett, B. L. N., and Iaffaldano, G.: Role of lithosphere in intra-continental deformation: Central Australia, Gondwana Research, 24, 958-968, 2013.

Keranen, K. M., Savage, H. M., Abers, G. A., and Cochran, E. S.: Potentially induced earthquakes in Oklahoma, USA: Links between wastewater injection and the 2011 Mw 5.7 earthquake sequence, Geology, doi:10.1130/G34045.1, 2013.

King, G. C., Stein, R. S., and Rundle, J. B.: The Growth of Geological Structures by Repeated Earthquakes 1. Conceptual Framework Journal of Geophysical Research, 93, 13,307-313,318, 1988.

King, T., Quigley, M. C., and Clark, D.: Surface effects produced by the Mw 6.1 20th May 2016 Petermann earthquake (Australia) and their use in Environmental Seismic Intensity evaluation, Tectonophysics, 747-748, 357-372, 2018.

King, T. R., Quigley, M., and Clark, D.: Surface-Rupturing Historical Earthquakes in Australia and Their Environmental Effects: New Insights from Re-Analyses of Observational Data, Geosciences, 9, 408, 2019.

Klinger, Y., Okubo, K., Vallage, A., Champenois, J., Delorme, A., Rougier, E., Lei, Z., Knight, E. E., Munjiza, A., Satriano, C., Baize, S., Langridge, R., and Bhat, H. S.: Earthquake Damage Patterns Resolve Complex Rupture Processes, 45, 10,279-210,287, 10.1029/2018gl078842, 2018.
Korsch, R. J., Goleby, B. R., Leven, J. H., and Drummond, B. J.: Crustal architecture of central Australia based on deep seismic reflection profiling, Tectonophysics, 288, 57-69, 1998.
Korsch, R. J., and Kositcin, N.: GOMA (Gawler Craton-Officer Basin-Musgrave Province-Amadeus Basin) Seismic and MT Workshop 2010. In: Geoscience Australia, Record, 2010.
Krischer, L.: hypoDDpy: hypoDDpy 1.0 Zenodo, 2015.
Lambeck, K., and Burgess, G.: Deep crustal structure of the Musgrave Block, central Australia: results from teleseismic travel time anomalies, Australian Journal of Earth Sciences 39 1–19, 1992.
Langer, C. J., Bonilla, M. G., and Bollinger, G. A.: Aftershocks and surface faulting associated with the Guinea, West Africa, earthquake of 22 December 1983, Seismological Society of America Bulletin, 77, 1579-1601, 1987.
Leonard, M.: The Burrakin WA earthquake sequence Sept 2000 - June 2002, Australian Earthquake Engineering Society Conference - Total Risk Management in the Privatised Era, Adelaide, Paper 22, 2002.
Leonard, M., Ripper, I. D., and Li, Y.: Australian earthquake fault plane solutions, Geoscience Australia Record, 2002/19, 2002.
Leonard, M.: One hundred years of earthquake recording in Australia, Bulletin of the Seismological Society of America, 98, 1458-1470, 2008.
Leonard, M., and Clark, D.: A record of stable continental region earthquakes from Western Australia spanning the late Pleistocene: Insights for contemporary seismicity, Earth and Planetary Science Letters, 309, 207-212, 2011.
Leonard, M.: Self Consistent Earthquake Fault Scaling Relations: Update and Extension to Stable Continental Strike-Slip Faults, Bulletin of the Seismological Society of America, 104, 2953-2965, 2014.
Leonard, M., Burbidge, D. R., Allen, T. I., Robinson, D. J., McPherson, A., Clark, D., and Collins, C. D. N.: The Challenges of Probabilistic Seismic Hazard Assessment in Stable Continental Interiors: An Australian Example Bulletin of the Seismological Society of America 104, 3008-3028, 10.1785/0120130248, 2014.
Lewis, J. D., Daetwyler, N. A., Bunting, J. A., and Moncrieff, J. S.: The Cadoux earthquake, Western Australia, Geological Survey Report, 1981/11, 133, 1981.
Lin, A., Guo, J., and Fu, B.: Co-seismic mole track structures produced by the 2001 Ms 8.1 Central Kunlun earthquake, China, Journal of Structural Geology, 26, 1511-1519, 2004.
Lin, A., Maruyama, T., Aaron, S., Michibayashi, K., Camacho, A., and Kano, K.: Propagation of seismic slip from brittle to ductile crust: Evidence from pseudotachylyte of the Woodroffe thrust, central Australia, Tectonophysics, 402, 21-35, 2005.
Lin, J., and Stein, R. S.: Stress triggering in thrust and subduction earthquakes and stress interaction between the southern San Andreas and nearby thrust and strike-slip faults, Journal of Geophysical Research: Solid Earth, 109, doi:10.1029/2003JB002607, 2004.
Liu, M., and Stein, S.: Mid-continental earthquakes: Spatiotemporal occurrences, causes, and hazards, Earth Science Reviews, 10.1016/j.earscirev.2016.09.016, 2016.
Livio, F., Serva, L., and Gürpinar, A.: Locating distributed faulting: Contributions from InSAR imaging to Probabilistic Fault Displacement Hazard Analysis (PFDHA), Quaternary International, 451, 223-233, https://doi.org/10.1016/j.quaint.2016.09.034, 2017.
Livio, F., Kettermann, M., Reicherter, K., and Urai, J. L.: Growth of bending-moment faults due to progressive folding: Insights from sandbox models and paleoseismological implications, Geomorphology, 326, 152-166, https://doi.org/10.1016/j.geomorph.2018.02.012, 2019.
Lopes, A. E. V., Assumpção, M., Do Nascimento, A. F., Ferreira, J. M., Menezes, E. A. S., and Barbosa, J. R.: Intraplate earthquake swarm in Belo Jardim, NE Brazil: reactivation of a major Neoproterozoic shear zone (Pernambuco Lineament), Geophysical Journal International, 180, 1303-1312, 10.1111/j.1365-246X.2009.04485.x, 2010.
Machette, M. N., Crone, A. J., and Bowman, J. R.: Geologic investigations of the 1986 Marryat Creek, Australia, earthquake - implications for paleoseismicity in stable continental regions, USGS Bulletin, 2032-B, 29 p, 1993.
Massonnet, D., Rossi, M., Carmona, C., Adragna, F., Peltzer, G., Feigl, K., and Rabaute, T.: The displacement field of the Landers earthquake mapped by radar interferometry, Nature, 364, 138-142, 10.1038/364138a0, 1993.
Mazzotti, S., and Adams, J.: Rates and uncertainties on seismic moment and deformation in eastern Canada, Journal of Geophysical Research, 110, B09301, 2005.
McCormack, B. J.: Quaternary Fault Scarps on the North-eastern Eyre Peninsula, South Australia; Geomorphic constraints on age and faulting history by investigation of knickpoint retreat., B.Sc. (Hons), Department of Earth Sciences, University of Melbourne, Melbourne, 85 pp., 2006.
Meier, M.-A., Werner, M. J., Woessner, J., and Wiemer, S.: A search for evidence of secondary static stress triggering during the 1992 Mw7.3 Landers, California, earthquake sequence, Journal of Geophysical Research: Solid Earth, 119, 3354-3370, 10.1002/2013jb010385, 2014.

Metzger, S., Schurr, B., Ratschbacher, L., Sudhaus, H., Kufner, S.-K., Schöne, T., Zhang, Y., Perry, M., and Bendick, R.: The 2015 Mw7.2 Sarez Strike-Slip Earthquake in the Pamir Interior: Response to the Underthrusting of India's Western Promontory, Tectonics, 36, 2407-2421, 10.1002/2017tc004581, 2017.
Miles, K. R.: Tertiary faulting in northeastern Eyre Peninsula, Transactions of the Royal Society of South Australia, 75, 89-96, 1952.
Milligan, P. R., and Nakamura, A.: Total Magnetic Intensity (TMI) Image of Australia with Variable Reduction to Pole (VRTP) greyscale., Geoscience Australia dataset, http://dx.doi.org/10.4225/25/561C7CFA2F230, 2015.
Mohammadi, H., Quigley, M., Steacy, S., and Duffy, B.: Effects of source model variations on Coulomb stress analyses of a multi-fault intraplate earthquake sequence, Tectonophysics, 766, 151-166, https://doi.org/10.1016/j.tecto.2019.06.007, 2019.
Mooney, W. D., Ritsema, J., and Hwang, Y. K.: Crustal seismicity and the earthquake catalog maximum moment magnitude (Mcmax) in stable continental regions (SCRs):Correlation with the seismic velocity of the lithosphere, Earth and Planetary Science Letters, 357-358, 78-83, 2012.
Moss, R. E. S., and Ross, Z. E.: Probabilistic fault displacement hazard analysis for reverse faults, Bulletin of the Seismological Society of America, 101, 1542–1553, https://doi.org/10.1785/0120100248, 2011.
Moss, R. E. S., Stanton, K. V., and Buelna, M. I.: The impact of material stiffness on the likelihood of fault rupture propagating to the ground surface, Seismological Research Letters, 84, 485-488, 2013.
Mueller, K., and Pujol, J.: Three-Dimensional Geometry of the Reelfoot Blind Thrust: Implications for Moment Release and Earthquake Magnitude in the New Madrid Seismic Zone, Bulletin of the Seismological Society of America, 91, 1563-1573, 10.1785/0120000276 %J Bulletin of the Seismological Society of America, 2001.
Musson, R. M. W.: Interpreting intraplate tectonics for seismic hazard: a UK historical perspective, Journal of Seismology, 16, 261-273, 10.1007/s10950-011-9268-1, 2012.
Nakamura, A.: Bouguer Gravity Anomaly Grid of Onshore Australia 2016, Geoscience Australia, Canberra, Australia, http://dx.doi.org/10.4225/25/579AB36FB071A, 2016.
Okada, Y.: Surface deformation due to shear and tensile faults in a half-space, Bulletin of the Seismological Society of America, 75, 1135-1154, 1985.
Olierook, H. K. H., Timms, N. E., Merle, R. E., Jourdan, F., and Wilkes, P. G.: Paleodrainage and fault development in the southern Perth Basin, Western Australia during and after the breakup of Gondwana from 3D modelling of the Bunbury Basalt, Australian Journal of Earth Sciences, 62, 289-305, 10.1080/08120099.2015.1030774, 2015.
Pérez-Peña, J. V., Al-Awabdeh, M., Azañón, J. M., Galve, J. P., Booth-Rea, G., and Notti, D.: SwathProfiler and NProfiler: Two new ArcGIS Add-ins for the automatic extraction of swath and normalized river profiles, Computers & Geosciences, 104, 135-150, https://doi.org/10.1016/j.cageo.2016.08.008, 2017.
Peterie, S. L., Miller, R. D., Intfen, J. W., and Gonzales, J. B.: Earthquakes in Kansas Induced by Extremely Far-Field Pressure Diffusion, 45, 1395-1401, 10.1002/2017gl076334, 2018.
Polcari, M., Albano, M., Atzori, S., Bignami, C., and Stramondo, S.: The Causative Fault of the 2016 Mwp 6.1 Petermann Ranges Intraplate Earthquake (Central Australia) Retrieved by C- and L-Band InSAR Data, Remote Sensing, 10, 1311, doi:10.3390/rs10081311, 2018.
Pujol, J.: Joint Event Location — The JHD Technique and Applications to Data from Local Seismic Networks, in: Advances in Seismic Event Location, edited by: Thurber, C. H., and Rabinowitz, N., Springer Netherlands, Dordrecht, 163-204, 2000.
Quigley, M., Clark, D., and Sandiford, M.: Tectonic geomorphology of Australia, Geological Society of London Special Publication 346, 243-265, 2010.
Quigley, M. C., Cupper, M. L., and Sandiford, M.: Quaternary faults of south-central Australia: palaeoseismicity, slip rates and origin, Australian Journal of Earth Sciences, 53, 285-301, 2006.
Qureshi, I. R., and Sadig, A. A.: Earthquakes and associated faulting in central Sudan, Nature, 215, 263-265, 1967.
Rajabi, M., Heidbach, O., Tingay, M., and Reiter, K.: Prediction of the present-day stress field in the Australian continental crust using 3D geomechanical–numerical models, Australian Journal of Earth Sciences, 64, 435-454, 10.1080/08120099.2017.1294109, 2017a.
Rajabi, M., Tingay, M., Heidbach, O., Hillis, R., and Reynolds, S.: The present-day stress field of Australia, Earth-Science Reviews, 168, 165-189, 10.1016/j.earscirev.2017.04.003, 2017b.
Rajendran, C. P., Rajendran, K., and John, B.: The 1993 Killari (Latur), central India, earthquake: an example of fault reactivation in the Precambrian crust, Geology, 24, 651-654, 1996.
Rajendran, C. P., Rajendran, K., Thakkar, M., and Goyal, B.: Assessing the previous activity at the source zone of the 2001 Bhuj earthquake based on the near-source and distant paleoseismological indicators, JOURNAL OF GEOPHYSICAL RESEARCH, 113, B05311, 10.1029/2006JB004845, 2008, 2008.
Rastogi, B., Mandal, P., and Biswas, S.: Seismogenesis of earthquakes occurring in the ancient rift basin of Kachchh, Western India, in: Intraplate Earthquakes edited by: Talwani, P., Cambridge University Press, Cambridge, pp. 126-161, 2014.
Salditch, L., Stein, S., Neely, J., Spencer, B. D., Brooks, E. M., Agnon, A., and Liu, M.: Earthquake supercycles and Long-Term Fault Memory, Tectonophysics, 774, 228289, https://doi.org/10.1016/j.tecto.2019.228289, 2020.

Sandiford, M.: Neotectonics of southeastern Australia: linking the Quaternary faulting record with seismicity and in situ stress, in: Evolution and dynamics of the Australian Plate edited by: Hillis, R. R., and Muller, D., Geological Society of Australia Special Publication, 101-113, 2003a.
Sandiford, M.: Geomorphic constraints on the late Neogene tectonics of the Otway Ranges, Australian Journal of Earth Sciences, 50, 69-80, 2003b.
Sandiford, M., and Egholm, D. L.: Enhanced intraplate seismicity along continental margins: Some causes and consequences, Tectonophysics, 457, 197-208, 2008.
Sandiford, M., Quigley, M., de Broekert, P., and Jakica, S.: Tectonic framework for the Cainozoic cratonic basins of Australia, Australian Journal of Earth Sciences, 56, s5-s18, 2009.
Sandiford, M., and Quigley, M. C.: Topo-Oz: insights into the various modes of intraplate deformation in the Australian continent, Tectonophysics, 474, 405-416, 2009.
Satyabala, S. P.: Coseismic ground deformation due to an intraplate earthquake using synthetic aperture radar interferometry: The Mw6.1 Killari, India, earthquake of 29 September 1993, 111, 10.1029/2004jb003434, 2006.
Schmidt, D. A., and Bürgmann, R.: InSAR constraints on the source parameters of the 2001 Bhuj earthquake, Geophysical Research Letters, 33, 10.1029/2005gl025109, 2006.
Schulte, S. M., and Mooney, W. D.: An updated global earthquake catalogue for stable continental regions: reassessing the correlation with ancient rifts, Geophysical Journal International, 161, 707-721, 2005.
Scott, C., Champenois, J., Klinger, Y., Nissen, E., Maruyama, T., Chiba, T., and Arrowsmith, R.: The 2016 M7 Kumamoto, Japan, Earthquake Slip Field Derived From a Joint Inversion of Differential Lidar Topography, Optical Correlation, and InSAR Surface Displacements, 46, 6341-6351, 10.1029/2019gl082202, 2019.
Seeber, L., Jain, S. K., Murty, C. V. R., and Chandak, N.: Surface rupture and damage patterns in the Ms = 6.4, September 29, 1993 Killari (Latur) earthquake in central India, National Centre for Earthquake Engineering Research Bulletin, 7, 12, 1993.
Seeber, L., Ekstrom, G., Jain, S. K., Murty, C. V. R., Chandak, N., and Armbruster, J. G.: The 1993 Killari earthquake in central India: A new fault in Mesozoic basalt flows?, Journal of Geophysical Research, 101, 8543-8560, 1996.
Senior, B. R., Truswel, E. M., ldnurm, F. M., Shaw, R. D., and Warren, R. G.: Cainozoic sedimentary basins in the eastern Arunta Block, Alice Springs region, central Australia, AGSO Journal of Australian Geology and Geophysics, 15, 421-444, 1995.
Sibson, R. H., Healy, D., Butler, R. W. H., Shipton, Z. K., and Sibson, R. H.: Reverse fault rupturing: competition between non-optimal and optimal fault orientations, in: Faulting, Fracturing and Igneous Intrusion in the Earth's Crust, Geological Society of London, 0, 2012.
Skoumal, R. J., Brudzinski, M. R., and Currie, B. S.: Earthquakes Induced by Hydraulic Fracturing in Poland Township, Ohio Bulletin of the Seismological Society of America 105, 189-197, doi:10.1785/0120140168 2015.
Smith, M. G.: Hydrogeology of the Lake Muir–Unicup Catchment, Western Australia: an ecologically important area experiencing hydrologic change, Ph.D., Department of Applied Geology, Curtin University, 2010.
Spaggiari, C. V., Bodorkos, S., Barquero-Molina, M., Tyler, I. M., and Wingate, M. T. D.: Interpreted bedrock geology of the south Yilgarn and central Albany-Fraser orogen, Western Australia, Geological survey of Western Australia, Record, 2009/10, 84pp, 2009.
Špičák, A.: Earthquake Swarms and Accompanying Phenomena in Intraplate Regions: A Review, Studia Geophysica et Geodaetica, 44, 89-106, 10.1023/A:1022146422444, 2000.
Steacy, S., Jiménez, A., and Holden, C.: Stress triggering and the Canterbury earthquake sequence, Geophysical Journal International, 196, 473-480, 10.1093/gji/ggt380 %J Geophysical Journal International, 2013.
Stein, S.: Approaches to continental intraplate earthquake issues, Special Paper - Geological Society of America, 425, 1-16, 10.1130/2007.2425(01), 2007.
Stone, J., Allan, G., and Fifield, L. K.: Limestone erosion measurements with cosmogenic Cl-36 in Calcite - preliminary results from Australia, Nuclear instruments and methods in physics research, section B - beam interactions with materials and atoms, 92, 311-316, 1994.
Talwani, P.: The intersection model for intraplate earthquakes, Seismological Research Letters, 59, 305- 310, 1988.
Talwani, P.: Chapter 11. Unified model for intraplate earthquakes, in: Intraplate Earthquakes, edited by: Talwani, P., Cambridge University Press, United Kingdom, 275-302, 2014.
Toda, S., Stein, R. S., Richards-Dinger, K., and Bozkurt, S. B.: Forecasting the evolution of seismicity in southern California: Animations built on earthquake stress transfer, 110, 10.1029/2004jb003415, 2005.
Tonkin, T. N., and Midgley, N. G.: Ground-Control Networks for Image Based Surface Reconstruction: An Investigation of Optimum Survey Designs Using UAV Derived Imagery and Structure-from-Motion Photogrammetry, Remote Sensing, 8, 1–8, 2016.
Townend, J., and Zoback, M. D.: How faulting keeps the crust strong, Geology, 28, 399-402, 2000.
Tregonning, P.: Is the Australian Plate deforming? A space geodetic perspective., Geolical Society of Australia Special Publication, 22 and Geological Society of America Special Publication, 372, 41-48, 2003.
Valentine, A. P., and Trampert, J.: Assessing the uncertainties on seismic source parameters: Towards realistic error estimates for centroid-moment-tensor determinations, Physics of the Earth and Planetary Interiors, 210-211, 36-49, https://doi.org/10.1016/j.pepi.2012.08.003, 2012.

van Arsdale, R.: Displacement history and slip rate on the Reelfoot fault of the New Madrid seismic zone, Engineering Geology, 55, 219-226, 2000.
Waldhauser, F., and Ellsworth, W. L.: A Double-Difference Earthquake Location Algorithm: Method and Application to the Northern Hayward Fault, California, Bulletin of the Seismological Society of America, 90, 1353-1368, 10.1785/0120000006 %J Bulletin of the Seismological Society of America, 2000.
Wallace, M. W., Dickinson, J. A., Moore, D. H., and Sandiford, M.: Late Neogene strandlines of southern Victoria: a unique record of eustasy and tectonics in southeast Australia, Australian Journal of Earth Sciences, 52, 279-297, 2005.
Wang, S., Xu, W., Xu, C., Yin, Z., Burgmann, R., Liu, L., and Jiang, G.: Changes in Groundwater Level Possibly Encourage Shallow Earthquakes in Central Australia: The 2016 Petermann Ranges Earthquake, Geophysical Research Letters, 46, https://doi.org/10.1029/2018GL080510, 2019.
Weatherman, M.: Basement Control on Distribution of Active Faults on North-eastern Eyre Peninsula, and some seismic implications, B. Sc. (Hons), School of Earth Sciences, The University of Melbourne, Melbourne, 77 pp., 2006.
Weber, B., Becker, J., Hanka, W., Heinloo, A., Hoffmann, M., Kraft, T., Pahlke, D., Reinhardt, J., Saul, J., and Thoms, H.: SeisComP3 - automatic and interactive real time data processing, Geophysical Research Abstracts, 9, 09219, SRef-ID: 1607-7962/gra/EGU2007-A-09219, 2007.
Wegmüller, U., and Werner, C.: GAMMA SAR processor and interferometry software, 3rd ERS Scientific Symposium Florence, 1997.
Wells, D. L., and Coppersmith, K. J.: New empirical relationships among magnitude, rupture length, rupture width, rupture area, and surface displacement, Bulletin of the Seismological Society of America, 84, 974-1002, 1994.
Wheeler, R. L.: Quaternary tectonic faulting in the Eastern United States, Engineering Geology, 82, 165-186, 2006.
White, S., Stollhofen, H., Stanistreet, I. G., and Lorenz, V.: Pleistocene to Recent rejuvenation of the Hebron Fault, SW Namibia, 316, 293-317, 10.1144/SP316.18 %J Geological Society, London, Special Publications, 2009.
Wilde, S. A., and Walker, I. W.: Pemberton - Irwin Inlet (SI/50-10, SI/50-14) 1:250 000 scale geological series map, Geological Survey of Western Australia, 1984.
Wilde, S. A., Middleton, M. F., and Evans, B. J.: Terrane accretion in the southwest Yilgarn craton: evidence from a deep seismic crustal profile, Precambrian Research, 78, 179-196, 1996.
Williams, R.: DEMs of difference, Geomorphological Techniques, 2, 2012.
Yabe, S., and Ide, S.: Why Do Aftershocks Occur Within the Rupture Area of a Large Earthquake?, Geophysical Research Letters, 45, 4780-4787, 10.1029/2018gl077843, 2018.
Yarwood, D. R., and Doser, D. I.: Deflection of oceanic transform motion at a continental margin as deduced from waveform inversion of the 1939 Accra, Ghana earthquake, Tectonophysics, 172, 341-349, 1990.
Zellman, M. S., and Ostenaa, D.: Geophysical and Paleoseismic Investigation of the Cheraw Fault, Southeastern Colorado, 54, 2016.
Zhou, Y., Parsons, B. E., and Walker, R. T.: Characterizing Complex Surface Ruptures in the 2013 Mw 7.7 Balochistan Earthquake Using Three-Dimensional Displacements, 123, 10,191-110,211, 10.1029/2018jb016043, 2018.

Tables

Event (setting) e=extended, n = non-extended, b = lithospheric boundary	Year	Magnitude (Mw)	Mapped surface rupture length (km)#	Mechanism	Max vertical surface displacement (m)	Deformation Reference
Reelfoot Thrust, USA (e)	1812	7.2-7.3	blind (61)	R	~2	Mueller & Pujol (2001)
Kutch, India (e)	1819	7.25-8.25	blind (>90)	R	7-9	Rajendran *et al.* (2008)
Accra, Africa (e)	1939	6.5	9-17	SS	0.46	Bates (1941); Yarwood and Doser (1990)
The Sudan, Africa (e)	1956	5.1	6	SS	0	Qureshi and Sadig (1967)
Meckering, WA (n)	1968	6.58	37	R	2.5	Gordon & Lewis (1980); Clark & Edwards (2018)
Calingiri, WA (n)	1970	5.46	3.3	R	0.4	Gordon & Lewis (1980)
Cadoux, WA (n)	1979	6.13	14	R	1.4	Lewis *et al.* (1981)
Guinea, Africa (e)	1983	6.2	9.4	SS	0.13	Langer *et al.* (1987)
Marryat Creek, SA (n)	1986	5.74	13	R	0.9	Machette *et al.* (1993)
Tennant Creek, NT* (n)	1988	6.76	36	R	1.8	Crone e*t al.* (1992, 1997)
Ungava, Canada* (n)	1989	6.3	8.5	R	0.8	Bent (1994)
Killari, India (n)	1993	6.1	3 (7-15)	R	0.5	Rajendran et al. (1996); Satyabala (2006)
Bhuj, India (e)	2001	7.7	blind (60)	R	3.0	Schmidt and Burgmann (2006); Rajendran *et al.* (2008)
Kallanie (n)	2005	4.4	blind	R	0.027	Dawson *et al.* (2008)
Hatanbulag, Mongolia (n,b)	2005	5.2	blind	R	0.01	Amarjargal *et al.* (2013)
Katanning, WA (n)	2007	4.73	0.2 (1.26)	R	0.1	Dawson *et al.* (2008)
Ernabella, SA (n,b)	2012	5.37	1.5	R	0.5	Clark *et al.* (2014b)

Petermann Ranges, NT (n,b)	2016	6.10	15 (20)	R	1.0	King *et al.* (2018); Polcari et al. (2018); Wang et al. (2019)
Botswana, Africa (n,b)	2017	6.5	blind	N	0.04	Gardonio et al. (2018)
Lake Muir, WA (n,b)	2018	5.30	3.2 (7)	R	0.4	this article
Lake Muir , WA (n,b)	2018	5.20	Blind (4)	SS	0	this article
Tennant Creek (n)	2019	5.3	Blind	R	0.04	https://twitter.com/sotisvalkan/status/1158362851930726400
Montelimar, France (e)	2019	4.9	<1?(5)	R	0.08	https://twitter.com/sotisvalkan/status/1194539703858606080

Table 1: Historical earthquake events known to have produced surface rupture in stable continental region crust (expanded after Crone et al., 1997; Clark et al., 2014b). * The Ungava surface rupture formed as the result of two events 0.9 sec apart (Bent, 1994), and Tennant Creek surface rupture was produced by three events in a 12 hr period (Bowman, 1992). # values in brackets estimate the surface rupture length from surface deformation (e.g. InSAR data). Shaded cells are events for which an InSAR image was produced.

Date (UTC)	Latitude	Longitude	Max horiz uncert. (km)	Depth (km)	Depth ~~uncertainty~~ uncert. (km)	M_W	M_L	Event page (USGS = moment tensors)
16/09/2018	-34.4102~~-34.3897~~	116.7792~~116.7988~~	1.19	~~0.02~~1.72	1.92	5.32	5.71	https://earthquakes.ga.gov.au/event/ga2018sfzeme https://earthquake.usgs.gov/earthquakes/eventpage/us2000hfcw
~~13~~12/10/2018	-34.3953~~-34.39523~~	116.7988~~116.79883~~	0.88	5.77	1.90		4.6~~5~~	https://earthquakes.ga.gov.au/event/ga2018ucpciy
~~98~~/11/2018	-34.4347~~-34.42316~~	116.7704~~116.78733~~	1.05	3.02	1.46	5.19	5.40	https://earthquakes.ga.gov.au/event/ga2018wamvnf https://earthquake.usgs.gov/earthquakes/eventpage/us1000hpej

Table 2: Selected source parameters and ~~recourse~~ resource links for the three largest events in the Lake Muir earthquake sequence.

~~Regression*~~	~~*a*~~	~~*a (std err)*~~	~~*b*~~	~~*b (std err)*~~	~~Std~~
~~*VSRL* (LSQ)~~	~~-5.38~~	~~0.788~~	~~1.064~~	~~0.135~~	~~0.250~~
~~*VSRL* (ODR)~~	~~-5.76~~	~~0.815~~	~~1.130~~	~~0.140~~	~~0.169~~
~~*DSRL* (LSQ)~~	~~-3.58~~	~~0.733~~	~~0.777~~	~~0.126~~	~~0.233~~
~~*DSRL* (ODR)~~	~~-3.91~~	~~0.753~~	~~0.833~~	~~0.129~~	~~0.181~~
~~*DSRL'* (LSQ)~~	~~-2.97~~	~~0.480~~	~~0.693~~	~~0.082~~	~~0.152~~
~~*DSRL'* (ODR)~~	~~-3.10~~	~~0.485~~	~~0.716~~	~~0.083~~	~~0.125~~

~~**Table 3. Coefficients between *SRL* (*VSRL* or *DSRL* in km) and M_W for substitution into Equation 1. * the regression type used is either least squares (LSQ) or orthogonal distance (ODR) regression, respectively.**~~

Figure Captions

Figure 1: An example of heterogeneity in seismogenic potential within Stable Continental Region (SCR) crust from Australia. ~~Neotectonic features (red lines) from the Australian Neotectonic Features Database~~ (Clark et al., 2012; Clark, 2012)~~. Historical surface ruptures shown as red dots labelled with the year of the event.~~ Base map shows neotectonic superdomains (after Leonard et al., 2014), and the outlines of Australian States and Territories. Neotectonic features (red lines) from the Australian Neotectonic Features Database (Clark et al., 2012; Clark, 2012). Historical surface ruptures shown as red dots labelled with the year of the event. Note all historical surface ruptures have occurred in Precambrian non-extended stable continental region (SCR, Johnston et al., 1994) crust. a = Roopena scarp, b = Hyden scarp, c = Lort River scarp, d = Dumbleyung scarp~~, e = Cadell scarp~~.

Figure 2: Location and geological setting of the 2018 Lake Muir earthquake sequence in southwest Western Australia**.** ~~Location i~~**Inset shows** Precambrian **basement geology**, and overlying Phanerozoic Perth Basin and Eocene rocks ~~modified after the GSWA 1:500 000 State interpreted bedrock geology of Western Australia, 2016~~ **(modified after Geological Survey of Western Australia, 2016). Proterozoic and younger faults and dykes are shown as thick and thin black lines respectively. Base map in the main frame shows reduced to pole total magnetic intensity data (Milligan and Nakamura, 2015). Black triangles show the locations of seismic recording stations** (rapid deployment kits are prefixed with LM)**, and GPS stations (SWSZ prefix). The location of the** ~~September~~ two M>5 **earthquake** epicentres ~~is~~ are **shown by** ~~a~~ **white star**s, with arrows indicting the associated focal mechanisms~~, with its associated uncertainty ellipse~~ **(see Table 2 for source).** ~~The uncertainty calculated for the location of this event is significantly larger than subsequent events in the sequence as it relied exclusively on the sparse national network of seismic stations. S~~The s**urface rupture**~~s~~ trace **from the September** event **and** the surface deformation front from the **November event**~~s~~ **are shown by black solid and dashes lines, respectively (see text for details).** ~~Focal mechanisms are shown for the two M>5 events (see Table 2 for source).~~ The InSAR phase image for the September M_W 5.3 earthquake is overlain to demonstrate the scale of surface deformation.

Figure 3: Map of the Lake Muir surface ruptures and associated seismicity. Background map is part of the Western Australian Department of Biodiversity, Conservation and Attractions LiDaR holdings (https://www.dbca.wa.gov.au/contact-us) with ESRI world imagery overlain at 75% transparency. White line shows the extent of the discrete surface rupture relating to the September event, as mapped from InSAR. Superposed black lines are scarp segments mapped on the ground. Grey dashed line shows the discrete line of deformation relating to the November event, as mapped from InSAR. The three largest events and their uncertainty ellipses**, 16th September M_W5.3,** ~~13th~~ 12th **October M_L4.6, and** ~~9th~~ 8th **November M_W5.2, are consecutively** ~~labelled~~numbered (see Table 2)**.**

Figure 4: Photographs of the surface rupture: (a) 13 cm high scarp crossing farm track. Photo taken by Roger Hearn on 27/09/2018. Looking north (479101 mE, 6190727 mN); (b) east-trending tension fissures relating to lateral spread into a farm dam (479588 mE, 6192126 mN); (c) 40 cm high scarp and hanging wall tension fissure at the hand trench location (see Figure 5). Looking north (479285 ME, 6191496 mN); (d) 40 cm high scarp in pine plantation. Looking northeast (479112 mE, 6190422 mN). GD94/MGA50.

Figure 5: Hand trench location (479285 ME, 6191496 mN GDA94/MGA50). (a) subset of the photogrammetrically-derived UAV DTM (see Figure 3 for full footprint), with topographic section indicated by the black line. Colour drape has been tilted to remove

regional topographic slope and enhance relative differences; (b) photomosaic of the north wall of the hand trench showing folded and displaced strata; and (c) interpretation of stratigraphy and structure of the north wall of the hand trench.

Figure 6: Phase images and images of the unwrapped InSAR line of sight (LOS) displacement field for the (a) & (b) September M_W 5.3 and (c) & (d) November M_W5.2 events. The location of the surface rupture relating to the September event is shown as a white line, with a black dashed line showing where the scarp was observed in the field. The surface deformation front relating to the November event is shown as a dashed black line. Refer to Figure 2 for focal mechanisms. Seismicity before and after the November event is shown black dots on parts (a) & (b) and (c) & (d), respectively. The main shocks are shown as red stars. Each fringe in (a) and (c) represents 2.8 cm of LOS range change. Note several unwrapping errors are evident as regions bound by a step jump at the northern and southern end of the scarp in part (b). The north-south extent of an easterly trending band of pine forest associated with degradation of coherence is indicated with a white arrow in part (a).

Figure 7: Relative co-seismic displacement swath profiles through UAV and InSAR data; (a) Location of scarp parallel and perpendicular swath profiles. Mapped scarp elements are shown in red. Length-weighted rose diagrams (north up) show orientation of scarp elements. The extent of the UAV surveys are shown as black outlines. UAV DTM differenced against LiDAR is shown over main scarp segment (blues are small, greys are large). Location and uncertainty ellipse for the September M_W5.3 event is shown with a star and red dashed line, respectively. Base map is the InSAR phase image for the September event over LiDaR (datum/projection = GDA94/MGA50); (b) Scarp-parallel profiles. UAV profiles sample a 100 m wide swath centred on the profile line and plot relative vertical displacement. The 90th percentile minus the 10th percentile value elevation value is plotted to reduce noise in the UAV data resulting from the difficulty in removing low vegetation inherent to structure from motion DTMs. UAV 2-D profiles plot the vertical displacement measured from single profile lines through small area UAV DTMs flown along forest trails. Spot heights were measured visually with a tape measure where the forest was too dense for other techniques to be used. InSAR swath profiles are co-located with the UAV profile lines and sample 300 m either side of the profile line. These plot relative LOS displacement, calculated as the difference between the maximum and the minimum value in each scarp-perpendicular swath. (c) 1st to 3rd quartile range of a scarp-perpendicular swath profile through the UAV data is plotted along with the mean value to demonstrate the precision of the UAV data. Variation in LOS displacement for the co-located unwrapped InSAR profile is not resolvable at the scale of the figure, so the maximum value sampled by each scarp-parallel swath is plotted. Zero relative displacement is arbitrarily pinned to the eastern end of the profile in part.

Figure 8: Coulomb stress changes resulting from the September M_W 5.3 event (plan at 3 km depth and section), (a) resolved for reverse faults parallel to the November rupture plain, and (b) resolved for optimally oriented strike slip faults. The rupture area was modelled as being 5.0 km long by ~~2.0~~1.17 km wide to constrain seismic moment and slip, and ~~30~~50° east-dipping consistent with the USGS focal mechanism for the event (Figure 2, Table 2,). Relocated seismicity prior to the November main shock is overlain onto the plan and projected onto the vertical A-B section plane (see Figure 3 for seismicity legend). Black line is the surface deformation trace interpreted from ground observations and InSAR data. Black arrows in the upper panel ~~show a linear trend of epicentres hypocentres~~point to the position of the ~~that relate to the~~ November M_W 5.3 strike-slip event rupture plane.

Figures

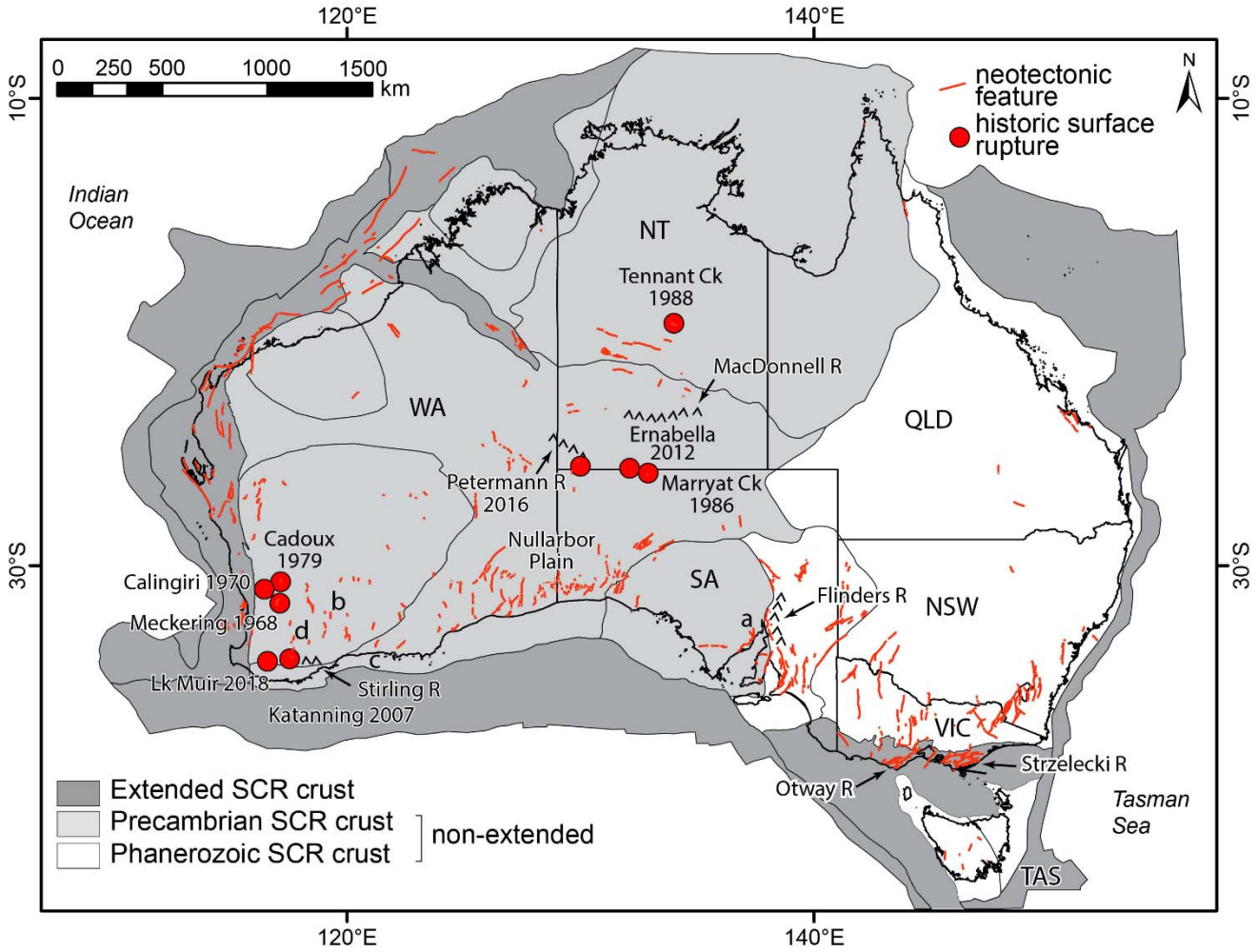

1590 **Figure 1**

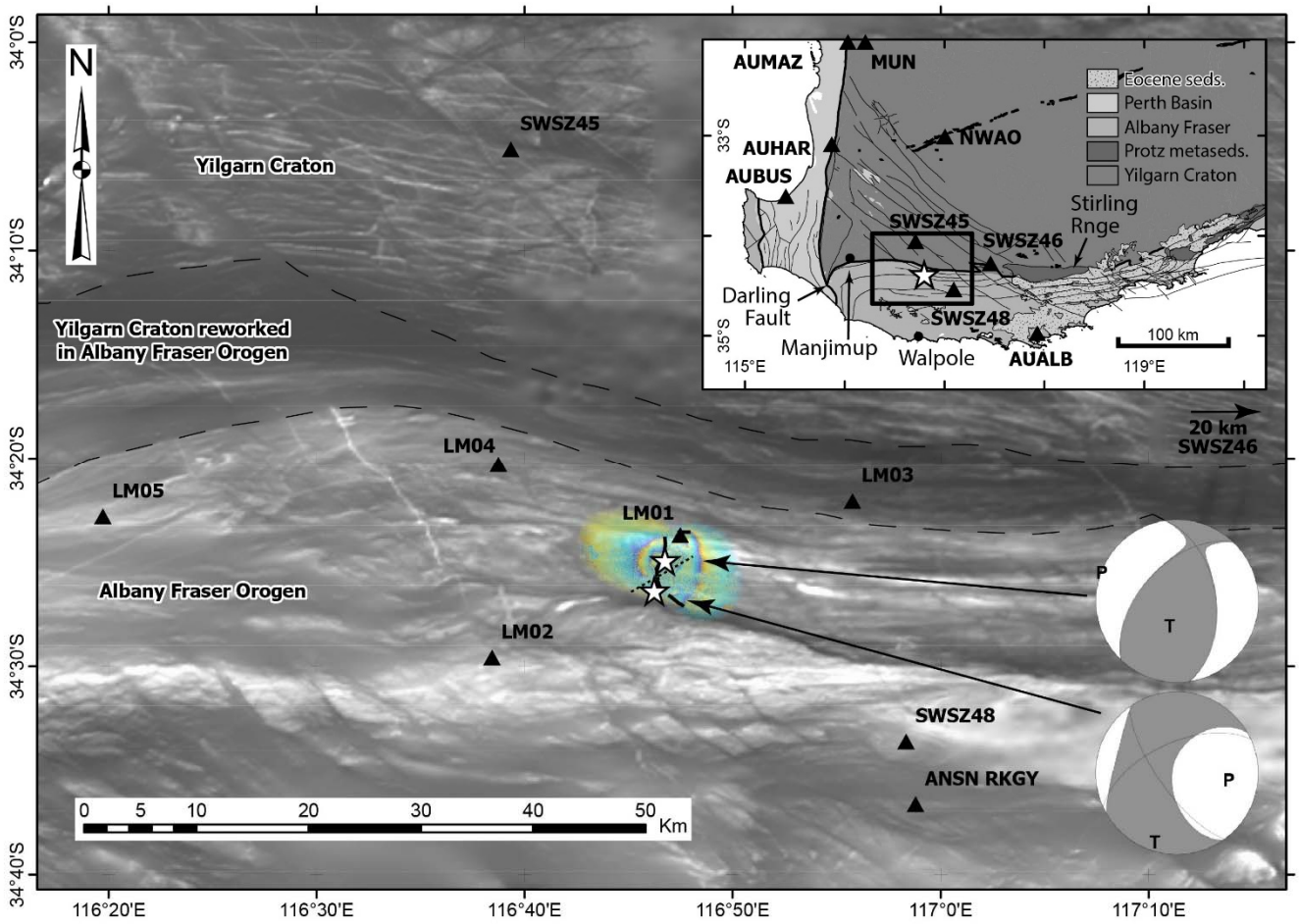
N
SWSZ45
Yilgarn Craton
Yilgarn Craton reworked
in Albany Fraser Orogen
Albany Fraser Orogen
LM01
LM02
LM03
LM04
LM05
SWSZ48
ANSN RKGY
0 5 10 20 30 40 50 Km
34°0'S
34°10'S
34°20'S
34°30'S
34°40'S
116°20'E
116°30'E
116°40'E
116°50'E
117°0'E
117°10'E
AUMAZ
MUN
AUHAR
NWAO
AUBUS
SWSZ45
SWSZ46
SWSZ48
Stirling
Rnge
Darling
Fault
Manjimup
Walpole
AUALB
33°S
35°S
115°E
119°E
100 km
Eocene seds.
Perth Basin
Albany Fraser
Protz metaseds.
Yilgarn Craton
20 km
SWSZ46
P
T
P
T

Figure 2

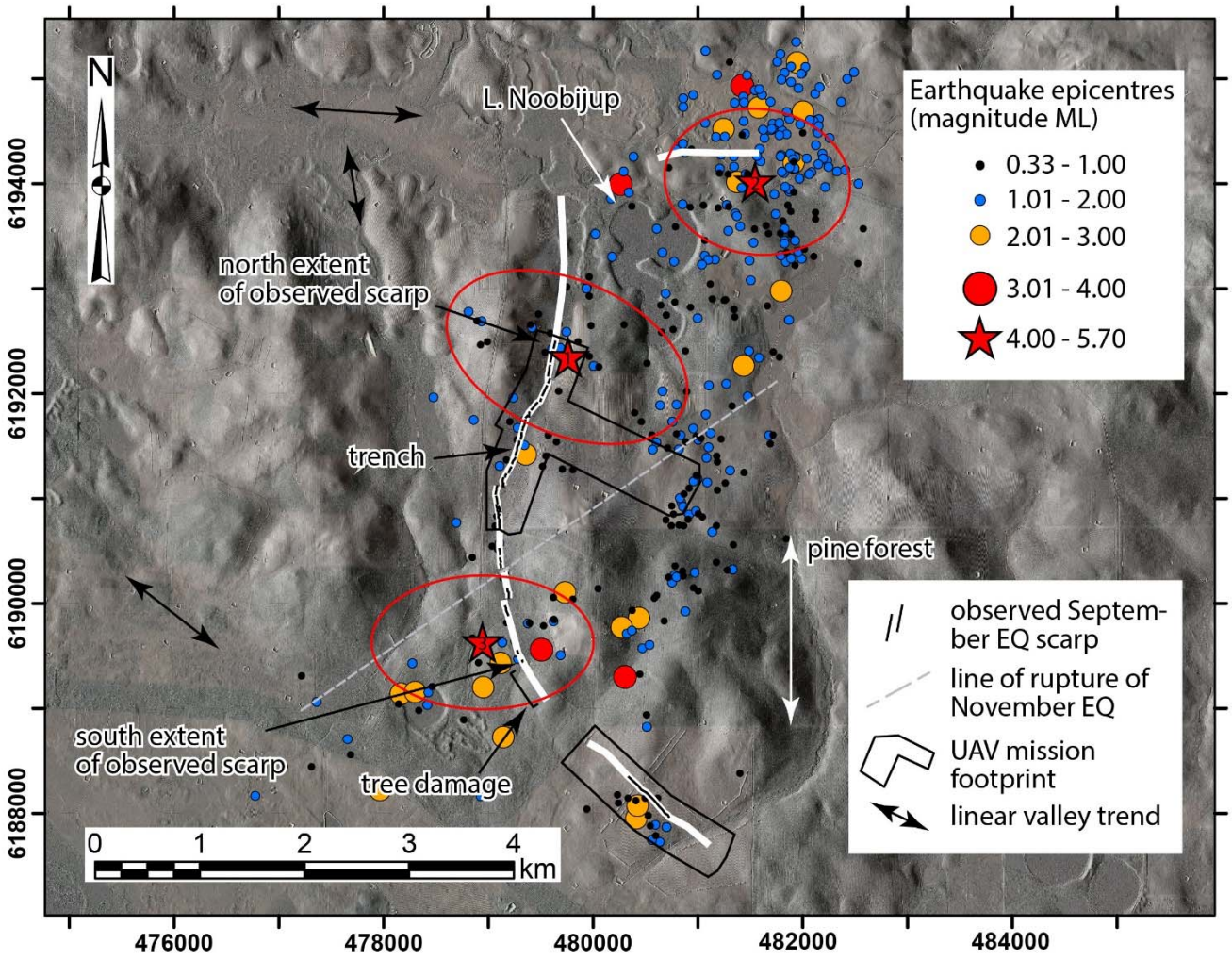
N
L. Noobijup
north extent
of observed scarp
trench
pine forest
south extent
of observed scarp
tree damage
0 1 2 3 4
km
Earthquake epicentres
(magnitude ML)
0.33 - 1.00
1.01 - 2.00
2.01 - 3.00
3.01 - 4.00
4.00 - 5.70
observed Septem-
ber EQ scarp
line of rupture of
November EQ
UAV mission
footprint
linear valley trend
6194000
6192000
6190000
6188000
476000
478000
480000
482000
484000

Figure 3

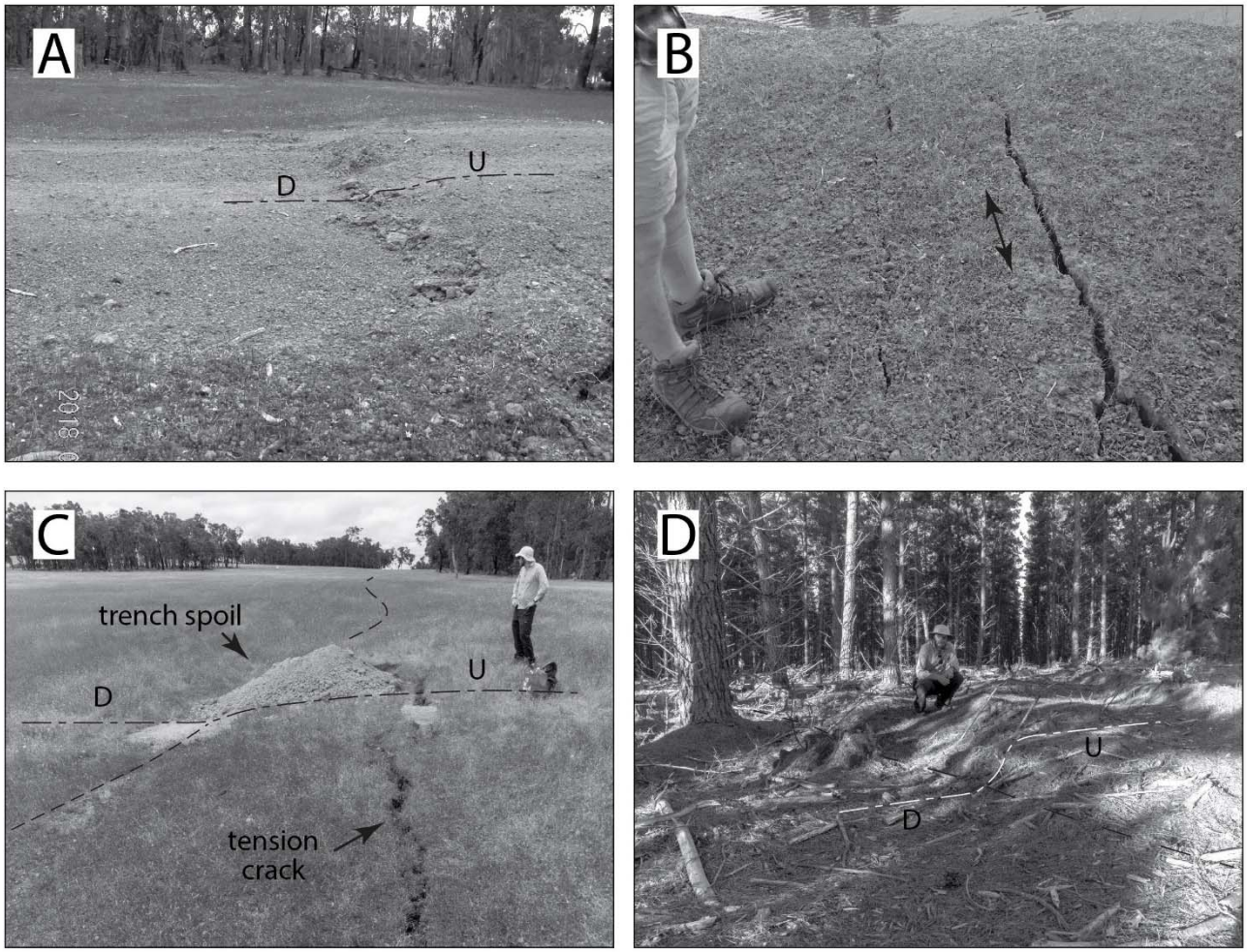

1595

Figure 4

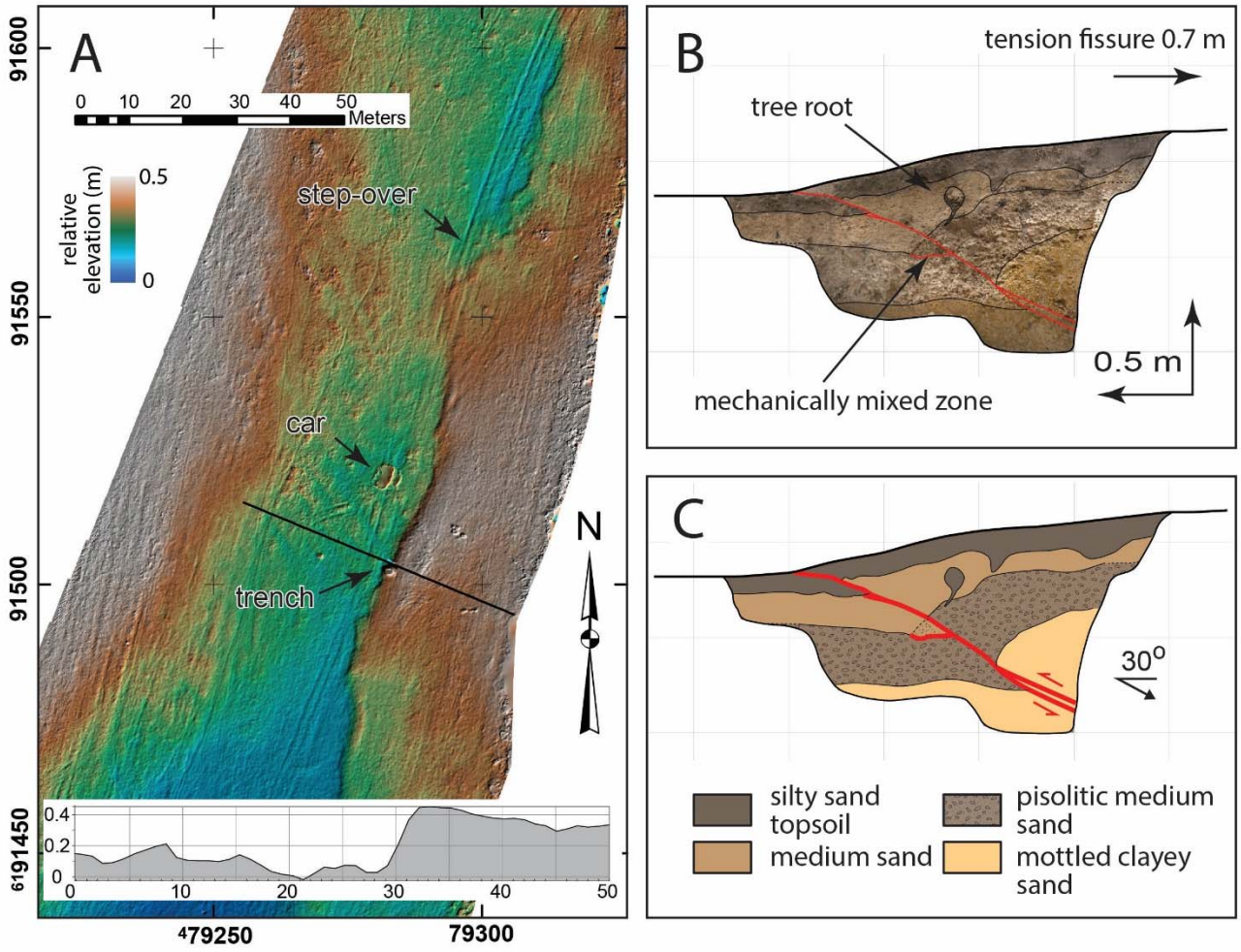
A
0 10 20 30 40 50
Meters
relative elevation (m)
0.5
0
step-over
car
trench
N
91600
91550
91500
6191450
0.4
0.2
0
0 10 20 30 40 50
479250
79300
B
tension fissure 0.7 m
tree root
mechanically mixed zone
0.5 m
C
30°
silty sand topsoil
medium sand
pisolitic medium sand
mottled clayey sand

Figure 5

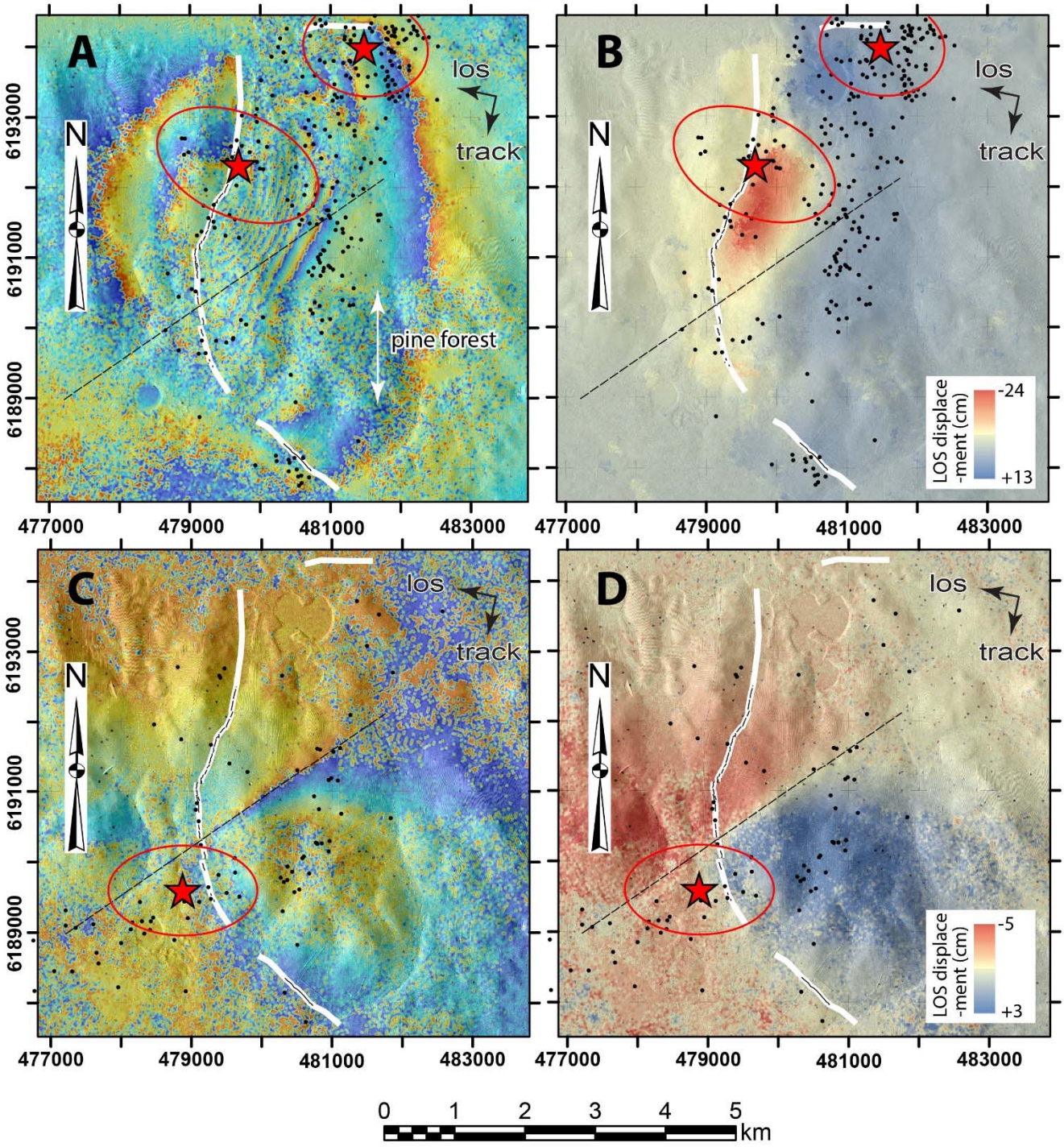

1600 **Figure 6**

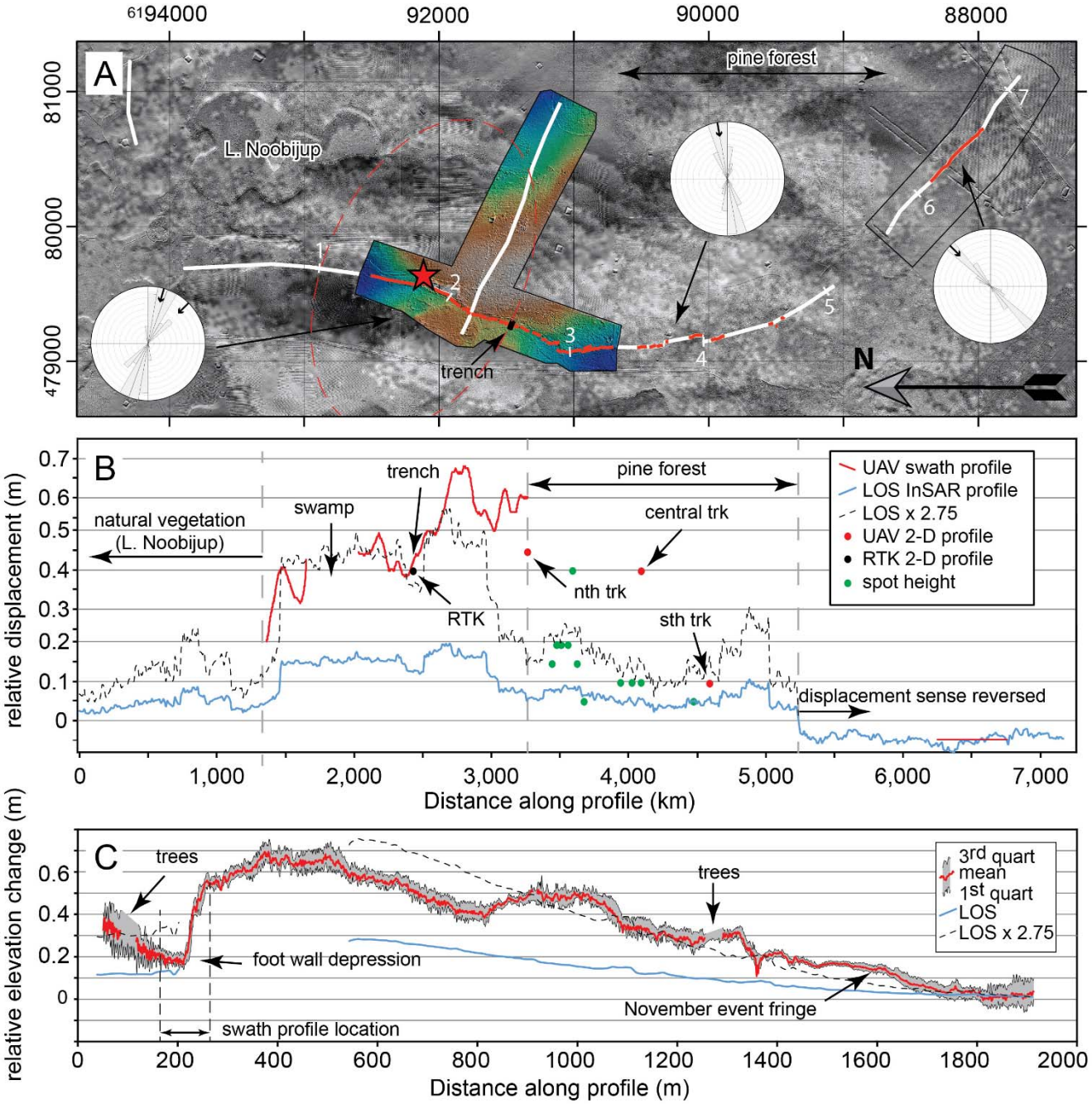
A
6194000
92000
90000
88000
81000
80000
479000
L. Noobijup
pine forest
trench
N
1
2
3
4
5
6
7
B
relative displacement (m)
natural vegetation
(L. Noobijup)
swamp
trench
RTK
pine forest
central trk
nth trk
sth trk
displacement sense reversed
UAV swath profile
LOS InSAR profile
LOS x 2.75
UAV 2-D profile
RTK 2-D profile
spot height
Distance along profile (km)
C
relative elevation change (m)
trees
foot wall depression
swath profile location
trees
November event fringe
3rd quart
mean
1st quart
LOS
LOS x 2.75
Distance along profile (m)

Figure 7

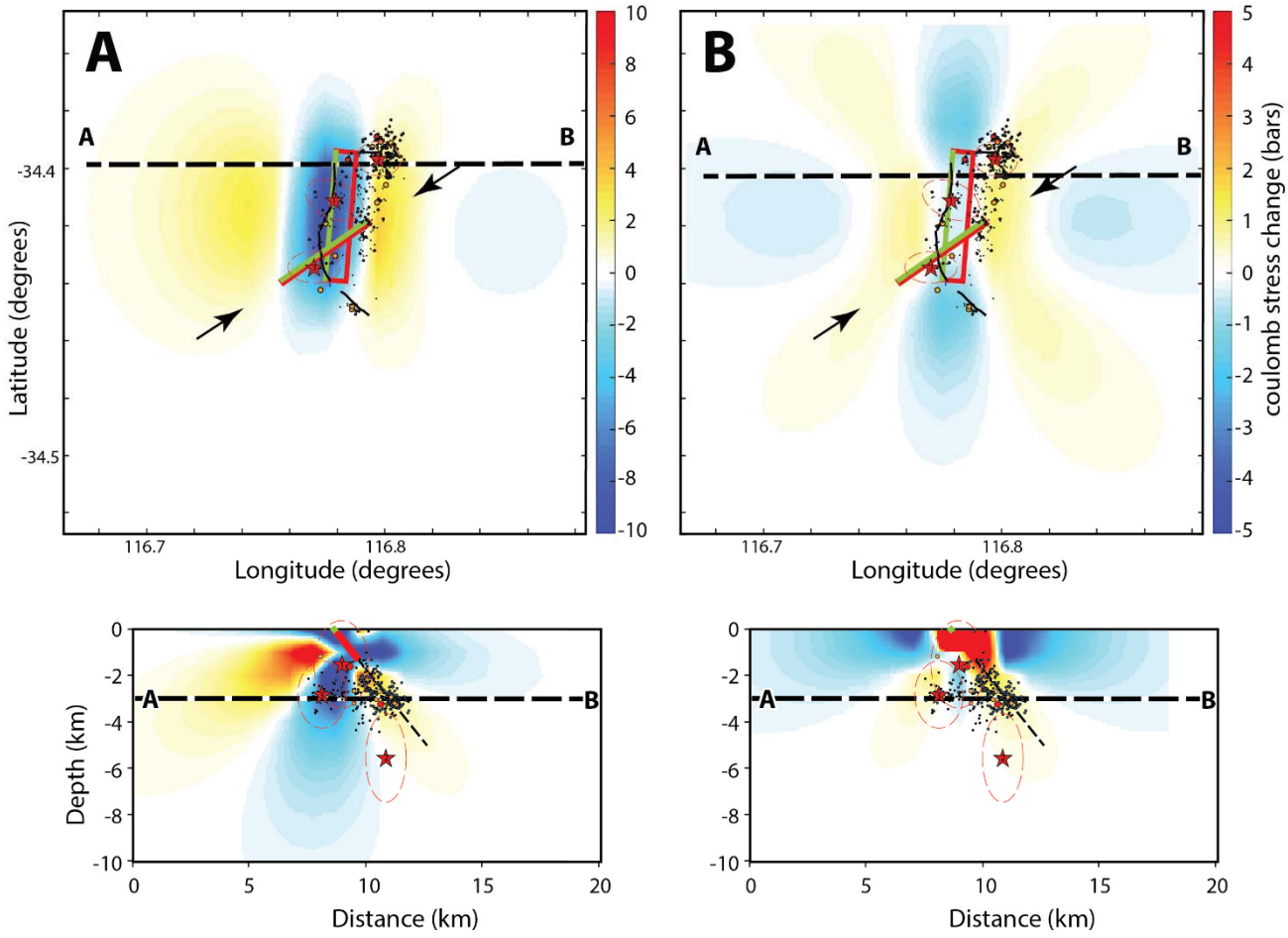
A
B
A
B
-34.4
-34.5
Latitude (degrees)
116.7
116.8
Longitude (degrees)
10
8
6
4
2
0
-2
-4
-6
-8
-10
5
4
3
2
1
0
-1
-2
-3
-4
-5
coulomb stress change (bars)
Depth (km)
0
-2
-4
-6
-8
-10
0
5
10
15
20
Distance (km)

Figure 8

Supplementary information

~~1~~ UAV DTM processing workflow and DBCA LiDaR details

In order to recover the surface deformation envelope associated with the events, aerial photographs were acquired with a DJI Phantom 4 UAV in an approximately 500 m-wide swath along an approximately 2 km length of the scarp produced in the September event. A ~2 km-long cross-line was also flown, extending eastward from the scarp across the region of most significant surface deformation indicated in the InSAR data (Figure 3). Flights were planned in the Map Pilot software (version 3.0.0) provided by Drones Made Easy (https://support.dronesmadeeasy.com/hc/en-us/categories/200739936-Map-Pilot-for-DJI). The 1144 images were captured in RAW format from an average elevation above the take-off point of 100 m, with 75% overlap in the forward and sideward directions, achieving an effective ground sampling distance of ~5.25 cm. Seventeen ground control points (GCPs) were deployed within the 1.75 km^2 mission area, and their locations were surveyed to better than 0.03 m accuracy in the horizontal and 0.06 m accuracy in the vertical using an Altus RTK GPS system. Due to the size of the area being captured, the coverage was acquired over two days.

The image dataset was processed using a Structure-from-Motion (SfM) and multi-view stereo approach, implemented in the software Agisoft Photoscan Pro 1.4.3 (Agisoft LCC). Initial image alignment and production of a sparse point cloud was achieved using the approximate 3D position, roll, pitch and yaw of the UAV captured by the UAV's on-board GPS and an inertial measurement unit. The GCPs were then manually identified on the images and their co-ordinates imported. The co-ordinates of the GCPs were used to refine the camera calibration parameters, and to optimise the geometry of the sparse point cloud. Multi-view stereo image matching algorithms (Seitz et al., 2006), implemented in Agisoft Photoscan Pro 1.4.3, were then applied to densify the sparse point cloud. The resulting dense point cloud achieved a standard deviation of the location differences between it and the control points of 0.09 m in the horizontal and 0.01 m in the vertical, which is comparable to other studies using similar GCP densities (e.g. Gindraux et al., 2017). Several studies of factors impacting local photogrammetry-derived DSM accuracy (e.g. Tonkin and Midgley, 2016; Gindraux et al., 2017) report a vertical accuracy decrease of ~0.1 m for every 100 m increase in the distance to the closest GCP. In extreme cases this can result in a 'bowl' or 'dome' effect (e.g. Ouédraogo et al., 2014). In our study the maximum distance from a control point is in the order of 200-300 m.

The dense point cloud was exported to the American Society for Photogrammetry and Remote Sensing (ASPRS) LAS format and classified into ground and non-ground points using the Cloth Simulation Filtering algorithm (Zhang et al., 2016; Serifoglu Yilmaz et al., 2018) implemented in the open source software package CloudCompare (https://www.danielgm.net/cc/). Points comprising the ground class were then re-imported into Photoscan, and a 6 cm-resolution Digital Terrain Model (DTM) was

generated. The DTM was used within the software to produce an orthophoto, then exported to geotiff format for further analysis.

In January 2012, the Western Australia Government Department of Biodiversity, Conservation and Attractions (DBCA) acquired a 1 m gridded LiDAR DTM covering the study area. The average magnitude of the uncertainties associated with the elevation values for this dataset is reported as 0.063±0.074 m. The elevation values from a subset of the LiDAR were subtracted from the ground class DTM generated in this study, to produce a DTM of difference (DoD, Williams, 2012). Voids in the DoD were filled using the ESRI ArcGIS *focal statistics tool* (null values are filled with the mean value within a rectangular neighbourhood of 50 cells dimension).

Change in land use from forestry to pasture in the time between acquisition of the LiDAR and UAV datasets has resulted in the introduction of several artefacts into the differenced DEM. For example, forestry practice involved the construction of numerous parallel furrows up to 0.1 – 0.2 m high and at 3 – 4 m spacing, into which pine trees were planted. The relief on these furrows has significantly eroded in the 6.5 years between the acquisition of the datasets. Several dams have also been constructed, one of which resulted in the modification of a wetland. Despite these sources of 'cultural noise', the vertical displacement envelope resulting from the September earthquake was able to be recovered from the DoD, with an accuracy of approximately 0.1 - 0.2 m.

A third UAV mission covered the southern extent of surface deformation indicated in the InSAR imagery (Figures 3, S1). Six GCPs were deployed within the 0.86 km^2 mission area, and their locations were surveyed to better than 0.02 m accuracy in the horizontal and 0.04 m accuracy in the vertical using an Altus RTK GPS system. A DoD was calculated using the same methodology above. The DoD shows the faint but continuous trace of a rupture that is everywhere less than 5 cm in height. While this displacement magnitude is consistent with the estimates using the unwrapped InSAR (Figure 6b), the orientation of the rupture at this location, sub-parallel to the maximum compression direction of the crustal stress field (Rajabi et al., 2017), suggests that horizontal motion may have been dominant. The vertical UAV signature might result in part from horizontal displacement of furrows associated with the former forestry land-use.

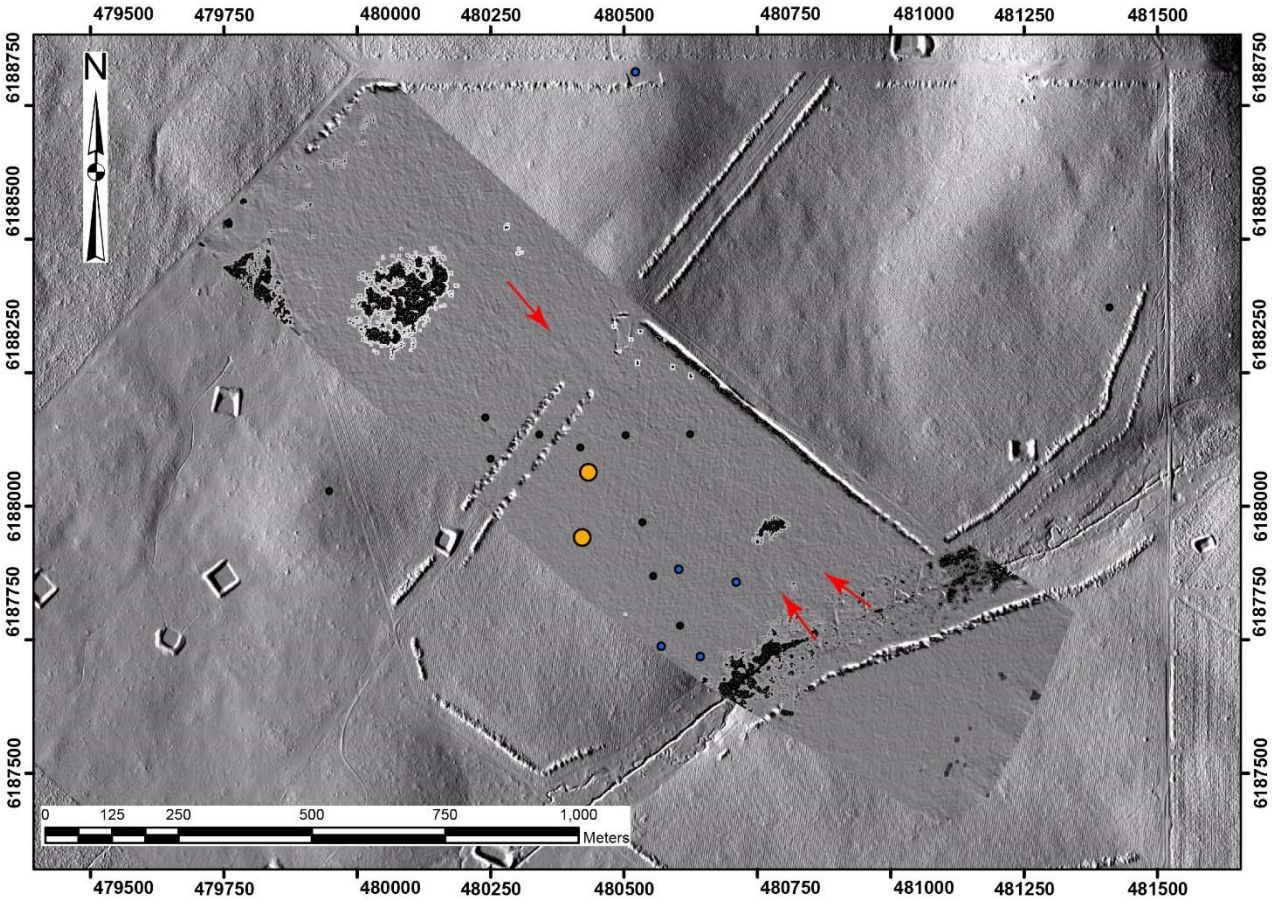

Figure S1: UAV DoD for the southern terminal structure. Subtle scarp with <5 cm vertical displacement is indicated by red arrows (GDA94/MGA50).

Aftershock relocation

Following the Mw 5.3 earthquake near Lake Muir, Western Australia, 884 earthquakes from 16 September, 2018 to 23 November, 2018 were recorded on stations from the permanent ANSN network and from five rapid deployment aftershock kits temporarily installed in the epicentral region. The original locations of these events were located using SeisComP3 seismological software and the LocSAT location algorithm. P- and S-wave arrival times were manually picked and reviewed by on-duty seismic analysts.

To better constrain the location and pattern of aftershocks, events from this dataset were relocated using the HypoDD double-difference relative location algorithm (Waldhauser and Ellsworth, 2000), and implemented with the corresponding software, HypoDDpy (Krischer, 2015). The HypoDD algorithm minimizes errors in hypocentral locations that are commonly attributed to uncertainties in earth structure along the event-station ray path. The algorithm works by first establishing a network of differential P- and S-wave travel times between two proximally located hypocentres that share a minimum number of P- and

S-phase arrivals at common stations. This network of events is determined through initial parameterization using the Ph2dt program (Table S1). This parameterization includes setting a maximum separation distance in kilometres (MAXSEP), a minimum number of phase pairs (MINLNK), and a maximum number of neighbouring events (MAXNGH). To establish strong links between events, Waldhauser (2001) recommends at least eight observations (MINOBS) for each event pair. Table S1 outlines the initial parameters used in the Ph2dt program for the Lake Muir earthquakes. MAXDIST specifies the distance between the event and station in km, and was set to a default value of 100, which includes all stations capable of recording the smaller-magnitude aftershocks in the Lake Muir area. Only events from the original dataset that meet this initial criteria are used in the HypoDD inversion. As a result, catalogue P- and S-wave data from 470 events were included in the final relocation.

MAXDIST	MAXSEP	MAXNGH	MINLNK	MINOBS
100	1	100	8	8

Table S1 Ph2dt input Parameters

Once events are linked together with the Ph2dt program and networks of event pairs are generated, HypoDD groups these events into clusters and then minimizes the travel-time residuals by adjusting the spatial difference of the hypocentres relative to the other hypocentres within the cluster. The double-difference travel-time residual is the difference between the observed and theoretical travel times for each event pair. The source of the P- or S-wave travel time differences of two events at one station can then be attributed to a spatial offset between the hypocentres, since the ray paths between the earthquake source and the seismic station are assumed to be similar. Theoretical travel times are calculated using a 1-D P-wave velocity model, which is derived from Dentith et al. (2000) and Salmon et al. (2012) and incorporates a shallow, low-velocity sediment layer. The VP/VS ratio was set to 1.73.

Depth (km)	0	0.1	5.0	10	15	20	25
P-wave Velocity (km/s)	1.11	5.95	6.20	6.27	6.37	6.57	6.97

Table S2 1-D P-wave velocity model

The double-difference travel-time residuals are minimized by weighted least squares. The Singular Value Decomposition (SVD) inversion method was chosen as the preferred inversion method, because SVD can examine smaller clusters of events and can also produce meaningful three-dimensional hypocentre relocation error estimates (2001). Before running the inversion, the original earthquake locations were separated into four different datasets, shown by the dashed boxes in Figure 1. The events were split to regulate the size of the relocation inversion problems to be solved. The aftershocks in subset A were restricted to magnitudes ML $\geq$ 1.0, since the total number of events near the focus of the 16 September mainshock would

be too large for the SVD inversion method. This magnitude threshold also ensures that the earthquakes are clearly recorded by both the local Lake Muir stations and by regional ANSN stations. Subset D was relocated separately, because these aftershocks temporally relate to the 16 September mainshock and are spatially related to the southern extent of surface rupture. The number of earthquakes and delay times for each subset A-D are shown in Table S3.

Data Subset	Earthquake Counts	P- Delay Times	S- Delay Times
A	106	7401	7314
B	182	8611	9289
C	103	5287	5290
D	18	279	294

Table S3 Earthquake and delay time counts

Within subset A, the A-A' cross-section is oriented approximately normal to the strike direction of the 16 September, 2018 focal mechanism. These events relocate to depths between 1 and 4 km (Figure S2). There is no clearly defined dip angle to this event cluster. Within subset B and along the B-B' cross-section, which is normally oriented to the discrete surface rupture, the earthquakes are also clustered between 1 and 4 km depth. East of the cross-section centre, the aftershocks dip ~30° to the east. The C-C' cross-section is oriented NW-SE: normal to the north-east trending nodal plane of 11 November, 2018 focal mechanism. The epicentres in subset C that linearly trend to the northeast, relocate along a steeply-dipping plane to the north-west. The remaining aftershocks within subset C are constrained to depths of ~1-3 km and show no defined dip direction. Lastly, within the small subset D, the events relocate ~300 m south-west of the observed fault rupture and are constrained to ~2-3 km depth (Figure S2). The mean east-west (EX), north-south (EY), and vertical (EZ) location errors with one standard deviation are displayed in Table S4.

Data Subset	Mean EX $\pm 1\sigma$	Mean EY $\pm 1\sigma$	Mean EZ $\pm 1\sigma$
A	47±30	86±74	126±134
B	72±72	137±147	215±242
C	55±30	92±72	306±255
D	94±59	165±66	523±236

Table S4 Least squares error estimates (m)

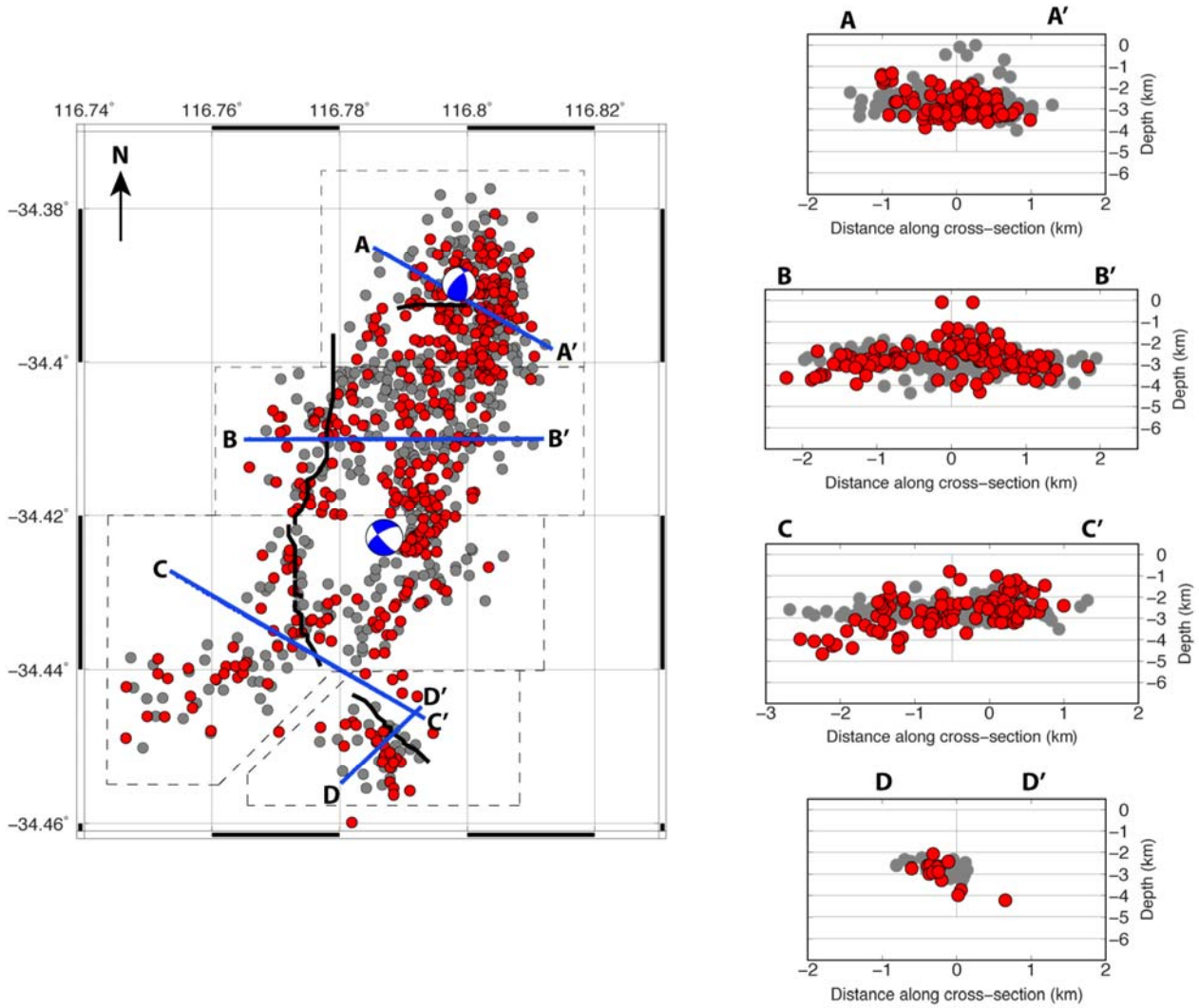

120

Figure S2: Relatively relocated aftershock map and cross-sections near Lake Muir, Western Australia. Grey circles represent the original earthquake locations, and the red circles represent the relocated earthquakes. Dashed boxes indicate the geographical boundaries for the data subsets A-D. Original and relocated earthquakes are projected onto the blue cross-section lines. The length 125 **of each cross-section is defined to include all original and relocated epicentres from each subset. The black lines mark the observed surface rupture from the 16 September earthquake. The focal mechanisms generated by the USGS for the 16 September M_w 5.3 and 11 November M_w 5.2 events are also plotted in map view.**

Mainshock relocation

The absolute location of the September Mw 5.3 Lake Muir mainshock determined by Geoscience Australia is not well 130 constrained by seismic stations of the Australian National Seismic Network. Furthermore, rapid deployment kit LM01 was offline during the November mainshock, which added considerably to the location uncertainty. It was also not possible to

include the mainshocks with the HypoDD relative location of the aftershocks, as the aftershocks were mostly recorded by the aftershock kits, and there are few common local stations linking the aftershocks with the mainshocks. However, two factors make it possible to improve the locations for these largest events. 1) The three largest events (see main text, Table 2), were recorded on at least 19 common regional and teleseismic stations. 2) The October aftershock is well constrained because all of the rapid deployment kits were online, and the event occurred within a kilometre of station LM01.

It is possible in this case to do a three-event relative location, and then "anchor" the group to a known location (i.e. the October aftershock) to produce an improved absolute location of the two largest events. To do this we adapt the method of Fisk (2002), which uses a combination of manual waveform alignment and the Joint Hypocenter Determination (JHD) technique on regional and teleseismic phases to obtain an accurate relative location, and then anchors at least one event to a known surface location (in their case, satellite images of surface displacement). While this method was developed for the high-precision location of nuclear weapons with repeatable waveforms, the flexibility provided by manual waveform alignment makes it possible to use in situations even where the waveforms do not perfectly match. Our application is as follows:

1. Each earthquake is located using a suitable earthquake location program, using travel times read on the following Australian and IMS stations. AU: KDU, KLBR, BBOO, CMSA, KNRA, MEEK, MORW, MTKN, MTN, MUN, NAPP, QIS, STKA; IMS: CM31, KURBB, NWAO, QSPA. The inclusion of QSPA in Antarctica is particularly important as it is the only station to the south of the event, and is needed to reduce the azimuthal gap. In principle, any standard earthquake location algorithm or approach which is capable of handling regional and teleseismic phases can be used for the Fisk (2002) relative location strategy. We solve the seismic location problem using the "neighbourhood algorithm" approach (Sambridge and Kennett, 2001) and the AK135 travel times (Kennett et al., 1995), but we could have adapted a formal program such as LocSAT (Bratt and Nagy, 1991) or NonLinLoc (Lomax, 2008) to do the same.
2. Waveforms for each event at each station are manually aligned using the GeoTool program, and the P phases are re-picked (Figure S3). In practice, this seems to improve the relative accuracy of the phase pick by about an order of magnitude or more. Like with the previous step, this outcome could also have been accomplished using another waveform analysis program such as SAC (Goldstein et al., 2003).
3. The average travel time residual of all three events is subtracted from the travel time of each event on a station-by-station basis, and the location is calculated again. We fixed the earthquake depth at 2 km as the aftershock cloud begins at this depth, but we note that changing the depth between 0-10 km has little effect on the surface location as the nearest stations are relatively distant. This process is iterated as many times as necessary, and we find that the residuals converge after just three iterations. This method is equivalent to the JHD approximation technique described in Pujol (2000), but any of the other JHD techniques mentioned there would have been appropriate as well.
4. The three events, which are now accurately located in a relative sense, are shifted so that the relatively located October M_L 4.6 event overlies the October event location calculated using the aftershock kits. This yields precise absolute locations of the September and November mainshocks.

5. Errors are calculated assuming that the precision of the travel time picks is within 4 samples. We use a modified Gaussian distribution with an L1 norm. This step is optional and is not intended to be extremely accurate. Rather, it is more indicative of the stability of the solution in terms of azimuthal coverage. There is ongoing debate regarding the appropriateness of error bars in relative locations, since a single poor phase pick can throw the solution out by orders of magnitude. It is therefore more important to ensure the data quality.

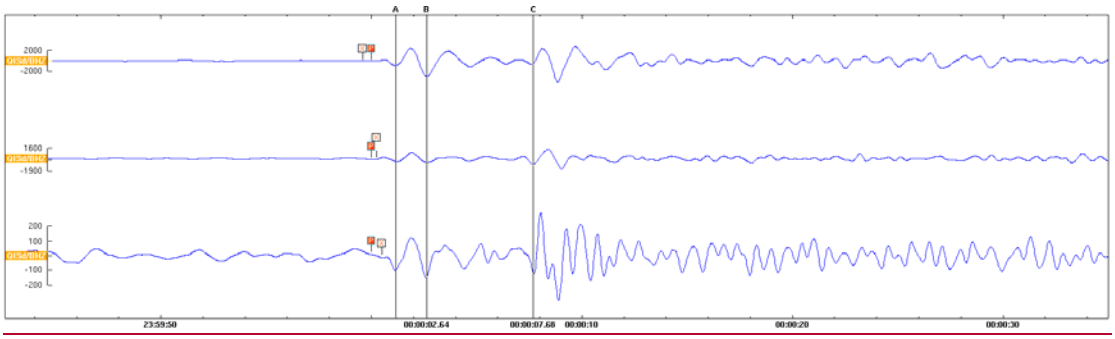

Figure S3. An example of a manual alignment of Lake Muir waveforms in GeoTool on the vertical component of station QIS. Top to bottom: September, November and October events respectively. "X" picks represent old phase picks. "P" picks are the new picks made after alignment, which is one pick made across all three events at the same time. The events were manually aligned by dragging them so that key features (e.g. A, B, and C) are aligned between them. These waveforms have been bandpass filtered 0.4-1.8 Hz (3rd order). While the P to X changes look small, the largest correction is 0.52 seconds. This makes a significant difference when calculating a relative location.

Coulomb Stress modelling

When slip occurs on a fault (the 'source' fault) stress is imparted to the surrounding crust and faults ('receiver' faults). In Coulomb stress modelling (e.g. Lin and Stein, 2004; Toda et al., 2005; Toda et al., 2011), fault displacements in the elastic half-space are used to calculate a 3D strain field, which is multiplied by the elastic stiffness to derive stress changes. Stress changes might be used to understand the distribution of aftershocks resulting from an event, or the static stress changes caused by displacement on a 'source' fault can be resolved onto 'receiver' faults to investigate whether they are promoted towards failure. The shear stress increase or decrease is dependent on the position, geometry, and slip of the source fault and on the position and geometry of the receiver fault, including its rake. The normal stress change (clamping or unclamping) is independent of the receiver fault rake (Toda et al., 2011).

Toda et al. (2011) use the Coulomb failure criterion, $\Delta\sigma_f = \Delta\tau_s + \mu' \Delta\sigma_n$, in which failure is hypothesized to be promoted when the Coulomb stress change is positive. Here, Δσf is the change in failure stress on the receiver fault caused by slip on the source fault(s), Δτs is the change in shear stress (reckoned positive when sheared in the direction of fault slip), Δσn is change in normal stress (positive if the fault is unclamped), and μ' is the effective coefficient of friction on the fault.

The source fault was parametrised as follows: length = 5 km, strike = 5°, dip = ~~30~~50°, dip slip = 0.6 m, strike slip = 0.0 m, rake = 90 °, top of rupture = 0 km, bottom of rupture = 0.~~8~~ 9 km, co-efficient of friction (μ') = 0.6 (Figures 8 and S4). The preferred parametrisation for the ~~The~~ strike-slip receiver fault (i.e. the November rupture plane) was determined through simple forward modelling using a finite rectangular elastic dislocation model (Okada, 1985) (https://earthquakes.aranzgeo.com/model/generic1). The Parameters that were found to best match the surface expression are as follows:~~parametrised as follows:~~ length = ~~5~~4.1 km, strike = ~~215~~233°, dip = 8~~9~~8°, dip slip = 0.0 m, strike slip = 0.~~0~~4 m, rake = ~~180~~0 °, top of rupture = 1.0 km, bottom of rupture = 2.5~~.0~~ km (Figure S5). This plane is shown in section on Figure S4b.

The Coulomb stress change consequent of the Lake Muir September M_W 5.3 reverse fault rupture was resolved for ~~dextral~~ optimally oriented ~~strike~~ strike-slip events parallel to the plane of the November M_W 5.2 strike-slip rupture (Figure ~~S3~~S4). This calculation shows that the plane of the November rupture was brought closer to failure over approximately half of its area, though only slightly so in the hypocentral region.

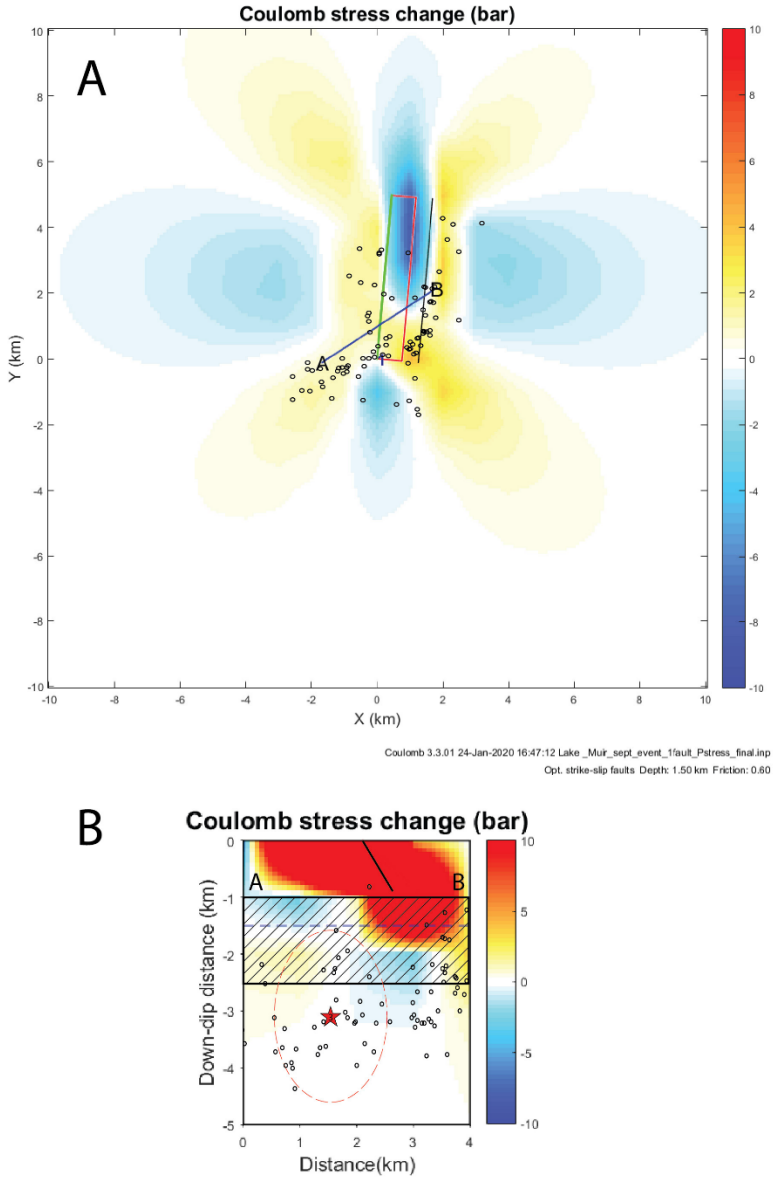

Figure ~~S3~~S4: Coulomb stress change resulting from the September event resolved for dextral strike-slip events onto the plane of the November rupture. Stress increase values are shown in bars. The location and uncertainty ellipse of the hypocentre for the November event is shown.

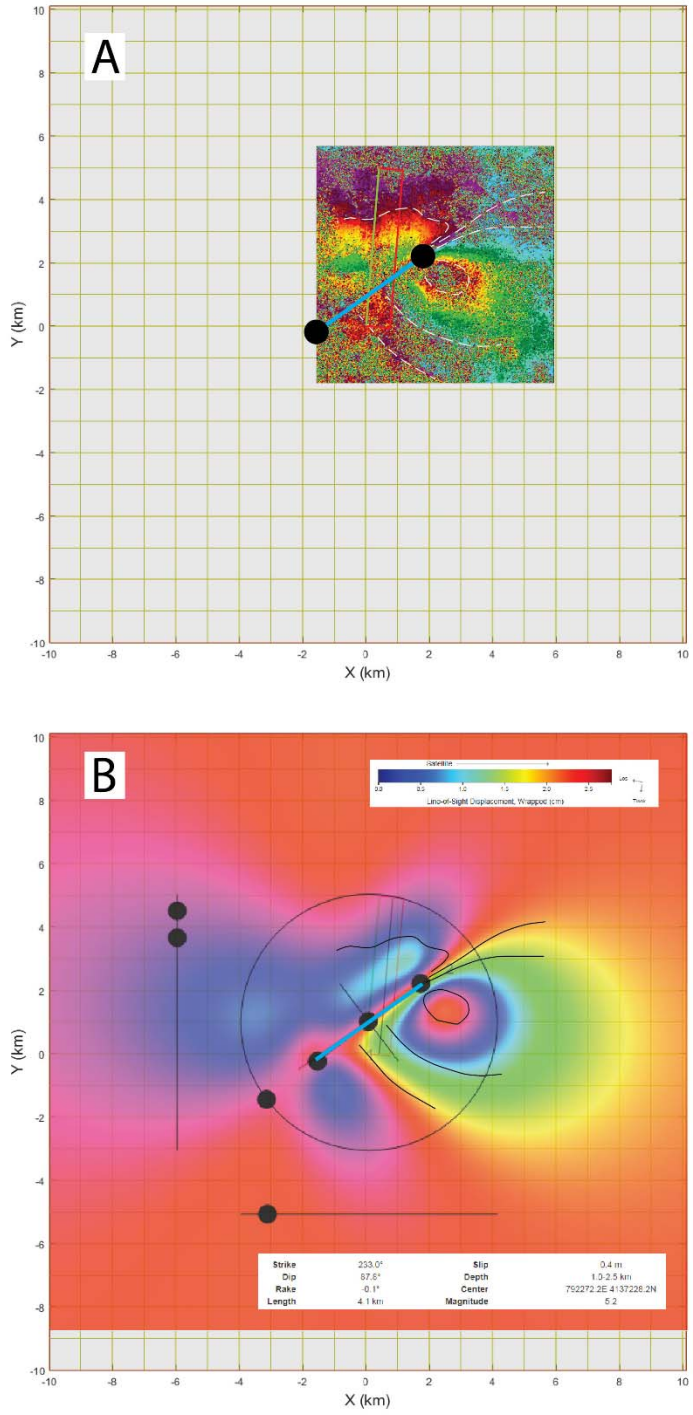

Figure S5: Simple forward modelling of InSAR surface deformation envelope for the Lake Muir November mainshock. (a) InSaR phase image (recoloured from Figure 6C to enhance fringes). Fringes used for matching are delineated with white dashes. Preferred fault trace shown with a blue line ending in lack dots. (b) Forward model showing match to fringes (white dashed lines in part (a) are reproduced as black lines).

References

Agisoft LCC: . Agisoft PhotoScan Pro 1.4.3. Available online: http://www.agisoft.com (accessed November 2018).

Bratt, S. R., and Nagy, W.: The LocSAT Program, Science Applications International Corporation , San Diego, 1991.

Dentith, M. C., Dent, V. F., and Drummond, B. J.: Deep crustal structure in the southwestern Yilgarn Craton, Western Australia, Tectonophysics, 325, 227-255, 2000.

Fisk, M. D.: Accurate Locations of Nuclear Explosions at the Lop Nor Test Site Using Alignment of Seismograms and IKONOS Satellite Imagery, Bulletin of the Seismological Society of America, 92, 2911-2925, 10.1785/0120010268 %J Bulletin of the Seismological Society of America, 2002.

Gindraux, S., Boesch, R., and Farinotti, D.: Accuracy Assessment of Digital Surface Models from Unmanned Aerial Vehicles' Imagery on Glaciers, Remote Sensing, 9, 186, 2017.

Goldstein, P., Dodge, D., Firpo, M., Minner, L., Lee, W. H. K., Kanamori, H., Jennings, P. C., and Kisslinger, C.: SAC2000: Signal processing and analysis tools for seismologists and engineers, The IASPEI International Handbook of Earthquake and Engineering Seismology 81 1613-1620, 2003.

Kennett, B. L. N., Engdahl, E. R., and Buland, R.: Constraints on seismic velocities in the Earth from traveltimes, Geophysical Journal International 122, 108-124, 1995.

Krischer, L.: hypoDDpy: hypoDDpy 1.0 Zenodo, 2015.

Lin, J., and Stein, R. S.: Stress triggering in thrust and subduction earthquakes and stress interaction between the southern San Andreas and nearby thrust and strike-slip faults, Journal of Geophysical Research: Solid Earth, 109, doi:10.1029/2003JB002607, 2004.

Lomax, A.: The NonLinLoc software guide, http://alomax.free.fr/nlloc ALomax Scientific, Mouans-Sartoux, France, 2008.

Okada, Y.: Surface deformation due to shear and tensile faults in a half-space, Bulletin of the Seismological Society of America, 75, 1135-1154, 1985.

Ouédraogo, M. M., Degré, A., Debouche, C., and Lisein, J.: The evaluation of unmanned aerial system-based photogrammetry and terrestrial laser scanning to generate DEMs of agricultural watersheds, Geomorphology, 214, 339–355, 2014.

Pujol, J.: Joint Event Location — The JHD Technique and Applications to Data from Local Seismic Networks, in: Advances in Seismic Event Location, edited by: Thurber, C. H., and Rabinowitz, N., Springer Netherlands, Dordrecht, 163-204, 2000.

Rajabi, M., Tingay, M., Heidbach, O., Hillis, R., and Reynolds, S.: The present-day stress field of Australia, Earth-Science Reviews, 168, 165-189, 10.1016/j.earscirev.2017.04.003, 2017.

Salmon, M., Kennett, B. L. N., and Saygin, E.: Australian Seismological Reference Model (AuSREM): crustal component, Geophysical Journal International, 192, 190-206, 10.1093/gji/ggs004 %J Geophysical Journal International, 2012.

Sambridge, M. S., and Kennett, B. L. N.: Seismic event location: nonlinear inversion using a neighbourhood algorithm, Pure and Applied Geophysics 158, 241-257, 2001.

Seitz, S. M., Curless, B., Diebel, J., Scharstein, D., and Szeliski, R.: A comparison and evaluation of multi-view stereo reconstruction algorithms, In Proceedings of the 2006 IEEE Computer Society Conference on Computer Vision and Pattern Recognition (CVPR'06), New York, NY, USA, 17–22 June 2006, 1, 2006.

Serifoglu Yilmaz, C., Yilmaz, V., and Güngör, O.: Investigating the performances of commercial and non-commercial software for ground filtering of UAV-based point clouds, International Journal of Remote Sensing, 39, 5016-5042, 10.1080/01431161.2017.1420942, 2018.

Toda, S., Stein, R. S., Richards-Dinger, K., and Bozkurt, S. B.: Forecasting the evolution of seismicity in southern California: Animations built on earthquake stress transfer, 110, 10.1029/2004jb003415, 2005.

Toda, S., Stein, R. S., Sevilgen, V., and Lin, J.: Coulomb 3.3 Graphic-Rich Deformation and Stress-Change Software for Earthquake, Tectonic, and Volcano Research and Teaching — User Guide, USGS Open File Report, 2011-1060, 63p, 2011.

Tonkin, T. N., and Midgley, N. G.: Ground-Control Networks for Image Based Surface Reconstruction: An Investigation of Optimum Survey Designs Using UAV Derived Imagery and Structure-from-Motion Photogrammetry, Remote Sensing, 8, 1–8, 2016.

Waldhauser, F., and Ellsworth, W. L.: A Double-Difference Earthquake Location Algorithm: Method and Application to the Northern Hayward Fault, California, Bulletin of the Seismological Society of America, 90, 1353-1368, 10.1785/0120000006 %J Bulletin of the Seismological Society of America, 2000.

Waldhauser, F.: HypoDD: A Computer Program to Compute Double-difference Hypocenter Locations, USGS Open File Report 25, 1–113, 2001.

Williams, R.: DEMs of difference, Geomorphological Techniques, 2, 2012.

Zhang, W., Qi, J., Wan, P., Wang, H., Xie, D., Wang, X., and Yan, G.: An Easy-to-Use Airborne LiDAR Data Filtering Method Based on Cloth Simulation, Remote Sensing, 8, 501, 2016.